LASER INTERFEROMETER GRAVITATIONAL WAVE OBSERVATORY
- LIGO -
CALIFORNIA INSTITUTE OF TECHNOLOGY
MASSACHUSETTS INSTITUTE OF TECHNOLOGY

Technical Note	**LIGO-T0900511-v4**

Modeling of Alignment Sensing and Control for Advanced LIGO

L. Barsotti, M. Evans
LIGO-MIT

This is an internal working
note of the LIGO project

California Institute of Technology
LIGO Project, MS 18-34
Pasadena, CA 91125
Phone (626) 395-2129
Fax (626) 304-9834
E-mail: info@ligo.caltech.edu

Massachusetts Institute of Technology
LIGO Project, Room NW17-161
Cambridge, MA 02139
Phone (617) 253-4824
Fax (617) 253-7014
E-mail: info@ligo.mit.edu

LIGO Hanford Observatory
Route 10, Mile Marker 2
Richland, WA 99352
Phone (509) 372-8106
Fax (509) 372-8137
E-mail: info@ligo.caltech.edu

LIGO Livingston Observatory
19100 LIGO Lane
Livingston, LA 70754
Phone (225) 686-3100
Fax (225) 686-7189
E-mail: info@ligo.caltech.edu

WWW: http://www.ligo.caltech.edu/

Abstract

This note presents a model of the alignment sensing and control scheme for Advanced LIGO. The model has been realized with the frequency domain tool Optickle, which has the peculiarity of including radiation pressure effects.

The optical configuration studied here corresponds to the Advanced LIGO baseline as at August 2009. In particular, stable recycling cavities are considered.

1 Introduction

The main changes which characterize Advanced LIGO (aLIGO) with respect to the first generation of LIGO detectors (iLIGO and eLIGO) are:

- up to about 10 times higher input laser power than initial detectors;
- an optical layout which includes stable recycling cavities and a signal recycling mirror (see Figure 1);
- complex suspensions and seismic isolation systems for the main optics.

While these changes will improve detector performance, they complicate the control strategy needed to keep the interferometer (IFO) at its operating point. In particular, all the mirrors need to be well aligned both in pitch (a rotation of the mirror about the horizontal axis) and yaw (a rotation of the mirror about its vertical axis) with respect to each other and with respect to the incoming beam in order to guarantee stable operation of the detector. A residual angular motion of the arm cavity mirrors of the order of 1 nrad RMS is required in order to meet the aLIGO sensitivity target, about three orders of magnitude higher than their actual motion. An alignment sensing and control (ASC) system is therefore needed in order to reduce the angular motion of the mirrors. While an ASC scheme has operated in LIGO for many years [10], the increased complexity of aLIGO requires modifications of ASC in order to deal with the new elements of the design, which can be explained in terms of additional complexity for ASC as follows:

- **radiation pressure effects** introduced by the high circulating power inside the arm cavities. They modify the opto-mechanical angular transfer functions, and they have to be taken into account when designing the ASC scheme. aLIGO is designed to have a maximum input power of 125 W, about 18 times more power then iLIGO (7 W). eLIGO has a target of 35 W, and it is currently operating at 14 W. The factor 2 of increase in power with respect to iLIGO was already enough to make the torque induced by the radiation pressure comparable to the pendulum restoring torque, and required a re-thinking of the ASC. A new ASC scheme which takes into account the new opto-mechanical transfer functions of the system was designed [2] and implemented at the sites. A similar approach can be adopted for the aLIGO ASC design;

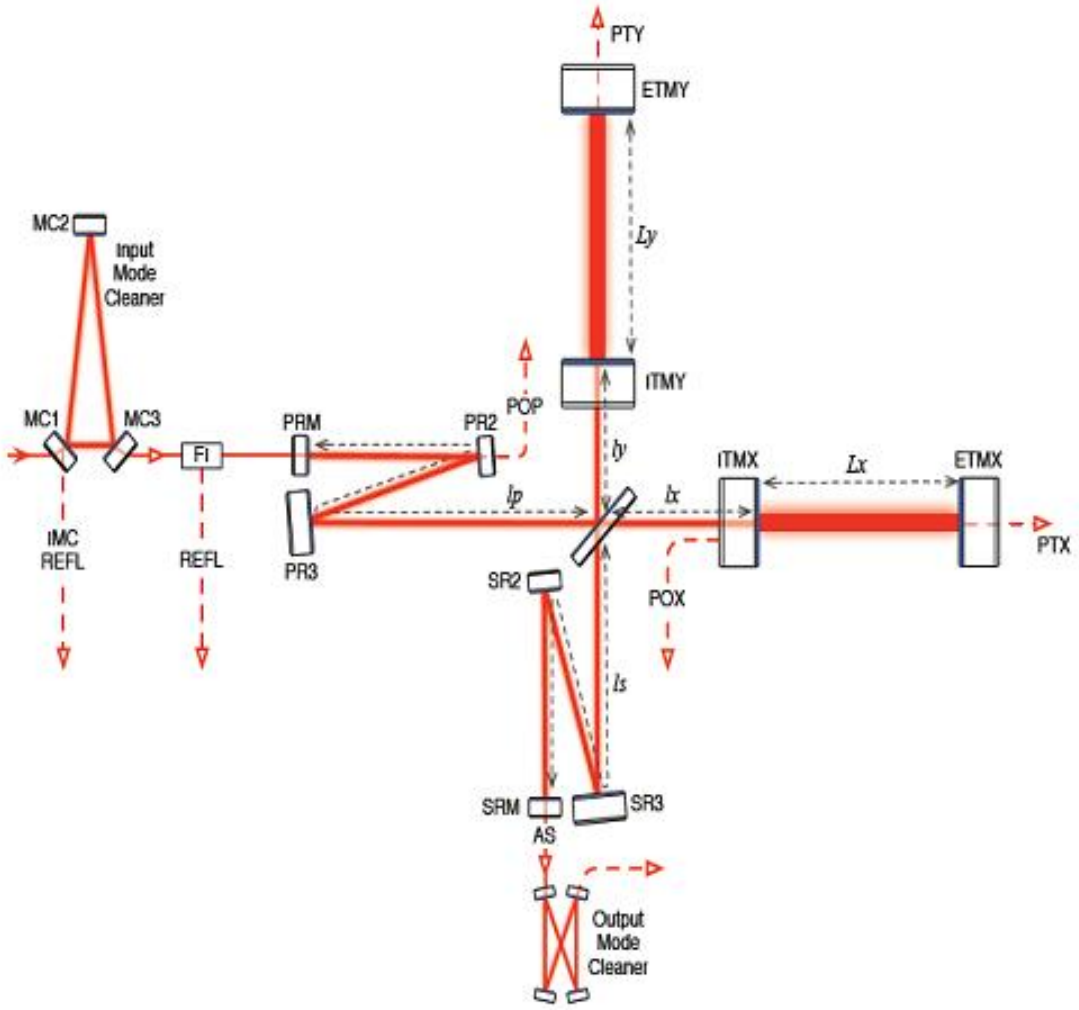

Figure 1: aLIGO optical layout.

- **more mirrors to be controlled**, i.e. a new sensing scheme is required for controlling the signal recycling mirror (SRM), and the 4 telescope mirrors required to make stable recycling cavities (PR2, PR3, Sr2 and SR3, see Figure 1);
- a more complex control strategy which takes into account the transfer functions of the **new mirror suspensions**;
- **more stringent noise requirements**, since the angular noise must be compatible with science mode operation down to 10 Hz (instead of 40 Hz as in previous LIGO detectors), where aLIGO aims to have a sensitivity of $6 \times 10^{-18}\ m/\sqrt{\text{Hz}}$.

A conservative approach requires the angular noise coupled to DARM to be at least a factor 10 below the design sensitivity. Besides the noise requirements, there are other concerns that the ASC design for aLIGO should address, based on eLIGO experience,:

- there should be an "acquisition mode" control scheme, easy to implement and robust, even if not low noise. The most appealing solution would be to have a sensing matrix which is close to diagonal, and minimal measurements required to achieve stability. The main goal is to speed up the commissioning phase in which the angular loops are open, and in that state an accurate measurement of the sensing matrix, needed to close the loops, is not possible;

- the design should be as much as possible input power independent, so as to minimize the needed changes in the control scheme while increasing the input power. This was observed not to be the case with the ASC scheme in eLIGO, which needs to be re-tuned at each power level. The main reason for that is the imperfect compensation of the thermal lens in the input mirrors, which causes the recycling cavity mode shape to change. This effect should be mitigated by the presence of stable recycling cavities, and a faster thermal compensation system.

Performance of the ASC is strictly connected to the stand-alone angular mirror motion of the aLIGO suspensions and the internal seismic isolation systems (ISI), which are currently prototyped at LASTI (BSC ISI, for the BS and test masses) and the LIGO sites (HAM ISI, for the other suspended optics). A full Quadruple pendulum has been suspended to the BSC ISI in LASTI, forming the first full scale aLIGO test mass attenuation system. The angular noise transferred to the aLIGO optics has been estimated on the basis of the current achieved performance (all the details can be found in appendix C). Since the tuning of the seismic isolation system is ongoing, it is reasonable to consider this estimate as a worse case scenario.

The model presented in this note has been developed with the frequency domain simulation tool Optickle [1], which includes radiation pressure effects. The note is organized in the following way:

- Section 2 summarizes the aLIGO optical parameters;

- Section 3 describes the effect of radiation pressure on the opto-mechanical angular transfer functions of the aLIGO test masses;

- Section 4 shows the signal content at the different output-ports of the IFO, and the proposes read-out scheme;

- in Section 5 the architecture of the ASC model is detailed;

- Sections 7 8 9 show the results of the ASC model in different optical configurations and input powers.

2 aLIGO parameters

The following tables summarizes the aLIGO parameters considered in this model, which are described in [12].

Quantity	Value
Arm Finesse	443
ITM transmission	1.4%
ETM transmission	5 ppm
PRM transmission	3%
SRM transmission	20%
Schnupp asymmetry	0.05 m
l_{PRC}	57.656 m
l_{SRC}	56.008 m
l_{EX}	3994.50 m
l_{EY}	3994.50 m
Lower mod. frequency (f1)	$9,099,471$ Hz
Upper mod. frequency (f2)	$45,497,355.$ Hz
Modulation index (f1, f2)	0.1

Table 1: Optical parameters.

Distance	Value (m)
PRM $\longleftrightarrow$ PR2	16.6037
PR2 $\longleftrightarrow$ PR3	16.1558
PR3 $\longleftrightarrow$ BS	19.5384
SRM $\longleftrightarrow$ SR2	15.726
SR2 $\longleftrightarrow$ SR3	15.4607
SR3 $\longleftrightarrow$ BS	19.368
BS $\longleftrightarrow$ ITMX	5.3828
BS $\longleftrightarrow$ ITMY	5.3328

Optic	ROC (m)	Beam Size (mm)
ETM	2245	62.0
ITM	1934	53.0
PRM	-10.997	2.3
PR2	-4.55	6.2
PR3	36.00	54.0
SRM	-5.6938	2.1
SR2	-6.428	8.2
SR3	36.00	54.0

Table 2: Optical path distances between the HR surfaces of the optics (left) and ROC and beam size for each optic (right).

The selected Gouy phases for the stable recycling cavities are:

$$\phi_{PRC} = 25^\circ \tag{2.1}$$

$$\phi_{SRC} = 19^\circ \tag{2.2}$$

This choice does not optimize cavity mode matching stability, but it is the best compromise found in between good alignment signals and stability, as will be discussed in the following sections.

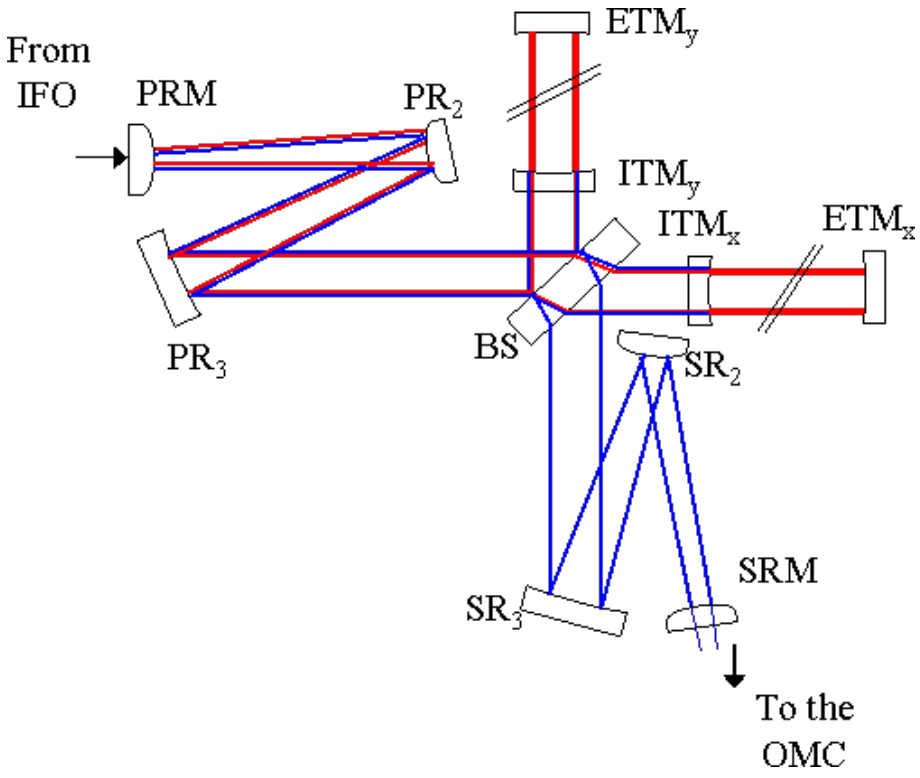

Figure 2: Beam profile in the stable recycling cavities (figure taken from [12]) .

3 Radiation Pressure Effects

The high circulating power inside the aLIGO arm cavities causes radiation pressure effects to be comparable with the restoring torque of the pendulum suspensions. For this reason, they need to be taken into account when modeling the angular control of aLIGO. Since aLIGO operates over a wide range of powers, it is also useful to see how the transfer functions change as function of the circulating power. The way in which radiation pressure effects are usually described for a single Fabry-Perot cavity will be recalled first [3].

3.1 Torsional stiffness matrix

For a single Fabry-Perot cavity, the radiation pressure torque can be written in terms of the optical parameters of the cavities in the form of a 2×2 matrix which couples the static misalignments of the two cavity mirrors [3]:

$$\tau = \hat{\mathbf{K}}_{opt}(g_{ETM}, g_{ITM}, L, P) \begin{pmatrix} \theta_{ETM} \\ \theta_{ITM} \end{pmatrix} \tag{3.1}$$

where g_1 and g_2 are the g factors of the cavity, L the length and P the intra-cavity power.

$\hat{\mathbf{K}}_{opt}$ is the torsional stiffness matrix, defined as:

$$\hat{\mathbf{K}}_{opt} = k_0 \begin{pmatrix} g_{ITM} & 1 \\ 1 & g_{ETM} \end{pmatrix} \tag{3.2}$$

with

$$k_0 = \frac{2PL}{c(g_{ETM}g_{ITM} - 1)}.$$

3.2 Hard and Soft modes

The analytical expressions of the eigenvalues and the eigenvectors of the torsional stiffness matrix $\hat{\mathbf{K}}_{opt}$ are:

$$k_S = k_0 \frac{(g_{ETM} + g_{ITM}) + \sqrt{(g_{ETM} - g_{ITM})^2 + 4}}{2} \qquad v_S = [1, \frac{k_0}{k_S - k_0 g_{ETM}}] \tag{3.3}$$

$$k_H = k_0 \frac{(g_{ETM} + g_{ITM}) - \sqrt{(g_{ETM} - g_{ITM})^2 + 4}}{2} \qquad v_H = [\frac{k_0}{k_0 g_{ITM} - k_H}, -1] \tag{3.4}$$

The two eigenvectors correspond to the basis of cavity misalignments which makes the torque stiffness matrix diagonal. It can be easily shown that:

$$\frac{k_0}{k_S - k_0 g_{ETM}} = \frac{k_0}{k_0 g_{ITM} - k_H} = \frac{2}{(g_{ITM} - g_{ETM}) + \sqrt{(g_{ETM} - g_{ITM})^2 + 4}}$$

By defining

$$r = \frac{2}{(g_{ITM} - g_{ETM}) + \sqrt{(g_{ETM} - g_{ITM})^2 + 4}}$$

a change of basis which makes the torque stiffness matrix diagonal can be described as:

$$\begin{pmatrix} 1 & r \\ r & -1 \end{pmatrix} \times \hat{\mathbf{K}}_{opt} \times \begin{pmatrix} 1 & r \\ r & -1 \end{pmatrix}^{-1} = \begin{pmatrix} k_S & 0 \\ 0 & k_H \end{pmatrix} \tag{3.5}$$

This is the normal mode basis which decouples the effects of radiation pressure in two independent modes. The two modes of misalignment are shown in figure 3.

We choose the names *hard* and *soft* for them, in order to put in evidence the fact that in one case the torque induced by radiation pressure tends to make the mode stiffer (*hard*), while in the other case it tends to make the mode less stiff (*soft*).

For aLIGO (cfr table 2):

$$g_{ETM} = 1 - L/R_{ETM} = -0.7794 \tag{3.6}$$

$$g_{ITM} = 1 - L/R_{ITM} = -1.0655 \tag{3.7}$$

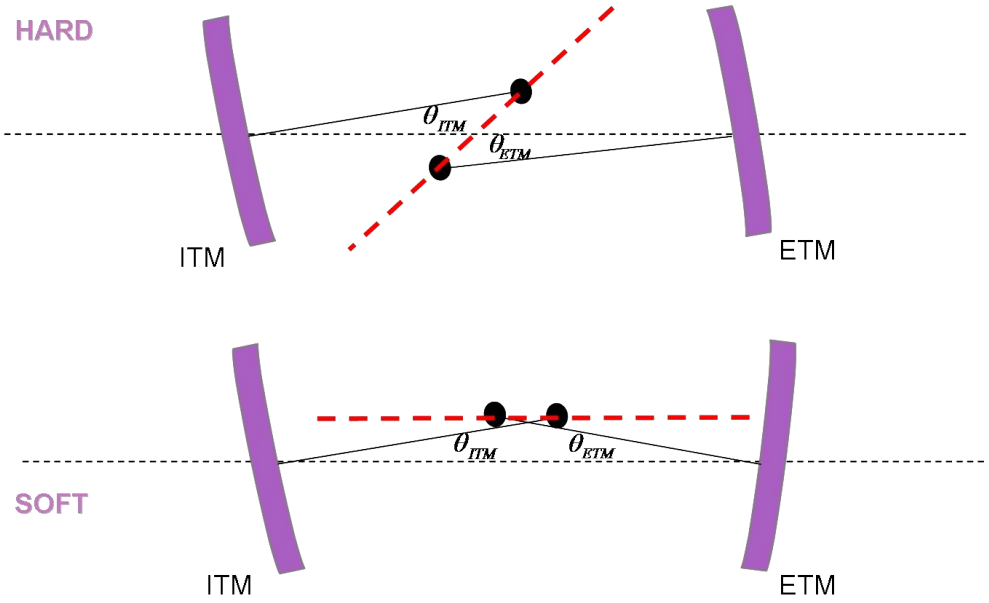

Figure 3: Representation of the basis which diagonalizes the torque stiffness matrix: the hard mode (top) and the soft mode (bottom).

The intra-cavity power P corresponding to a power P_0 entering the IFO can be estimated by taking into account the nominal recycling gain G_{rec} and the arm cavity gain G_{arm}:

$$P = \frac{1}{2} \times P_0 \times G_{rec} \times G_{arm} \tag{3.8}$$

where:

$$G_{rec} = 43.5 \tag{3.9}$$

$$G_{arm} = \frac{2 * 443}{\pi} = 282 \tag{3.10}$$

According to this naive calculation the maximum intra-cavity power expected for aLIGO is about 770 kW. The corresponding optical torques are:

$$k_S = -10.57 \text{ Nm} \qquad v_S = [1, r] \tag{3.11}$$

$$k_H = 232.96 \text{ Nm} \qquad v_H = [r, -1] \tag{3.12}$$

with $r = 1.1533$.

The radiation pressure torque for the soft mode has a negative value. The resonance frequency of the opto-mechanical angular dofs is determined by the sum of the restoring torque and the radiation pressure torque. This means that the stability of the soft mode depends entirely on the restoring torque of the suspension.

3.3 Shift of the pendulum frequency in aLIGO

A complete Matlab model of the Quadruple suspension (QUAD) has been developed and tuned to match the response of the LASTI prototype [7]. Figure 4 shows the transfer function torque to angle of the aLIGO test mass, the last stage in the QUAD, for PITCH and YAW. For reference, the same transfer function is plotted for a simple pendulum suspension (as in iLIGO and eLIGO) which has the same lowest resonance frequency and the same momentum of inertia as the aLIGO test masses.

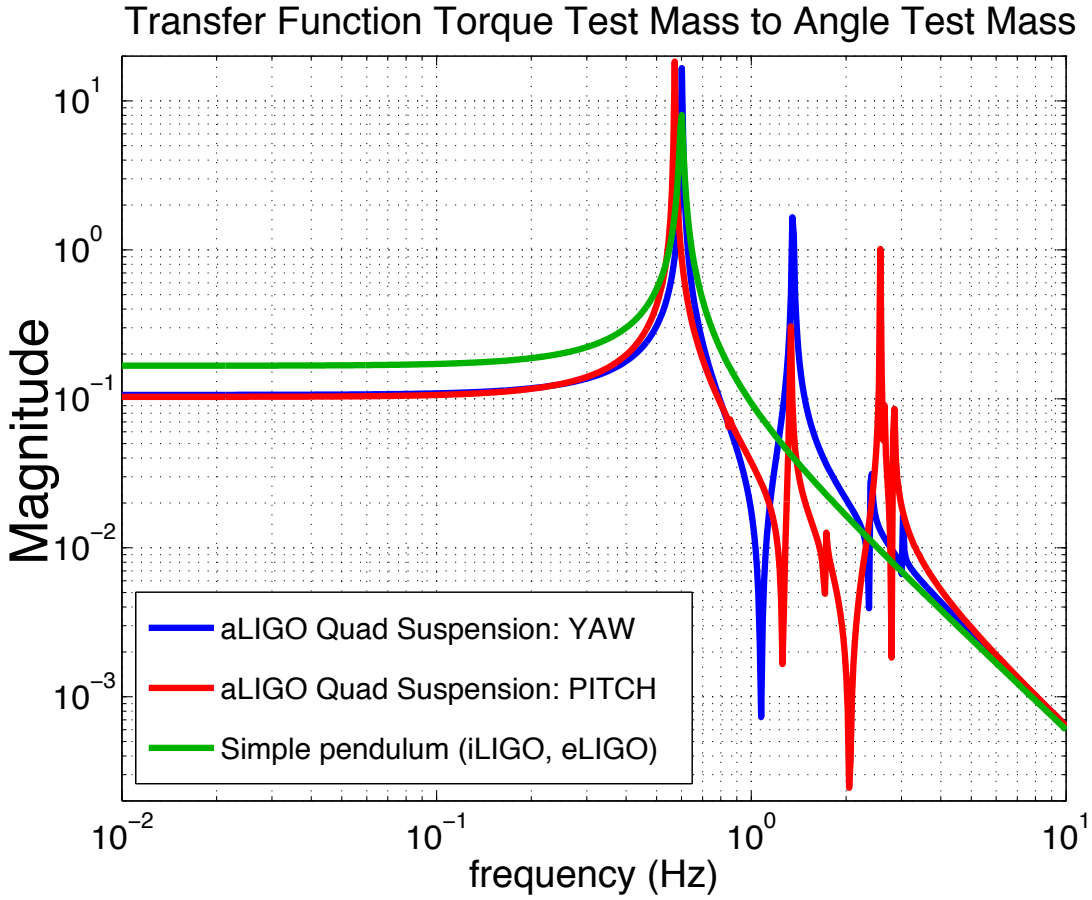

Figure 4: Amplitude of the transfer function from torque on the test mass to angle of the test mass. PITCH and YAW of the aLIGO QUAD suspension are plotted. For comparison, a simple pendulum iLIGO-like transfer function with an angular frequency of 0.6 Hz and same high frequency slope as the quadruple pendulum TFs is shown as well. Since the restoring torque is inversely proportional to the DC value of the transfer function, the plot shows how the restoring torque in aLIGO will be about 50% higher than what would have been with a simple pendulum suspension.

The restoring torque is slightly higher for PITCH than for YAW, as reported in table 3. Note that the restoring torque for aLIGO, both for PITCH and YAW, will be more than a

factor 1.5 higher than the one predicted by considering a simple pendulum with aLIGO test masses and a resonance frequency of 0.6 Hz. In that hypothetical case, the restoring torque would be $k = 6$ Nm (as assumed in [3]).

In order to explain how radiation pressure modifies the opto-mechanical transfer function of the system, we first simplify our analysis by considering only the lowest resonance of the mechanical transfer function, so as to have a simple pendulum transfer function. A more complete description with the full QUAD transfer functions is shown in section 3.5.

An 'equivalent' momentum of inertia has been computed by dividing the value of the DC restoring torque by the square of the resonance frequency[1]. In this approximation, the soft and hard mode resonance frequency can be computed by using the value of the restoring torque and the equivalent momentum of inertia listed in table 3:

$$f = \frac{1}{2\pi}\sqrt{\frac{k_{res} + k_{opt}}{I_{eq}}} \tag{3.13}$$

Tables 4 and 5 show the resonance frequency for PITCH and YAW. At its nominal power, aLIGO will have unstable angular modes both for PITCH and YAW. However, the computed value of the unstable frequency is quite small, about 200 mHz, and this makes the instability easy to compensated with the control filter. For this reason, even if the circulating power will be much higher in aLIGO than in the past, radiation pressure effects are expected to be more easily controllable.

DOF	**Restoring Torque (Nm)**	**Equivalent Momentum of Inertia I (Kgm^2)**	**Pendulum Frequency (Hz)**
PITCH	9.72	0.757	0.57
YAW	9.41	0.663	0.60

Table 3: Advanced LIGO suspension parameters for PITCH and YAW.

The modification of the PITCH opto-mechanical transfer functions due to radiation pressure in an aLIGO-like arm cavity can be seen in Figure 5. In our model, the maximum circulating power in the aLIGO arm cavities is about 720 kW[2]. The plot shows, still in the case of a simple pendulum, the opto-mechanical transfer functions of the soft and hard mode in this regime, and the mechanical transfer function in absence of radiation pressure. As mentioned earlier, the soft mode is actually unstable. In order to make it stable, the unity gain frequency of the loop needs to be about ten times higher than the frequency of the unstable resonance in order to provide overall stability.

[1] Another way of modeling the torque to angle transfer function of the quadruple suspension with a simple pendulum would be to match the high and low frequency slope, and define an arbitrary resonance frequency. Since we are interested in understanding when the lowest resonance becomes unstable, we adopt the method described in the text.

[2] The discrepancy with the theoretical value of 770 kW is due to the fact that the carrier power entering the IFO is less than 125 W, due to the two sets of sidebands.

IFO	Intra-cavity Power (kW)	Pendulum Frequency (Hz)	Hard Frequency (Hz)	Soft Frequency (Hz)
iLIGO	15	0.6	0.69	-0.25
eLIGO	87.5	0.6	1.00	-1.46
aLIGO	770	0.57	2.85	-0.17

Table 4: Frequency of the PITCH angular resonance.

IFO	Intra-cavity Power (kW)	Pendulum Frequency (Hz)	Hard Frequency (Hz)	Soft Frequency (Hz)
iLIGO	15	0.5	0.60	-0.42
eLIGO	87.5	0.5	0.95	-1.49
aLIGO	770	0.6	3.05	-0.21

Table 5: Frequency of the YAW angular resonance.

Since aLIGO will operate over a range of different input powers, it is useful to see how the hard and soft mode frequencies move as a function of the total power stored inside the arm cavities. (figure 6). It is interesting to note that the soft mode will become unstable only close to the maximum aLIGO power. Below that threshold, both the hard and soft modes will be stable.

3.4 Common and Differential DOFs

For a two cavity IFO like aLIGO, the error signals extracted from the IFO naturally distinguish between common and differential motions of the two cavities. It is therefore convenient to choose the basis of the common and differential soft and hard modes. The 4×4 matrix which expresses the misalignment of the cavity mirrors in terms of the new basis is:

$$\begin{pmatrix} \theta_{EX} \\ \theta_{EY} \\ \theta_{IX} \\ \theta_{IY} \end{pmatrix} = \begin{pmatrix} 1 & r & 1 & r \\ 1 & r & -1 & -r \\ r & -1 & r & -1 \\ r & -1 & -r & 1 \end{pmatrix} \begin{pmatrix} \theta_{CommSOFT} \\ \theta_{CommHARD} \\ \theta_{DiffSOFT} \\ \theta_{DiffHARD} \end{pmatrix} \tag{3.14}$$

The ASC model presented in this note has been developed by adopting this particular choice of DOFs for the arm cavities, while for the other mirrors we consider the DOFs given by the simple misalignment of the mirrors. The arm cavity DOFs will be referred to as CH, DH, CS and DS. For the other mirrors, the name of the mirror itself is used to refer to its misalignment: PRM, PR2, PR3, SRM, SR2, SR3, BS. Two additional degrees of freedom are given by the input beam orientation (both angle and position). Two steering mirrors (IN1 and IN2) are placed before PRM, about 1 meter apart. Since the Gouy phase accumulated

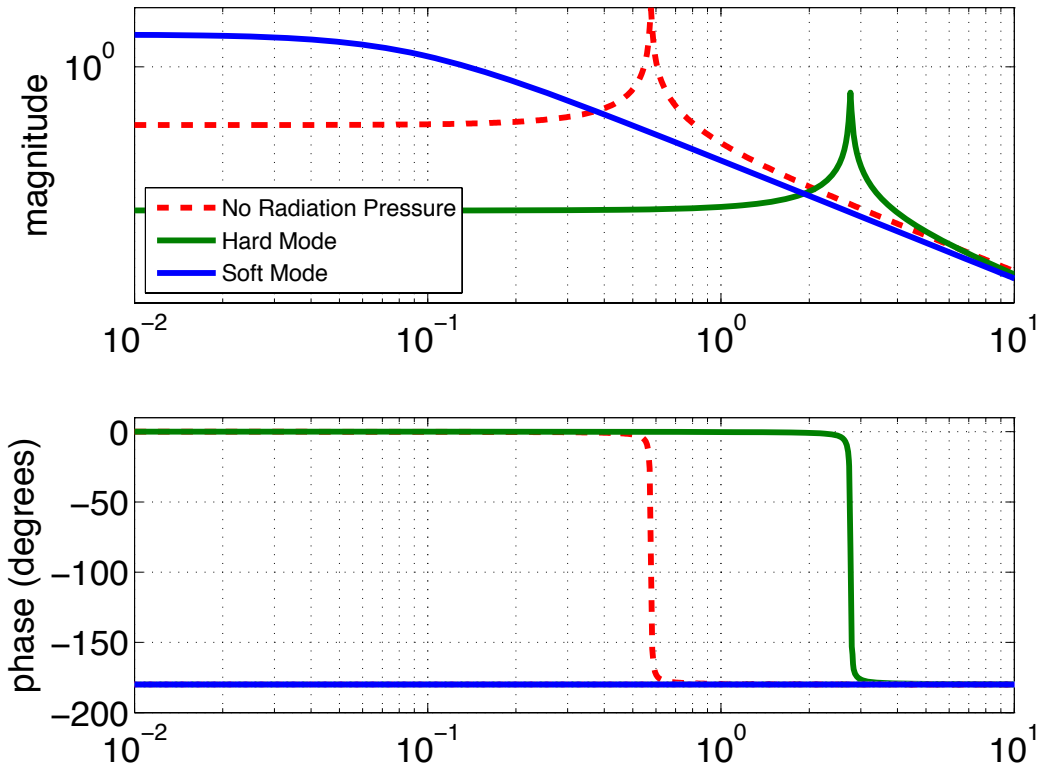

Figure 5: Opto-mechanical transfer functions for the hard and soft mode (in green and in blue) with 720 kW circulating inside the cavity. Only the lowest resonance of the quadruple pendulum suspensions is shown. The dotted red curve shows the same transfer function in absence of radiation pressure.

between these two mirrors is very small, only one global signal can be used to control one of them (IN1 in this model). The other one is locally controlled.

3.5 Quadruple pendulum opto-mechanical transfer functions

In aLIGO, the angular control of the test masses will be done by acting not directly on the mirrors, but on the penultimate mass of the quadruple suspension. The opto-mechanical transfer functions of the quadruple pendulum 'torque of the penultimate mass to PITCH angle of the test mass', for the hard and soft modes of the aLIGO IFO, are shown in figure 8. The impact of radiation pressure is studied for different input powers [3].

[3] As mentioned in the previous section, the intra-cavity power corresponding to 125 W of input power is 720 kW (instead of 770 kW), because the modulation sidebands slightly decrease the effective carrier power entering the IFO.

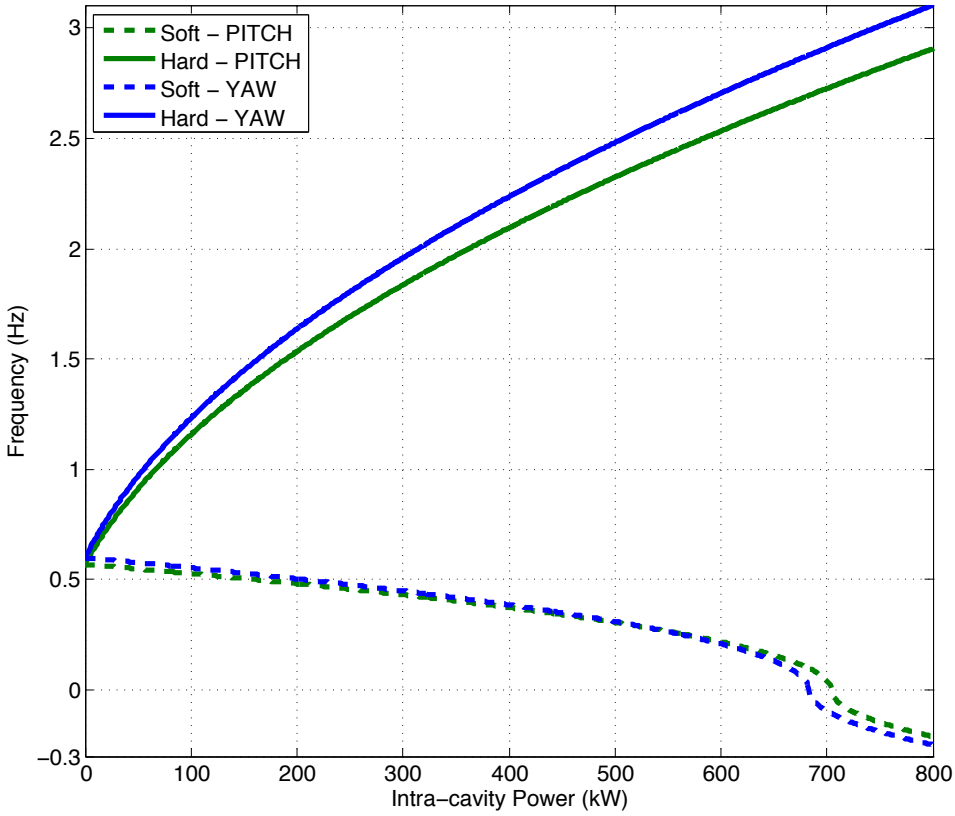

Figure 6: Frequency of the Hard and Soft modes for PITCH and YAW in advanced LIGO, as function of the intra-cavity power.

In the hard mode, the general effect of increasing the power is to shift the resonances to higher frequencies. However, because of the presence of multiple resonances, the shifted resonance can happen to move on top of other resonances, and the shape of the transfer function can significantly change from one power level to another.

For the soft mode, as already seen in section 3.3, the curves show how the lowest resonance becomes unstable when approaching 125 W of input power (or, equivalently in this model, about 720 kW of intra cavity power). The structures around few Hz are instead almost unaffected by the power increase.

4 Sensing Scheme

The alignment sensing scheme designed for aLIGO is based on the LIGO's one. It uses signals which give the relative angular orientation of the mirrors, extracted at the IFO output ports (REFL, AS, POP, TRX, TRY, see Figure 9) through quadrant split photo detectors (QPDs) which sense the position of the beam impinging upon the diode by comparing the amount of light present on each quadrant, and so detecting misalignments both in pitch and

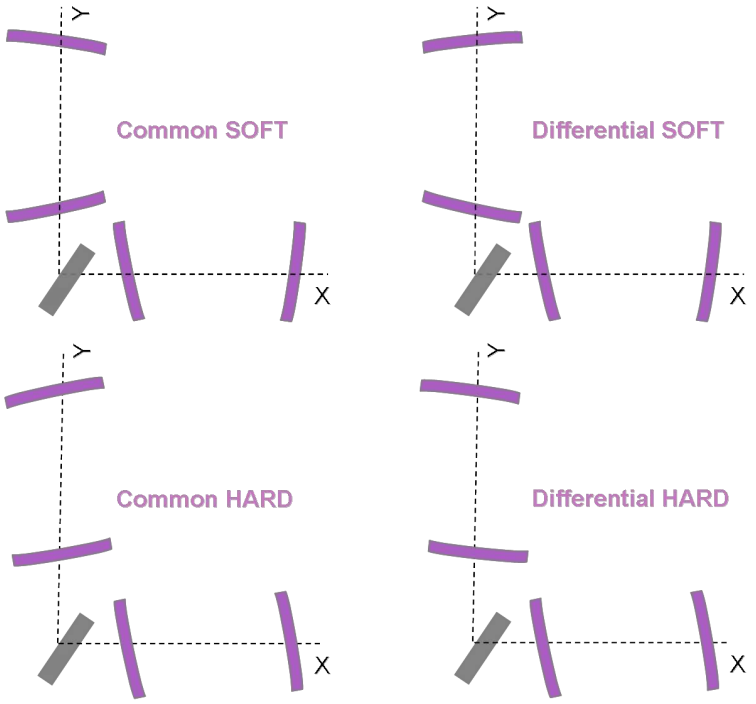

Figure 7: Soft and hard modes in common and differential combinations.

yaw. Moreover, the sensing of angular misalignments is made through a phase modulation-demodulation technique (wavefront sensor, WFS) which allows QPDs to spatially resolve any amplitude modulation present at the phase modulation frequency.

Alignment signals are produced by the interference between the fundamental TEM_{00} Hermite-Gaussian mode of the carrier (sidebands) and the TEM_{01} and TEM_{10} modes of the sidebands (carrier) generated by the misalignment of the IFO optics. The interference signal depends on the relative Gouy phase between the TEM_{00} and TEM_{10} modes, which is a function of the longitudinal position of the detector along the optic axis. For this reason, angular misalignments of different mirrors can be distinguished by placing detectors at different locations along the optical path.

In aLIGO, the maximum power impinging upon each diode will be 50 mW. With 125 W of input power, there will be 50 mW available on each diode, except at the AS port, where 99% of the power will be used for length control. By taking only 1% of the power, only 5 mW will be available for 2 diodes, resulting in 2.5 mW power on each WFS.

All the diodes used in science mode will be placed in vacuum on seismically isolated benches. In particular, suspended benches have been designed in transmission to the arm cavities, inside the BSC chambers. The QPDs which are planned to be use for ASC will be placed on these benches, whose target performance in terms of seismic noise suppression has been designed taking into account the ASC requirements [8].

In this configuration, we study sensitivity of the IFO signals at each port to the angular

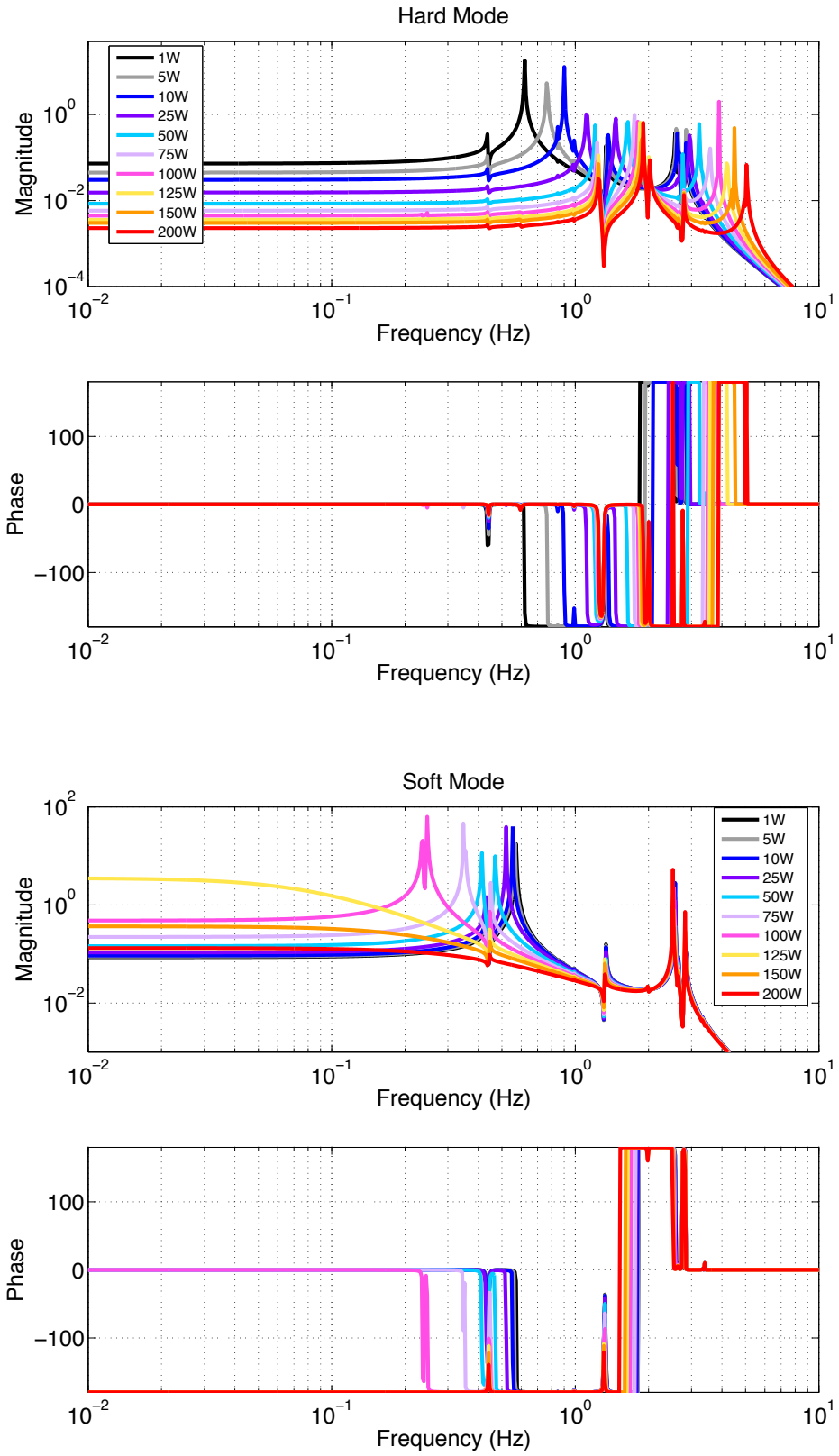

Figure 8: Opto-mechanical transfer functions 'torque of the penultimate mass to PITCH angle of the test mass', of the hard and soft modes in aLIGO, as function of the input power.

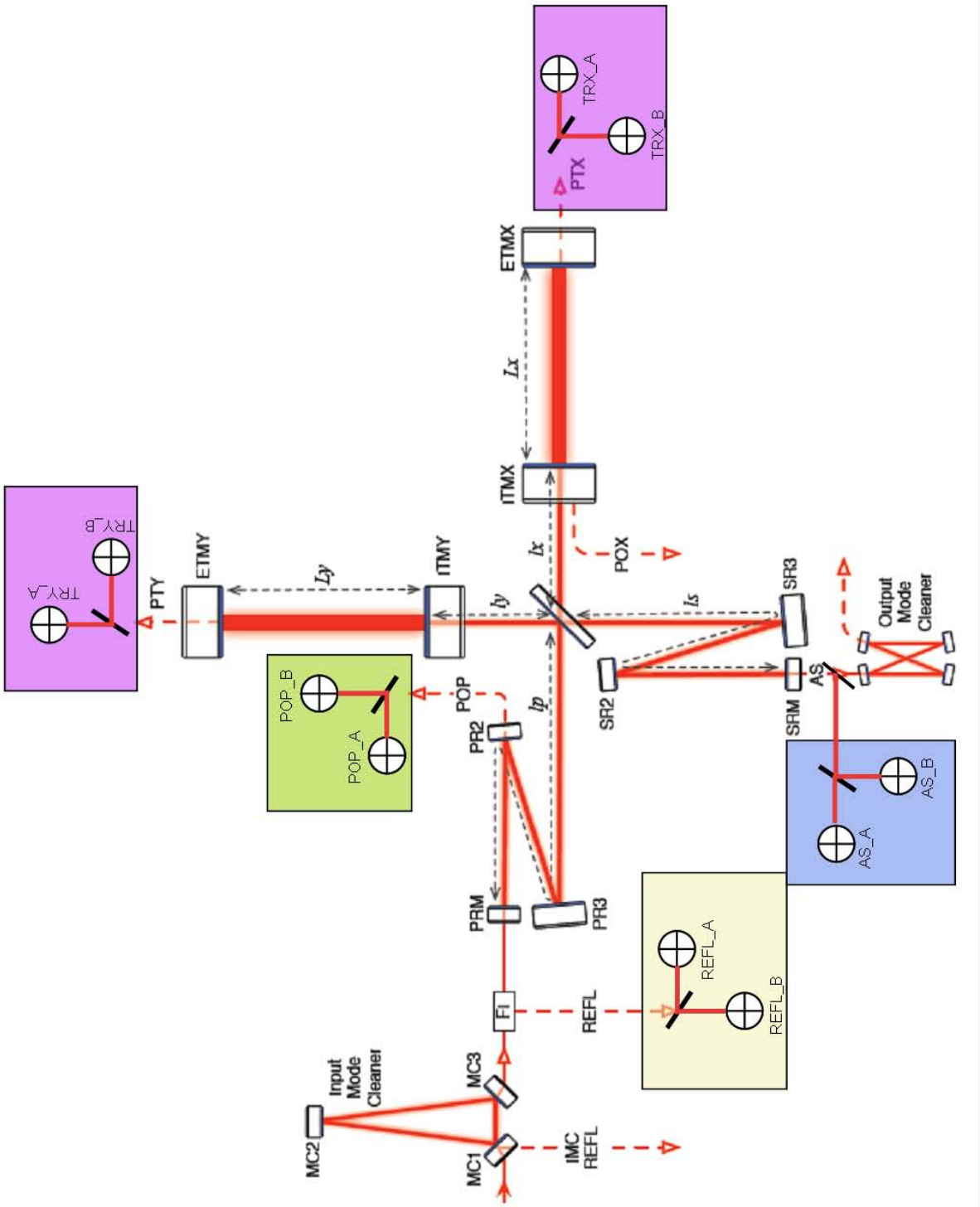

Figure 9: aLIGO alignment sensors.

DOFs (as defined in section 3.4).

4.1 Selection of Error Signals

For each DOF, the amplitude of the signal has been computed (in **W/mrad**), together with the Gouy phase and the demodulation phase (only for RF signals) in which it appears. The Gouy phases and the demodulation phases are expressed in **degrees**. **It is important to point out that the absolute value of the Gouy phases depends on the particular lengths in the readout assumed in this model. The interesting thing is the relative difference between the phases on which the signal appears.**

The largest amplitudes are marked in dark green. The color fades to gray as the amplitude value decreases.

4.1.1 Asymmetric port signals

f1 sidebands are not resonant in the signal recycling cavity. For the signals transmitted to the asymmetric port **AS**, it doesn't make sense therefore to consider f1 demodulation.

	DH	DS	CH	CS	PRM	PR2	PR3	SRM	SR2	SR3	IN1	BS
Gouy Phase	32.0	40.9	31.8	34.6	-68.8	-68.3	-68.3	23.7	41.3	41.2	-68.7	50.8
Amplitude	**-340.0**	-32.0	3.4	-3.9	0.0	0.1	0.9	0.1	1.1	7.2	0.0	**-110.0**

Table 6: **DC Signal: AS**

	DH	DS	CH	CS	PRM	PR2	PR3	SRM	SR2	SR3	IN1	BS
Gouy Phase	39.2	40.9	28.4	36.6	-53.7	-53.4	-53.4	21.6	40.3	40.2	-61.2	43.3
Demod Phase	27.2	22.6	26.5	26.8	83.1	82.8	82.8	23.5	26.4	26.4	62.7	7.3806
Amplitude	**-390.0**	-24.0	1.3	-1.4	0.0	0.0	0.3	0.0	0.4	2.6	0.0	-3.4

Table 7: **RF Signal: AS, f2 demodulation**

	DH	DS	CH	CS	PRM	PR2	PR3	SRM	SR2	SR3	IN1	BS
Gouy Phase	-58.7	-58.6	32.9	32.9	17.8	17.9	17.9	4.5	42.2	42.2	-2.5	-58.5
Demod Phase	76.0	76.4	-13.9	-13.9	-5.4	-5.4	-5.4	-23.2	-17.1	-17.1	-0.9	76.066
Amplitude	**-2.30**	**2.70**	0.06	-0.07	0.00	0.01	0.05	0.00	0.01	0.07	0.00	**1.67**

Table 8: **RF Signal: AS, fM demodulation**

4.1.2 Reflection port signals

Both f1 and f2 sidebands are resonant in the power recycling cavity, and both f1 and f2 demodulated signals are considered at the symmetric port **REFL**, together with the DC signal.

	DH	DS	CH	CS	PRM	PR2	PR3	SRM	SR2	SR3	IN1	BS
Gouy Phase	1.2	4.2	60.8	69.5	-8.1	56.9	57.3	-74.0	-74.0	-74.0	-42.4	58.7
Amplitude	0.3	-1.0	**906.5**	13.8	-5.1	5.8	56.4	0.0	0.0	0.1	5.2	19.6

Table 9: **DC Signal: REFL**

	DH	DS	CH	CS	PRM	PR2	PR3	SRM	SR2	SR3	IN1	BS
Gouy Phase	-40.2	-23.3	-32.9	-28.8	-68.3	-27.3	-27.2	79.8	79.8	79.8	47.7	-27.2
Demod Phase	-16.6	-14.6	-17.5	-16.5	-17.1	-16.1	-16.1	-15.4	-15.4	-15.4	-17.7	-16.1
Amplitude	-0.4	0.4	**211.8**	**37.9**	-2.0	-5.4	**-45.5**	0.0	0.0	0.0	-1.3	-15.5

Table 10: **RF Signal: REFL, f1 demodulation**

	DH	DS	CH	CS	PRM	PR2	PR3	SRM	SR2	SR3	IN1	BS
Gouy Phase	-41.6	-40.6	-32.8	-28.4	-65.4	-27.5	-27.4	73.0	73.0	73.0	48.1	-28.4
Demod Phase	-69.5	-69.7	-66.4	79.4	-81.5	69.8	68.9	8.6	8.6	8.6	-57.0	59.8
Amplitude	-3.4	3.9	**120.3**	**-23.9**	-1.1	3.8	**32.5**	0.0	0.1	0.5	-0.8	9.6

Table 11: **RF Signal: REFL, f2 demodulation**

4.1.3 Central cavity signals

For the pick-off signal extracted in transmission of the PR2 mirror, here is the table showing the sensitivity of the DC and RF signals to the different DOFs.

	DH	DS	CH	CS	PRM	PR2	PR3	SRM	SR2	SR3	IN1	BS
Gouy Phase	-44.5	-22.3	-33.8	-32.5	78.7	-46.5	-40.9	-87.0	-87.0	-87.0	70.0	-38.4
Amplitude	0.2	-0.2	**-129.8**	-5.7	-1.0	-0.1	-1.8	0.0	0.0	0.0	0.0	-0.8

Table 12: **DC Signal: POP**

	DH	DS	CH	CS	PRM	PR2	PR3	SRM	SR2	SR3	IN1	BS
Gouy Phase	-39	-53.2	54.6	57.7	57.7	57.9	58	55.1	55.1	55.1	33.9	57.9
Demod Phase	72.4	36.8	-36.5	-36.6	-36.6	-36.6	-36.6	-38.4	-38.4	-38.4	-35.9	-36.6
Amplitude	-0.0	0.0	**-4.7**	**-4.0**	0.1	**0.7**	**6.3**	0.0	0.0	0.0	0.0	**2.2**

Table 13: **RF Signal: POP, f1 demodulation**

	DH	DS	CH	CS	PRM	PR2	PR3	SRM	SR2	SR3	IN1	BS
Gouy Phase	43.7	43.9	54.3	58.2	57.7	58	58	-22	-22	-22	44.2	57.1
Demod Phase	8.2	8.3	-32.8	-32.5	-32.3	-32.5	-32.5	85.8	85.8	85.8	-47.6	-41.5
Amplitude	**-0.5**	**0.6**	**3.3**	**2.8**	-0.1	**-0.5**	**-4.5**	-0.0	-0.0	-0.1	-0.0	**-1.3**

Table 14: **RF Signal: POP, f2 demodulation**

4.1.4 Arm transmitted signals

Signals transmitted trough the arm cavity have been investigated as well. Since both f1 and f2 are not resonant inside the arms, only DC signals can be useful.

	DH	DS	CH	CS	PRM	PR2	PR3	SRM	SR2	SR3	IN1	BS
Gouy Phase	14.1	-79.8	13.9	-80.2	-0.3	0.1	0.1	16.0	16.0	16.0	-10.0	33.2
Amplitude	**116.9**	**-25.5**	**120.3**	**-25.5**	-0.0	-0.0	-0.4	0.0	0.0	0.0	0.0	-0.0

Table 15: **DC Signal: TRX**

	DH	DS	CH	CS	PRM	PR2	PR3	SRM	SR2	SR3	IN1	BS
Gouy Phase	14.1	-79.8	13.9	-80.2	-0.3	0.1	0.1	16.0	16.0	16.0	-10.0	-0.75
Amplitude	**-119.4**	**26.1**	**122.8**	**-26.1**	-0.0	-0.0	-0.4	0.0	-0.0	-0.0	0.0	-0.3

Table 16: **DC Signal: TRY**

4.2 Sensing Matrix

In aLIGO there will be at least two WFSs at each port of the IFO from which alignment error signals are planned to be extracted. In order to be able to finely tune the Gouy phase of the two detectors, the strategy will be to separate them by 90° of Gouy phase, and then digitally combine the signals to have the wanted Gouy phase. The suffixes used to identify the two detectors at each port are $\_A$ and $\_B$. The tuning of demodulation phase will be done digitally as well, in the same way it is currently done in eLIGO. The letters I and Q will be used to identify the in-phase and quadrature-phase signals. The demodulation frequency

will be written as 1 (f1 9 MHz), 2 (f2 45 MHz) or M (f2 - f1 36 MHz) (see table 2 for accurate values of the frequencies).

On the basis of the previous tables, we choose the signals to use in the sensing scheme. As it is shown in the next section, the PR2 and SR2 mirrors are not sensed (nor globally controlled) in this scheme, as their coupling to DARM is small enough that they can be left under local control, as it will be shown in the following sections. For sensing the other 10 DOFs, 10 independent signals (5 RF and 5 DC) have been chosen.

Port	DC Signals	RF Signals
TRX, TRY	2	0
AS	1	2
REFL	0	3
POP	2	0

(4.1)

On the basis of the signal sensitivity to the IFO DOFs (cfr tables in section 4.1), the Gouy phases have been tuned in the following way:

Port	*Sensor*	*GouyPhase(dg)*	*Tuning*	*A∠B(dg)*
TRX, TRY	A	14	$Max\ DH$	90
	B	-76	$Min\ DH$	
AS	A	23.7	$Max\ SRM$	100
	B	122.5	$Max\ BS$	
$REFL$	A	147.2	$Max\ CH$	90
	B	57.2	$Min\ CH$	
POP	A	139.1	$Max\ PRM$	60
	B	78.7	$Max\ PR3$	

(4.2)

The demodulation phase of the RF signals have been set in order to maximize the sensitivity to the given DOF on I for the common signals, and on Q for the differential ones:

Sensor	*Demdofreq*	*DemodPhase(dg)*	*Tuning*
AS_B	fM	166.2	$Max\ BS\ on\ Q$
AS_A	$f2$	117.1	$Max\ DH\ on\ Q$
$REFL\_A$	$f1$	-17.5	$Max\ CH\ on\ I$
$REFL\_B$	$f2$	-85.1	$Max\ SR3\ on\ Q$

(4.3)

The sensitivity of the selected signals with respect to the IFO DOFs is shown in the sensing matrix, where all the amplitudes are in **W/mRad**:

Signals/DOFs	*CS*	*CH*	*DS*	*DH*	*PRM*	*PR2*
TR_DC Comm	**-36.4**	0.3	0.4	0	0	0
REFL_A I1	**-37.8**	**-211.8**	−0.4	0.4	1.6	5.3
TR_DC Diff	0.4	0	**-36.4**	−0.2	0	0
AS_A Q2	1.4	−1.3	23.0	**374.6**	0	0
POP_B DC	1.4	**35.1**	0	−0.1	−0.7	0
REFL_B Q2	**-0.6**	**-0.4**	**-1.0**	**0.9**	**0.4**	0.1
POP_A DC	4.0	**91.1**	0.1	−0.1	−0.4	0.1
AS_A DC	−2.7	2.4	−21.4	**-237.5**	0	0
REFL_B I2	**0.8**	**-4.6**	−0.4	0.4	**0.6**	−0.2
AS_B QM	0	0	**2.7**	**-2.3**	0	0

(4.4)

Signals/DOFs	*PR3*	*SRM*	*SR2*	*SR3*	*IN1*	*BS*
TR_DC Comm	−0.1	0	0	0	0	0
REFL_A I1	**45.3**	0	0	0	0.2	15.5
TR_DC Diff	0	0	0	0	0	0
AS_A Q2	0	0	−0.4	−2.5	0	2.9
POP_B DC	0.6	0	0	−0.0	0	0.2
REFL_B Q2	**0.6**	0	0.1	**0.5**	**-0.4**	**-0.6**
POP_A DC	1.3	0	0	0	0	0.5
AS_A DC	0	0.1	0.7	4.8	0	−7.0
REFL_B I2	**-1.8**	0	0	0	**-0.7**	**-0.9**
AS_B QM	0	0	0	0	0	**1.7**

(4.5)

All the signals are dominated by the arm cavity motion. This fact is very inconvenient, especially in the initial commissioning phase. In fact, the reconstruction of the all DOFs, which goes trough the inversion of the sensing matrix, requires a precise measurement of the sensing matrix itself and this is possible only once the loops are already closed. In order to close the alignment loops, the easiest way would be to have a sensing matrix as diagonal as possible, so that each loop can be treated independently.

The approach followed here is to have a *two steps* alignment scheme:

- **acquisition mode**: the arm cavity DOFs are closed with high bandwidth loops ($\approx 1Hz$) and high low frequency gain, while a slow drift control ($\approx 100mHz$) is used for the central cavity DOFs. The idea is that in the bandwidth of the drift control the gain of the arm cavity loops will be much higher, so that the motion of the arm cavity DOFs at frequencies within the loop bandwidth won't affect much the central cavity DOFs. This allows us to have a close to diagonal sensing matrix, with the drawback of poor performance, as the reconstruction of the DOFs is not accurate;
- **science mode**: the full sensing matrix is measured in the "pre-aligned" state, and the main non-diagonal terms are included. The gain of the loops is increased as needed in order to reduce the angular noise coupling to DARM (see the following sections for details).

Before entering into the details of the control scheme of the two modes of operation, in the next section we describe the architecture of the ASC model.

5 Architecture of the ASC model

The architecture of the ASC model is summarized in Figure 10. Each block corresponds to a matrix, while the white labels identify signal vectors. The signal flow can be described as follows, with capitalization used to identify the signal vectors and the matrices according to Figure 10:

- the angular motion of the `MIRRORS` causes the `SENSOR` signals to change, accordingly to the IFO response, which includes radiation pressure effects;
- the sensor signals can be combined through an `INPUT MATRIX` to define the `ERROR` signals for the angular degrees of freedom of the IFO;
- the error signals are filtered by the `CONTROL FILTERS` and the resulting `CONTROL` signals are mapped to mirror `CORR`ection signals, which are then filtered to take into account the particular mirror response and sent to the actuators;
- the mechanical `PENDULUM RESPONSE` translates the actuation force to angular motion of the `MIRRORS` [4].

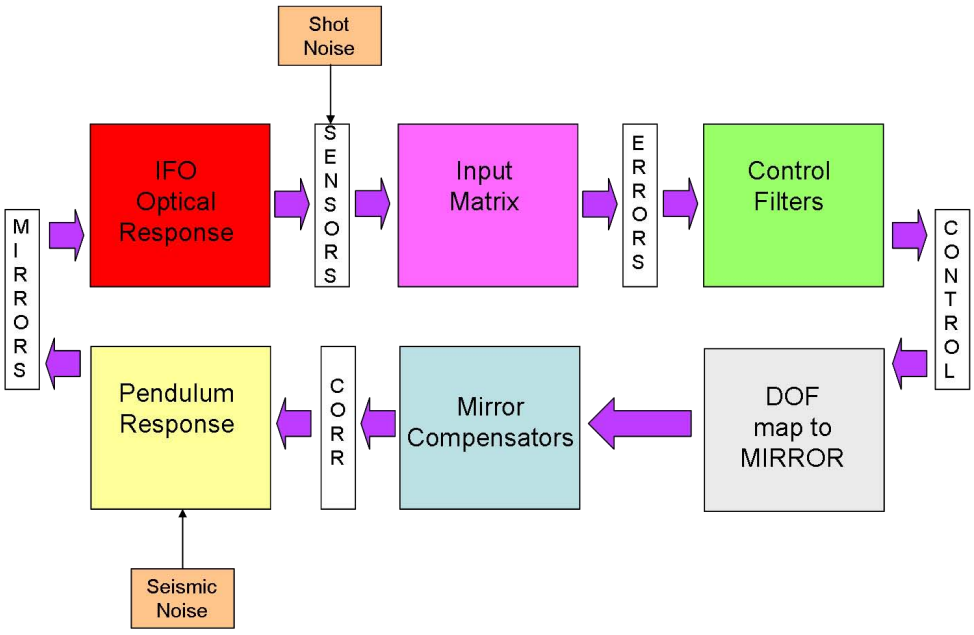

Figure 10: Architecture of the ASC model. The colorful blocks correspond to matrices, while the white labels correspond to signal vectors.

The matrices which define the model are built in the following way:

[4] In aLIGO the alignment correction signals will be applied not directly to the mirror, but to the previous stage of the suspension (penultimate mass).

- the Optickle model provides the transfer functions which simulate the `IFO Optical Response`;
- the `Input Matrix` has to be computed in order to reconstruct the error signals of the angular DOFs;
- the `Control Filters` and `Mirror Compensators` are designed to obtain the desired performance;
- the common and differential hard and soft matrix described in section 3.4 defines the angular DOF basis which diagonalizes the torque stiffness matrix in presence of radiation pressure (`DOF map to MIRROR`);
- the pendulum response is based on precise models of the aLIGO suspensions [7].

The noises included in the model (seismic noise and shot noise) are described in the next section.

5.1 Input noises: seismic noise and shot noise

Two fundamental noises which limit the ASC noise performance are considered in this model: the angular seismic noise of the optics and the shot noise of the sensors. Other kind of noises, such as electronic noise and acoustic noise, which have been polluting the alignment signals in first generation detectors, are neglected here. The reason for it is that in aLIGO the ASC electronics will be designed so as to have, for each signal, the electronic noise below the shot noise, and all the diodes used in science mode will be placed under vacuum. The assumption that seismic noise and shot noise will be the dominant noise sources of the alignment signals is therefore at least plausible.

5.1.1 Seismic noise

The angular seismic noise of the optics used as input to this model is shown in Figure 11. For each optic, an estimate of the pitch noise transferred to the mirrors has been made based on current measurements and models of the aLIGO suspensions (see appendix C for details). The ground motion included in this model is taken from an analysis made on the S5 data [11]. The level of the seismic noise used here is the 90th percentile, that is, the seismic noise during S5 was higher than this 90% of the time.

5.1.2 Shot noise

For each sensor, the limiting noise is assumed to be shot noise:

$$\widetilde{P}_{Shot} = \sqrt{2 \times h_P \times \nu \times P_{DC}} \quad W/\sqrt{Hz} \tag{5.1}$$

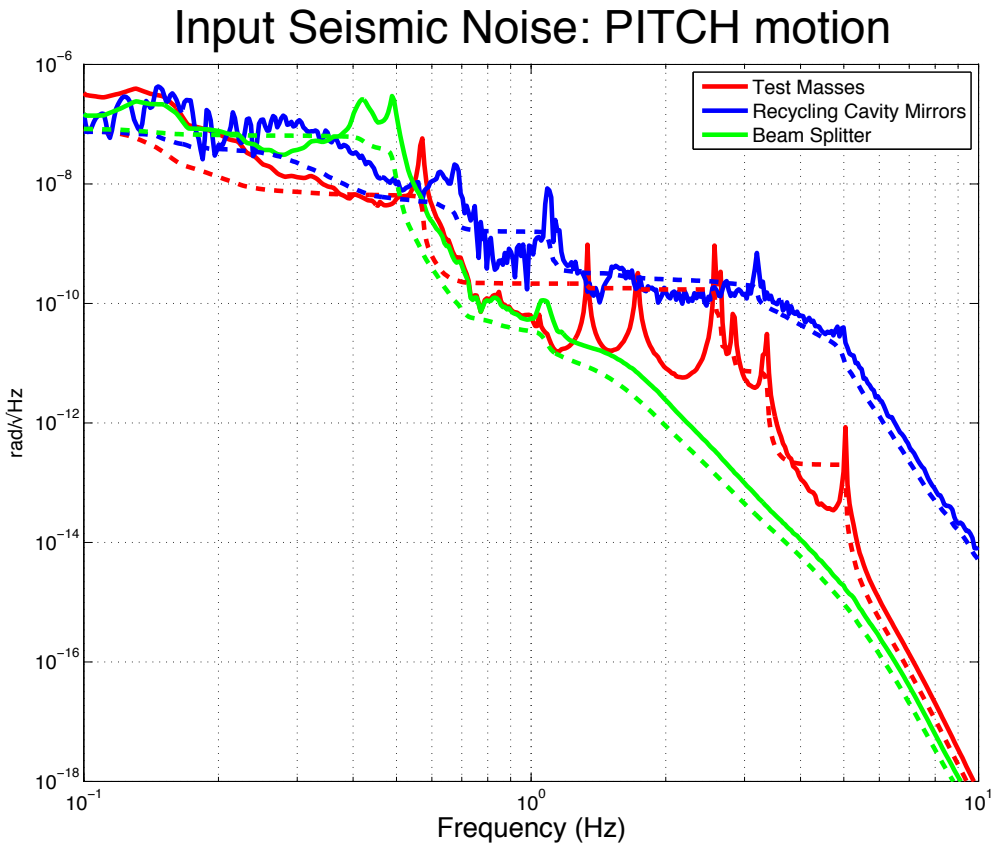

Figure 11: Angular pitch motion of all the IFO mirrors under local controls. The curves assume that the presence of sensing noise introduced by the damping loops will reintroduce noise only below 10 Hz.

where $h_P = 6.626 \times 10^{-34}\ Js$ is Planck's constant and $\nu = 2.817 \times 10^{14}$ Hz is the frequency of the laser light. P_{DC} is the power impinging upon the diode. The model is tuned so as to have 50 mW on each diode, which is the maximum power which the aLIGO WFS's and QPD's will be able to handle. Only the diodes at the AS port have less power, as only 1% of the power is sent to the WFSs, resulting in about 2.5 mW on each diode with 125 W of input power.

5.2 Angular noise coupling to DARM

In order to evaluate the performance of the ASC scheme, it is crucial to determine how much noise is introduced in the detection frequency band (above 10 Hz for aLIGO) due to the angular mirror motion.

The coupling of angular mirror motion to the length of a cavity is usually understood from a geometrical argument. For a static mirror angle θ_{Mirror} and a static beam spot offset d_{Spot}, the change in length of a cavity ΔL, is given by:

$$\Delta L = d_{Spot} \times \theta_{Mirror} \tag{5.2}$$

where the beam spot offset is referred to the mirror's center of rotation and the mirror angle is referred to the input beam to the cavity. In general, both d_{Spot} and θ_{Mirror} are frequency dependent, and their are usually referred to as beam spot motion (BSM) and residual angular mirror motion. This bilinear process in which the BSM on each mirror causes the angular mirror motion θ_{Mirror} to produce a length signal is mathematically expressed by the convolution of the two spectra:

$$\hat{\Delta L}(f) = \hat{d}_{Spot}(f) * \hat{\theta}_{Mirror}(f) \tag{5.3}$$

A good approximation of the convolution product is given by:

$$\hat{\Delta L}(f) = \hat{d}_{Spot}(f) * \hat{\theta}_{Mirror} \approx \hat{d}^{RMS}_{Spot} \times \hat{\theta}_{Mirror}(f) + \hat{\theta}^{RMS}_{Mirror} \times \hat{d}_{Spot}(f) \tag{5.4}$$

In order to evaluate the angular noise coupled to DARM, we need therefore to compute the length variation produced by each mirror, i.e. the product of the RMS of the beam spot motion on each mirror times the residual angular motion of the mirror, plus the RMS of the residual angular motion of each mirror times the beam spot motion.

For the arm cavity mirrors, the length change produced by the angular motion is directly a change of the DARM length. This fact can be summarized by saying that the coupling factor is 1. For the mirrors outside the arm cavities, we use the following coupling factors [4]:

- BS: $\pi/2F \sim 1/280$;
- PRC mirrors: $1/100$;
- SRC mirrors: $1.2 \times 10^{-2} \times \left(\frac{10Hz}{f}\right)^2$

5.3 Beam Spot Motion (BSM)

In order to calculate the beam spot motion, is useful to think about the angular noise coupling to DARM as the coupling of mirror angular motion through the conversion of an incident TEM_{00} field in the cavity. To first order, TEM_{00} is produced by angular motion through the conversion of an incident TEM_{01} or TEM_{10} mode, so that its amplitude variation is:

$$\Delta A_{00} = \frac{-2i\alpha}{\theta_0}\left(\theta_x A_{01} + \theta_y A_{10}\right) \tag{5.5}$$

where θ_0 is the incident beam's divergence angle and $\alpha = \sqrt{1 + z_{beam}^2/z_0^2} = w_{beam}/w_0$ is the ratio of the beam size at the mirror and the beam waist size. As we have done elsewhere, we will focus on the θ_x motion and ignore θ_y as its behavior is identical.

The modulation of the outgoing field produced by ΔA_{00} can be found by

$$A_{00}e^{i\phi} = A_{00} + \Delta A_{00} \tag{5.6}$$

$$A_{00}e^{i\phi} \simeq A_{00}(1 + i\phi) \tag{5.7}$$

$$\Rightarrow \phi \simeq -i\frac{\Delta A_{00}}{A_{00}} = \frac{-2\alpha}{\theta_0}\frac{A_{01}}{A_{00}}\theta \tag{5.8}$$

with the last step from equation 5.5. Going on to relate this to equivalent mirror displacement we will use [5]:

$$\Re(\phi) = -kz$$

with $k = 2\pi/\lambda$. This yields:

$$z = \frac{\alpha\lambda}{\pi\theta_0}\Re\left(\frac{A_{01}}{A_{00}}\right)\theta = \alpha\, w_0 \Re\left(\frac{A_{01}}{A_{00}}\right)\theta = d_{Spot}\theta \tag{5.9}$$

where we have related the beam waist size to the divergence angle by $w_0 = \lambda/(\pi\theta_0)$, and used the fact that beam spot displacement on the mirror is given by:

$$d_{Spot} = w_{beam}\Re(A_{01}/A_{00})$$

.

5.4 Coupling of mirrors in the signal recycling cavity

The advantage of the approach presented in the previous section is that it lets us compute the contributions from mirrors outside of the cavity as well. Take the signal recycling mirror (SRM) for example; the BSM on the mirror is given by the ratio of incident TEM_{01} and TEM_{00} modes, but while the TEM_{00} field is determined by the interferometer's offset from the dark fringe and may even approach zero, the equivalent displacement noise of this mirror's

[5] Taking the real part explicitly drops the amplitude modulation produced by angular motion, which cannot be represented by an equivalent mirror displacement.

angular motion clearly does not go to infinity, as the geometrical argument that lead to equation 5.2 would imply.

We can relate the angular motion of the SRM to equivalent motion of an arm cavity mirror by observing that:

$$\phi_{arm} \simeq \frac{\phi_{BS}}{\mathcal{F}} \simeq \frac{\phi_{SRM}}{\mathcal{FC}} \simeq \frac{-i}{\mathcal{FC}} \frac{dA_{00}}{A_{00SRM}} \tag{5.10}$$

where $\mathcal{F}$ is the cavity finesse and $\mathcal{C} = A_{00BS}/A_{00SRM}$ is the contrast which relates the TEM_{00} field amplitude on the beam-splitter to that on the SRM. Taking this one step further:

$$\phi_{arm} \simeq \frac{d_{SRM}\theta_{SRM}}{\mathcal{FC}} \tag{5.11}$$

if $\mathcal{C}$ is real, which is usually isn't.

In fact, in the case of the signal recycling cavity we know what $\mathcal{C}$ is almost entirely imaginary, as the A_{00SRM} at the dark port is produced by the difference of the A_{00} fields reflected from the arms, which are almost parallel. Their difference is therefore orthogonal to the fields themselves, causing the coupling of these mirrors to result from their production of amplitude modulation, besides the coupling due to phase modulation. Going back to equation 5.8 and assuming that $\mathcal{C} = i|\mathcal{C}|$, we can see that:

$$\Re(\phi_{arm}) \simeq \frac{-1}{\mathcal{F}|\mathcal{C}|}\Re\left(\frac{\Delta A_{00}}{A_{00SRM}}\right) = \frac{2\alpha}{\mathcal{F}|\mathcal{C}|\theta_0}\Im\left(\frac{A_{01}}{A_{00SRM}}\right)\theta_{SRM} \tag{5.12}$$

$$\Re(\phi_{arm}) \simeq \frac{2\theta_{inc}\alpha^2}{\mathcal{F}|\mathcal{C}|\theta_0^2}\theta_{SRM} \tag{5.13}$$

where θ_{inc} is the angle of the incident beam on the SRM. Thus, for the mirrors in the signal recycling cavity, not only the beam spot motion is relevant, but also the beam angular motion (BAM) plays the role of coupling angular noise to the DARM readout.

6 ASC configurations

aLIGO will operate over a range of different input powers, and, at least in the first part of the commissioning phase, also different optical configurations will be adopted: the baseline layout with signal recycling and a iLIGO-like configuration without signal recycling mirror. In order to explore these different states, we run the ASC model for:

- aLIGO with maximum power (125 W input power);
- aLIGO with 25 W input power;
- iLIGO-like optical layout with 25 W input power.

For each configuration, the ASC performance will be described in terms of the following figures of merit (FOMs):

- the residual angular motion of each mirror under alignment control;
- the beam spot motion on each mirror, caused by the motion of all the mirrors;
- the angular noise coupling to DARM;
- the contribution of each mirror to the total seismic angular noise coupled to DARM.

For aLIGO at maximum power, we describe also a possible 'acquisition mode', characterized by an easy-to-measure diagonal input matrix, which on the other hand provide a poor reconstruction of the angular DOF and low loop gains, and therefore a not optimal angular motion suppression.

7 aLIGO with maximum power (125 W)

7.1 Acquisition Mode

The acquisition mode input matrix is derived from the matrix in section 4, by zeroing all the off-diagonal terms and taking the inverse: Units are **mrad/W**.

	TR Comm	REF A I1	TR Diff	AS A Q2	POP B DC	POP A DC	AS A DC	REF B Q2	REF B I2	AS B QM
CS	**-0.03**	−0	0	0	0	0	0	0	0	0
CH	0	−0.005	0	0	0	0	0	0	0	0
DS	0	0	**-0.03**	0	0	0	0	0	0	0
DH	0	0	0	**0.003**	0	0	0	0	0	0
PRM	0	0	0	0	**-1.41**	0	0	0	0	0
$PR3$	0	0	0	0	0	**0.79**	0	0	0	0
SRM	0	0	0	0	0	0	**11.11**	0	0	0
$SR3$	0	0	0	0	0	0	0	**2**	0	0
$IN1$	0	0	0	0	0	0	0	0	**-1.43**	0
BS	0	0	0	0	0	0	0	0	0	**0.59**

(7.1)

All the loops except the arm cavity ones are controlled with a low bandwidth drift control. This fact justifies the removal of all the off-diagonal terms in the first 4 columns, since the corresponding elements will be reduced by the gain of the arm loops, which run at high bandwidth. The other big terms which appeared in the sensing matrix in section 4 have

been neglected, with the drawback that the reconstruction of the IFO DOFs is not exact. The angular loops will tend to zero the error signals, which however don't correspond to the real motion of the mirrors, resulting in a poor suppression of the effective mirror angular motion.

The open loop and closed loop transfer functions are shown in figure 12. The scheme proposed here does not control the PR2, SR2 and SRM mirrors, which are kept under local control. As mentioned before, all the loops except the arm cavity ones have a very small bandwidth (about 100 mHz). The control filters have been designed so as to have at least 40 dg of phase margin.

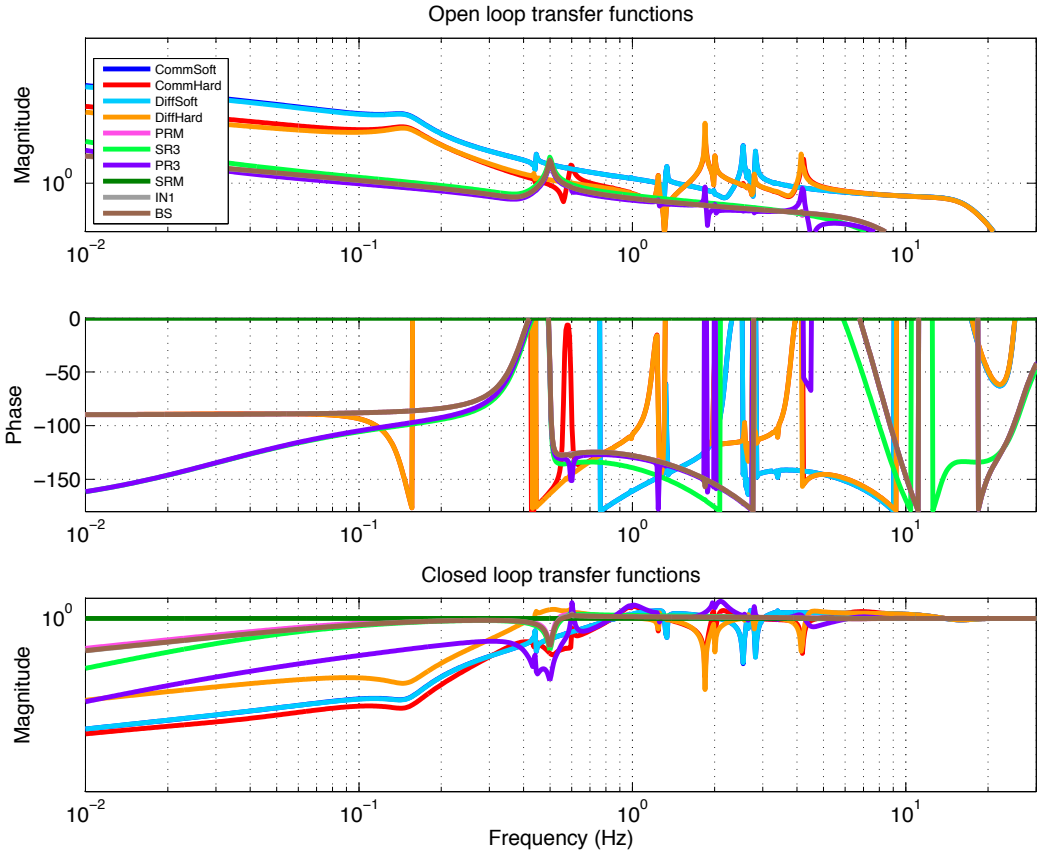

Figure 12: Open loop and closed loop transfer functions of the angular DOF loops in ACQUISITION MODE.

In order to evaluate the goodness of the reconstruction, we compare the frequency-dependent suppression of the mirror motion expected from the diagonal terms of the open loop transfer function matrix with the one computed by taking correctly into account the not diagonal terms. If the ratio is close to one, it means that the cross-coupling between the DOFs is small. If the ratio differs from one it means that the off-diagonal terms are not negligible,

or, in other words, the input matrix did not do a good job in diagonalizing the system. Figure 13 shows this ratio for the 10 angular DOFs. With the diagonal input matrix, the plot shows that the reconstruction of the DOFs is not particularly good, especially at low frequency.

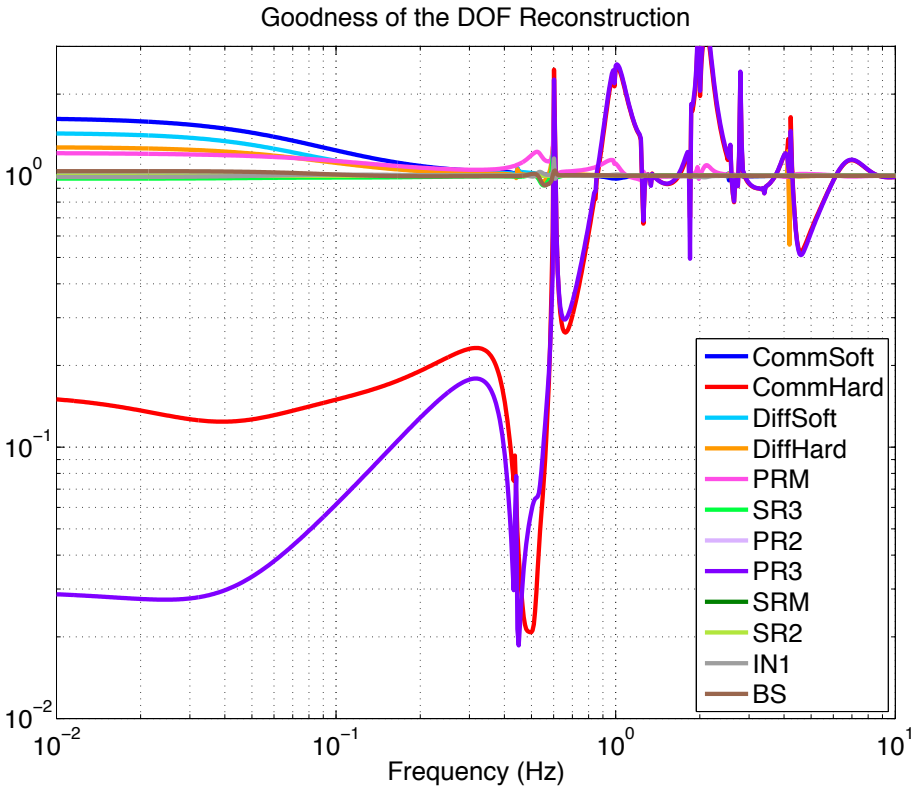

Figure 13: Measurement of the goodness of the reconstruction of the angular DOFs in the ACQUISITION MODE. The plot shows the ratio between the suppression of the mirror motion expected from the diagonal terms of the open loop transfer function matrix with the one computed by taking correctly into account the not diagonal terms. The reconstruction is optimal when the ratio is 1.

7.1.1 ASC FOMs: aLIGO maximum power, acquisition mode

The performance of the ASC in this configuration (standard aLIGO signal-recycled IFO, 125 W of input power) is described by the FOMs: figure 14 shows the residual angular motion of each mirror with the angular loops closed, figure 15 shows the beam spot motion on each optic.

The design sensitivity of aLIGO is shown by the dotted black line in figure 16. A conservative approach requires us to have all the noise contribution at least a factor 10 below

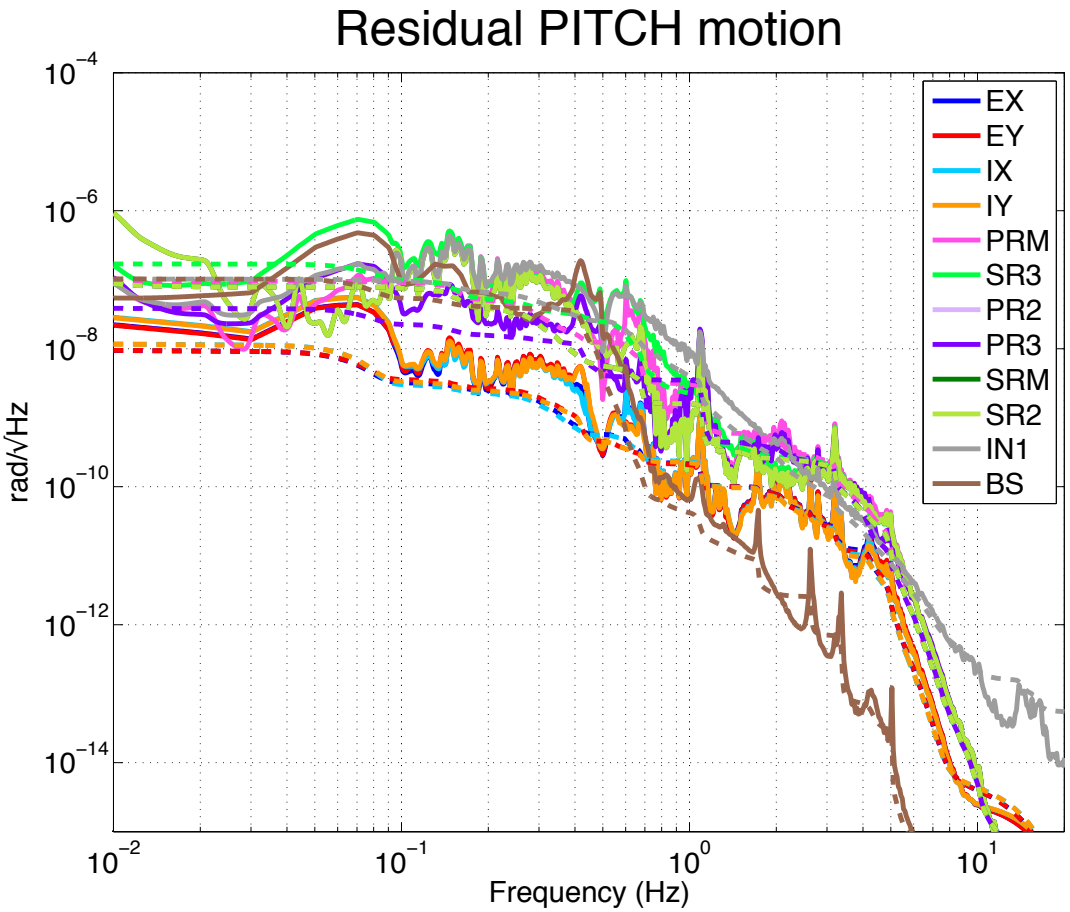

Figure 14: Residual angular motion of each optic in ACQUISITION MODE.

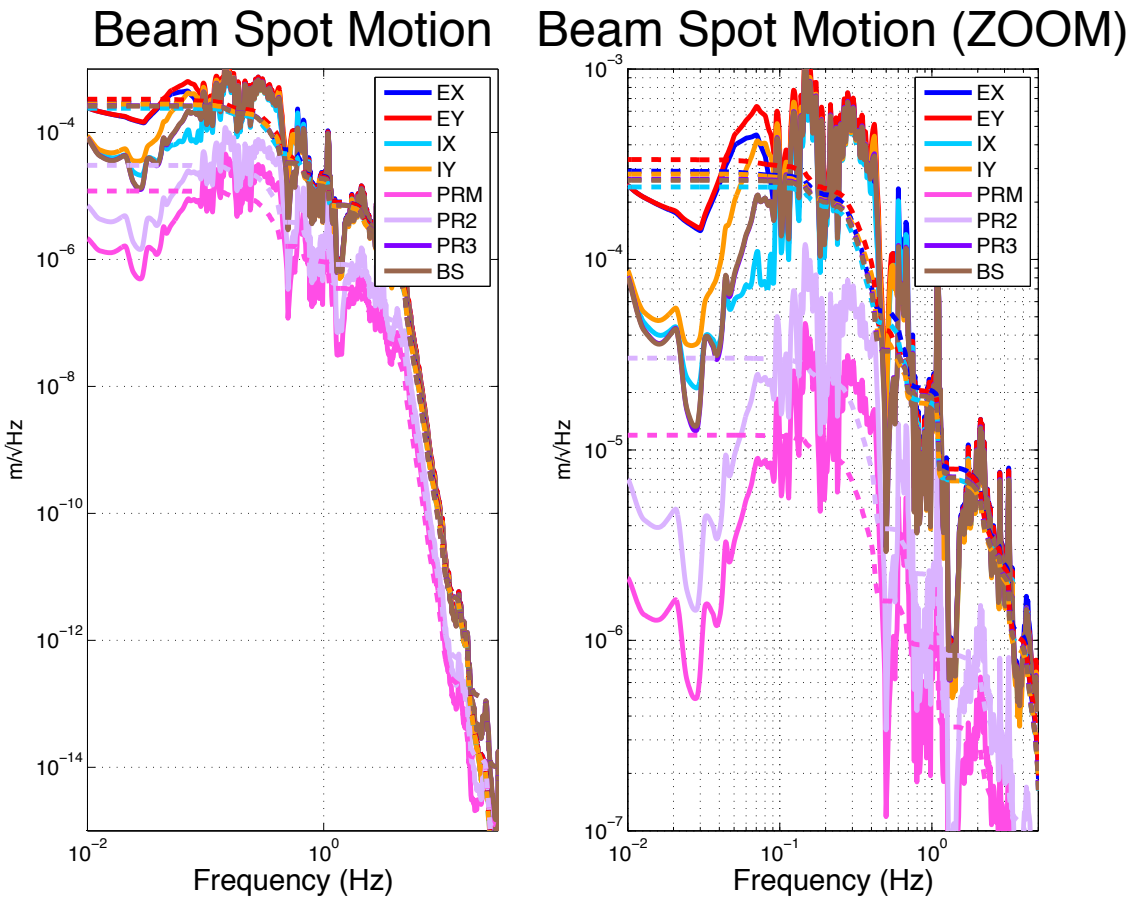

Figure 15: Beam Spot Motion (BSM) on each optic in ACQUISITION MODE.

the goal (dotted red line), but we aim to meet this target only in science mode. The noise resulting from acquisition mode control exceeds the science mode target below 20 Hz, while the performance at higher frequencies is compatible with low noise operations.

The noise contribution below 20 Hz comes from the sensor noise of the transmitted signals, and the residual angular seismic motion. The sensor noise could be reduced by reducing the frequencies of the cut-off filter poles, which are intentionally kept high in order to have a robust control scheme with plenty of phase margin. Figure 17 shows which optics contribute to the seismic noise. The dominant sources are the SR3 mirror and the end mirrors.

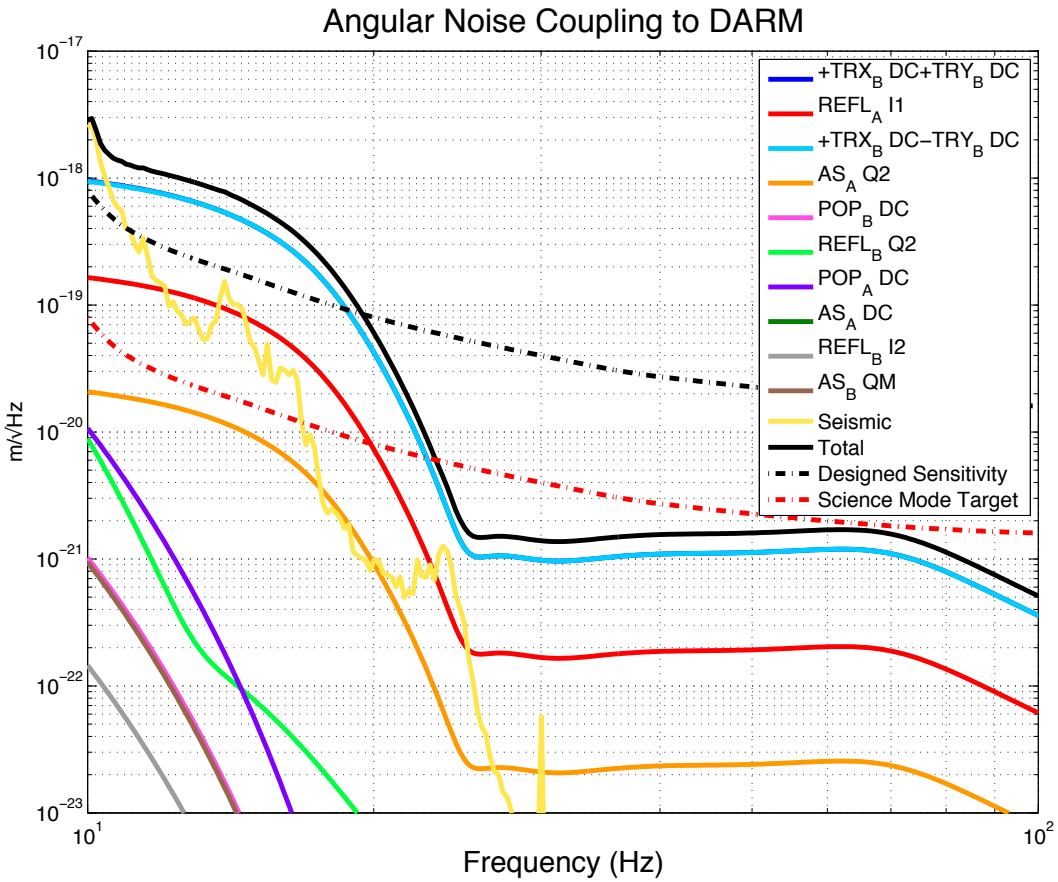

Figure 16: Angular noise coupling to DARM in ACQUISITION MODE. The yellow curve represents the sum of the seismic noise contribution from all the mirrors (see figure 17 for details).

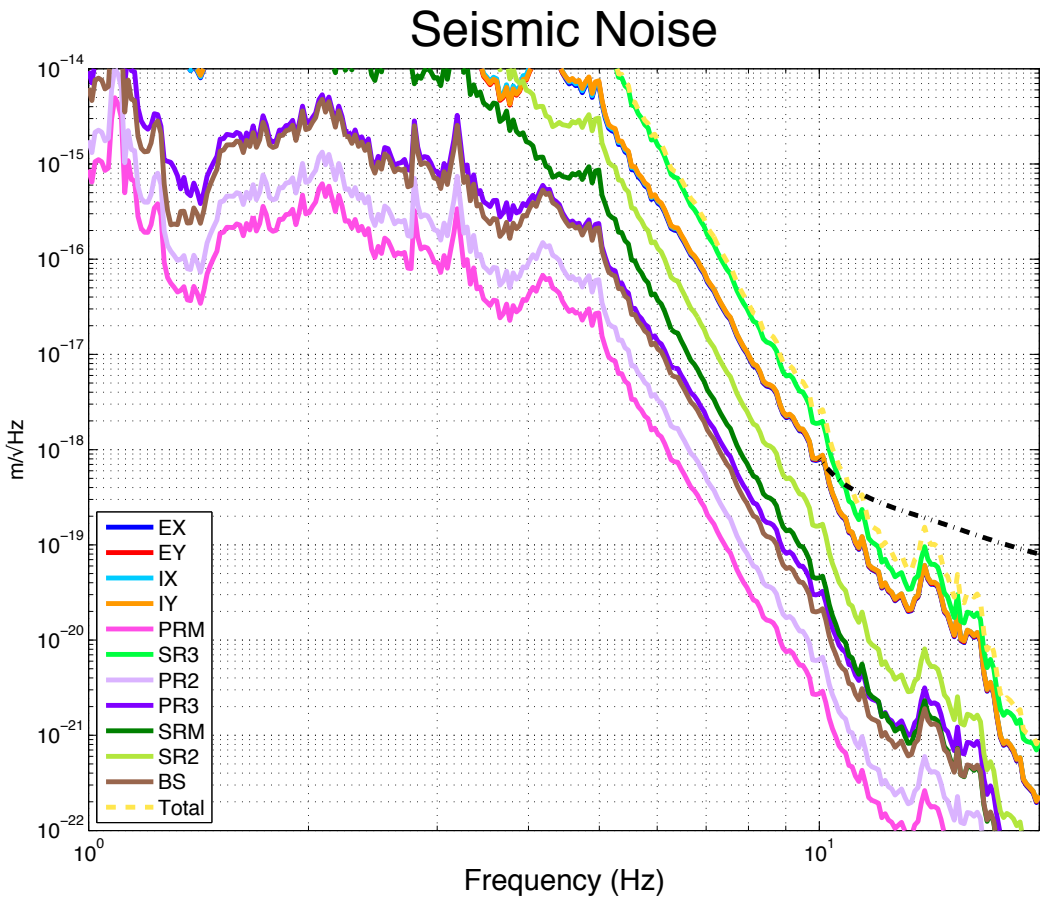

Figure 17: Contribution of the different optics to the seismic noise in ACQUISITION MODE.

7.2 Science Mode

Once the IFO is globally aligned in acquisition mode, a precise measurement of the input matrix can be done. The big off-diagonal terms of the sensing matrix have been included here (units are **W/mRad**):

Signal/DOF	*CS*	*CH*	*DS*	*DH*	*PRM*	*PR3*	*SRM*	*SR3*	*IN1*	*BS*
TR_DC Comm	**-36**	0	0	0	0	0	0	0	0	0
REFL_A I1	−37	**-210**	0	0	0	45	0	0	0	0
TR_DC Diff	0	0	**-36**	0	0	0	0	0	0	0
AS_A Q2	0	0	0	**370**	0	0	0	0	0	0
POP_B DC	0	0	0	0	**-0.7**	0.62	0	0	0	0
POP_A DC	0	0	0	0	0	**1.3**	0	0	0	0
AS_A DC	0	0	0	0	0	0	0.09	0	0	**-7**
REFL_B Q2	−0.64	−0.4	**-1**	0.9	0.36	0.56	0	0.49	−0.37	−0.6
REFL_B I2	0	0	0	0	0.63	**-1.8**	0	0	−0.67	−0.9
AS_B QM	0	0	0	0	0	0	0	0	0	**1.7**

With this gain hierarchy, the input matrix which reconstructs the error signals for the DOFs, in **mrad/W** is the following:

	TR Comm	REF A I1	TR Diff	AS A Q2	POP B DC	POP A DC	AS A DC	REF B Q2	REF B I2	AS B QM
CS	**-0.03**	−0	0	0	0	0	0	0	0	0
CH	0.005	−0.005	0	0	0	**0.17**	0	0	0	0
DS	0	0	**-0.03**	0	0	0	0	0	0	0
DH	0	0	0	**0.003**	0	0	0	0	0	0
PRM	0	0	0	0	**-1.41**	**0.70**	0	0	0	0
PR3	0	0	0	0	0	**0.79**	0	0	0	0
SRM	0	0	0	0	0	0	**10.81**	−0	0	**45.32**
SR3	−0.03	−0.004	−0.06	−0.005	0.06	**-2.41**	0	**2.05**	**-1.11**	0.14
IN1	0	0	0	0	**-1.32**	**-1.48**	0	0	**-1.48**	**-0.80**
BS	0	0	0	0	0	0	0	0	0	**0.60**

(7.2)

With respect to the acquisition mode control filters, more aggressive cut-offs have been designed for science mode. Moreover, the low frequency gain have been increased in the arm cavity loops and in the SR3 loop, whose motion was dominating the seismic noise coupled to DARM. Note that the input matrix reported here contains also the reconstructed SRM degree of freedom, while the SRM is not actually globally controlled.

Figure 19 shows how the decoupling between the DOFs is now very good, as the off-diagonal terms of the open loop transfer functions are small [6].

The equivalent angular noise for each DOF due to shot noise is shown in Table 17.

[6] For details about the meaning of the plot cfr 7.1.

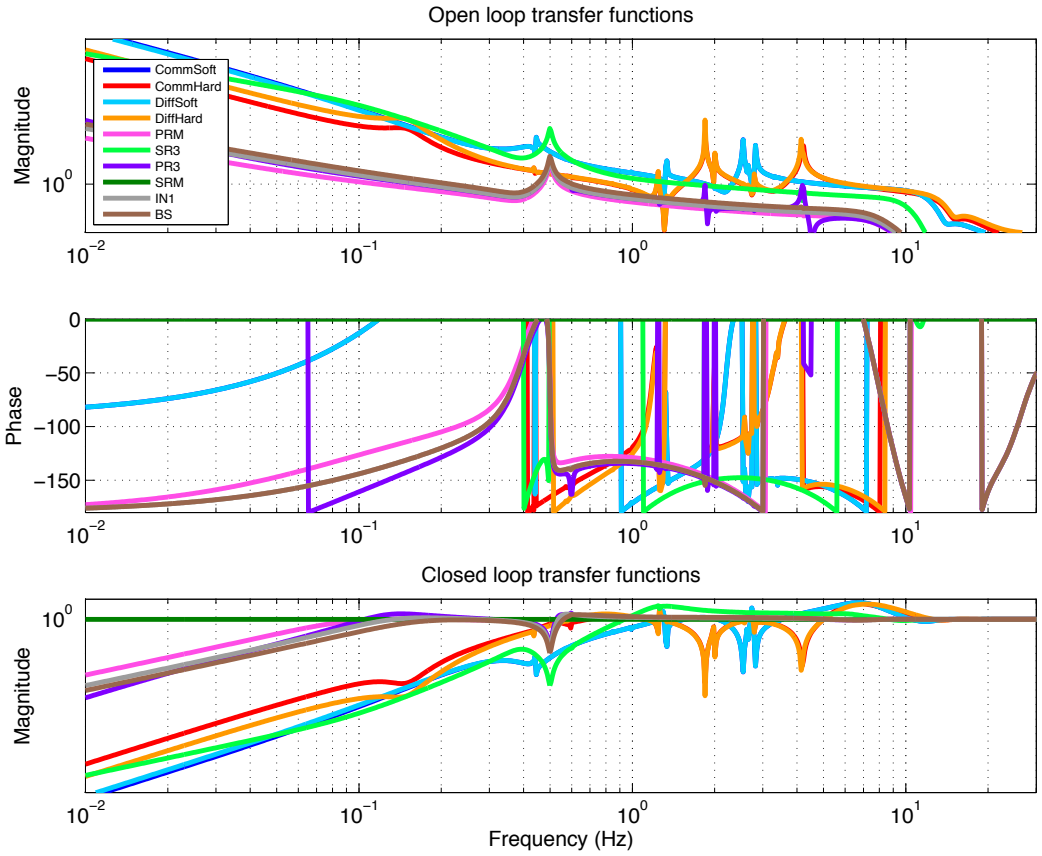

Figure 18: Open loop and closed loop transfer functions of the angular DOF loops in SCIENCE MODE.

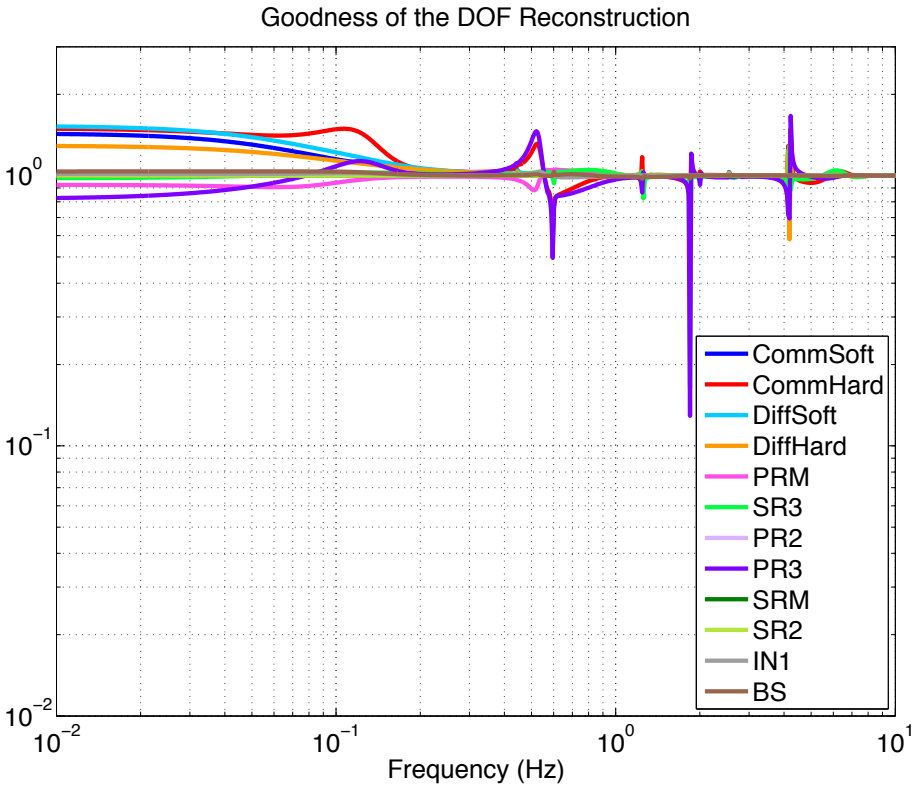

Figure 19: Measurement of the goodness of the reconstruction of the angular DOFs in SCIENCE MODE. The plot shows the ratio between the suppression of the mirror motion expected from the diagonal terms of the open loop transfer function matrix with the one computed by taking correctly into account the not diagonal terms (cfr figure 13 where the same plot for acquisition mode is reported). The reconstruction is optimal when the ratio is 1.

Units/ DOFs	CS	CH	DS	DH	PRM	SR3	PR3	SRM	IN	BS
$(10^{-15} rad/\sqrt{Hz})$	3.7	23	3.7	0.08	215	457	108	2134	339	18

Table 17: Equivalent angle noise due to shot noise for each DOF. Units are $10^{-15} rad/\sqrt{Hz}$. These values have been obtained by propagating the shot noise for each sensor through the input matrix 7.2, and taking the incoherent sum of all the contributions for each DOF.

7.2.1 ASC FOMs: aLIGO maximum power, science mode

The same analysis performed for the acquisition mode is repeated here for science mode. The following figures show:

- the residual pitch motion of each optic 20;
- the BSM on all the optics 21 22;
- the angular noise coupling to DARM 24;
- the contribution of all the optics to the angular seismic noise coupled to DARM 25;
- the beam angular motion on the SRC mirrors 23.

The target for the ASC noise in science mode is shown by the red dotted curve in figure 24, which is a factor 10 below the designed sensitivity. This goal is not achieved below 13 Hz (even if the angular noise is still below the designed sensitivity), but it is pretty close to the target above that frequency.

7.2.2 Note on the SRM alignment loop

The FOMs presented in the previous sections are made with no global alignment control for the SRM. The reason for that is that the reconstruction of the SRM dof is not very good, and keeping the SRM loop closed actually increases the residual motion of the mirror at low frequency. In particular, with a drift control on the SRM mirror of about 100 mHz, we see that the low frequency part of the residual motion is dominated by the BS motion. On the other hand, it seems unwise not to foresee at least a drift control for the SRM, even if it doesn't seem strictly necessary for reducing the noise coupling to DARM. In particular, we might need to reduce the beam spot motion and the angular motion of the beam entering the OMC. The following plots show an alternative control scheme in which the BS is controlled with high bandwidth (few Hz), and the SRM is under drift control (see figure 26). The increase bandwidth on the BS reduces the BSM (figure 29) and the BAM (figure **??**) of the beam on the SRM by about a factor 2.

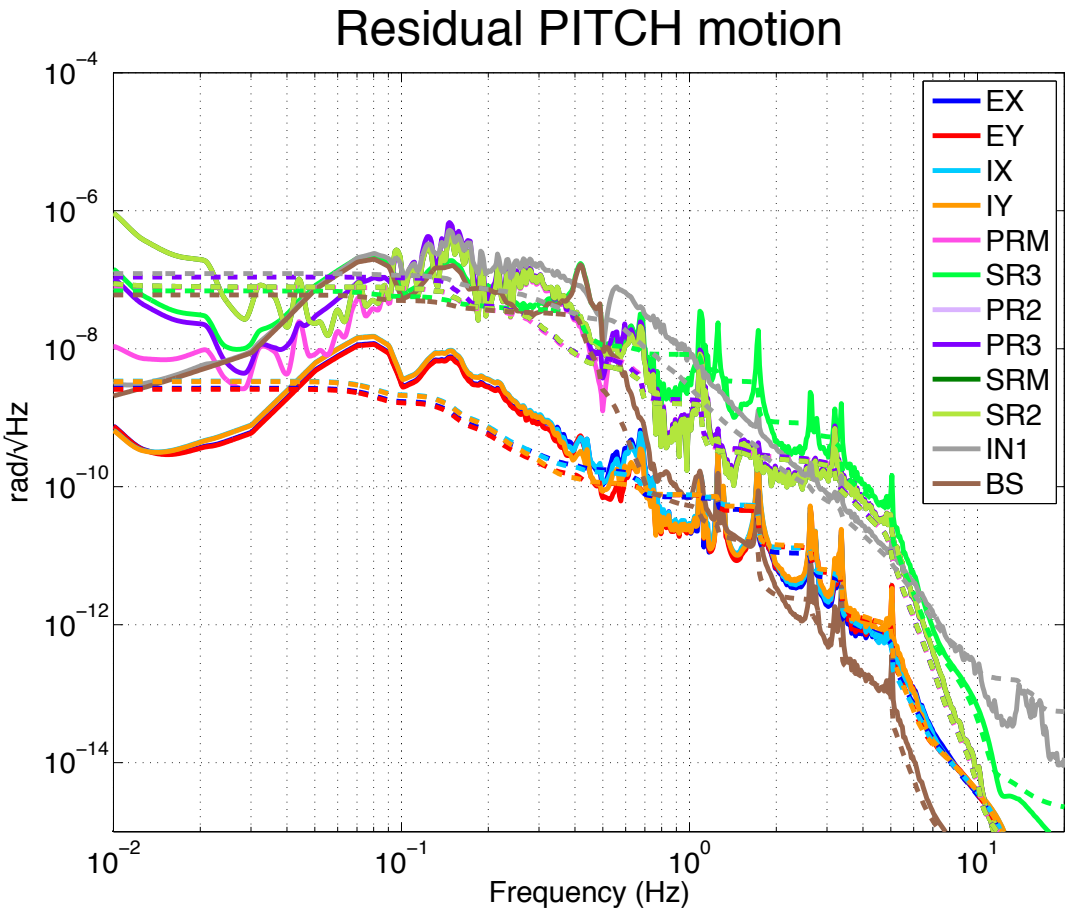

Figure 20: Residual pitch motion in SCIENCE MODE.

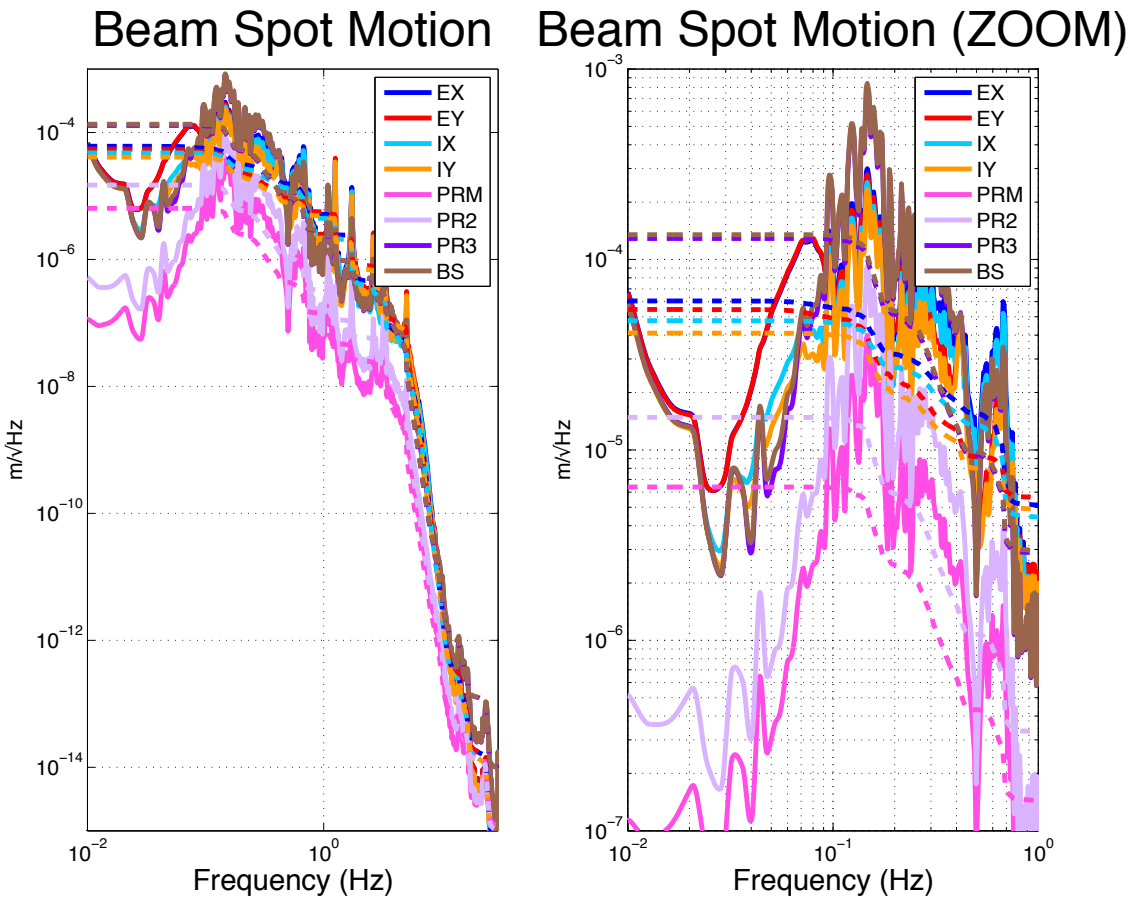

Figure 21: Beam Spot Motion (BSM) in SCIENCE MODE.

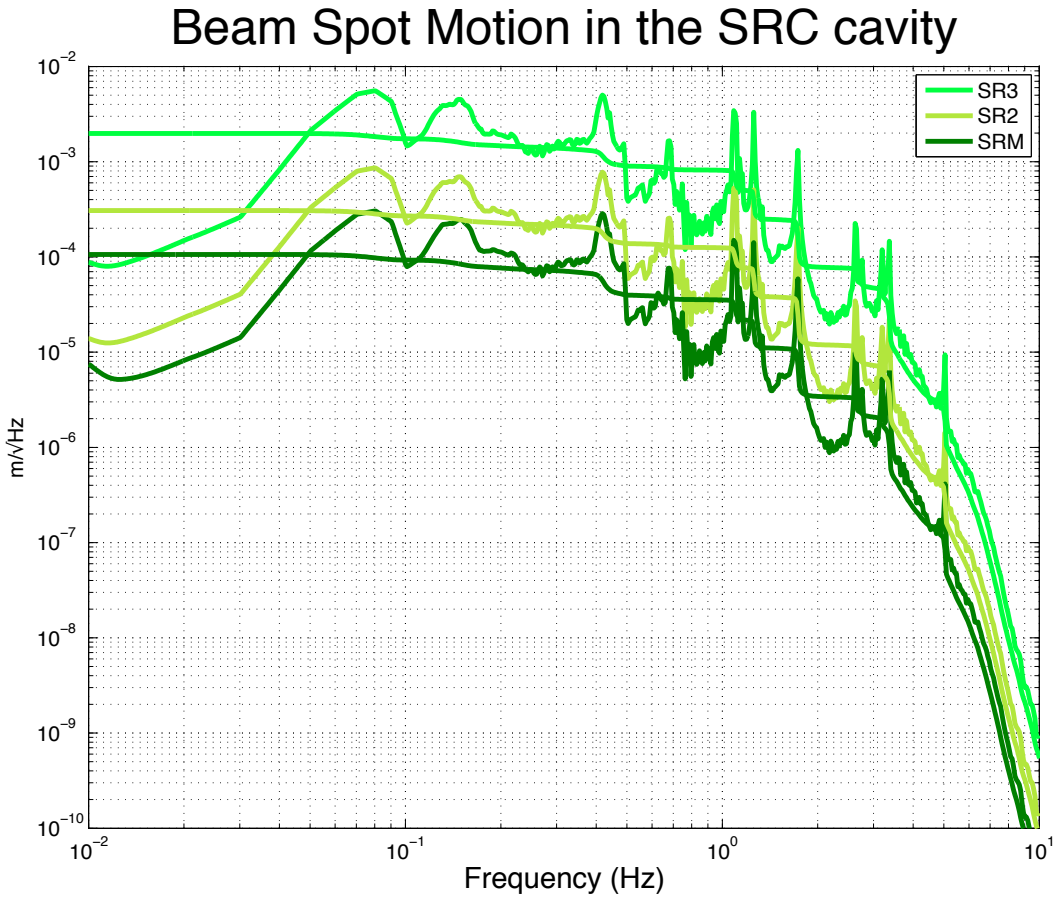

Figure 22: Beam Spot Motion (BSM) on the SRC mirrors in SCIENCE MODE. This is the effective beam spot motion on the optics. The BSM used for computing the coupling to DARM is actually computed as described in section 5.4, with $\mathcal{C} = A_{00BS}/A_{00SRM} \sim 0.01$.

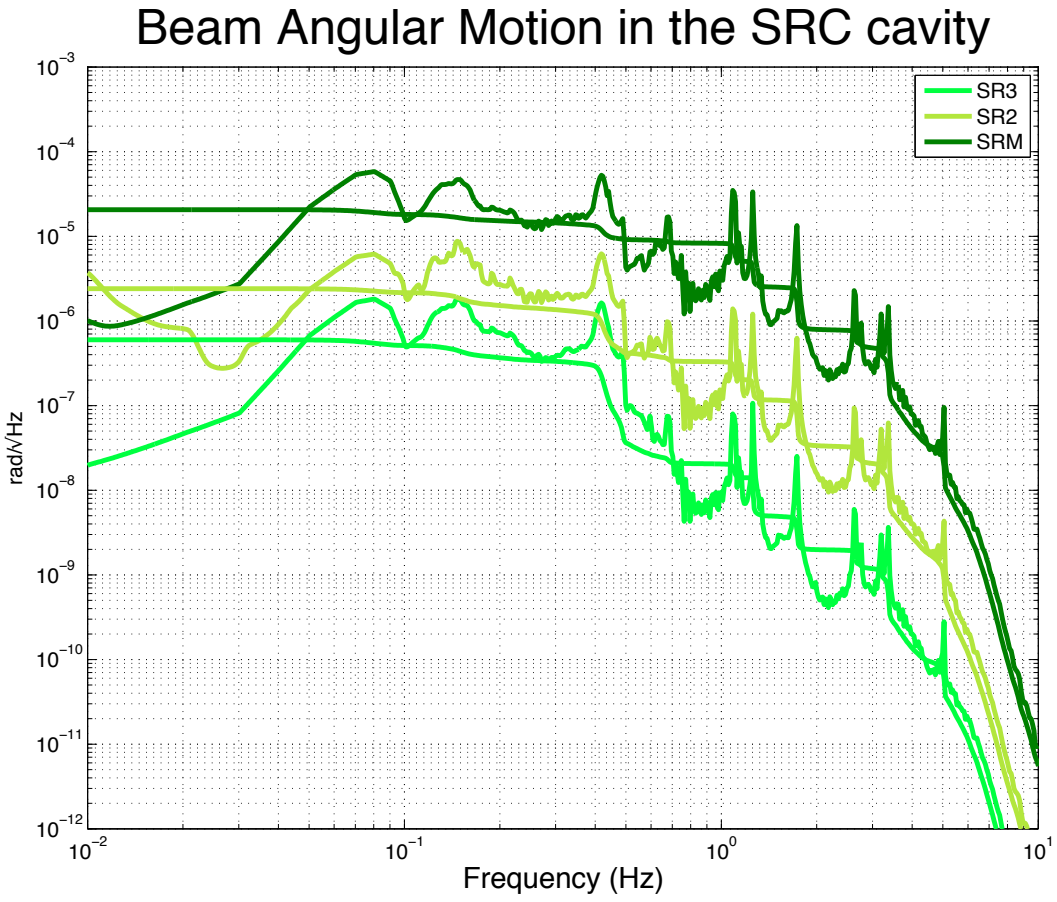

Figure 23: Beam Angular Motion (BAM) on the SRC mirrors in SCIENCE MODE.

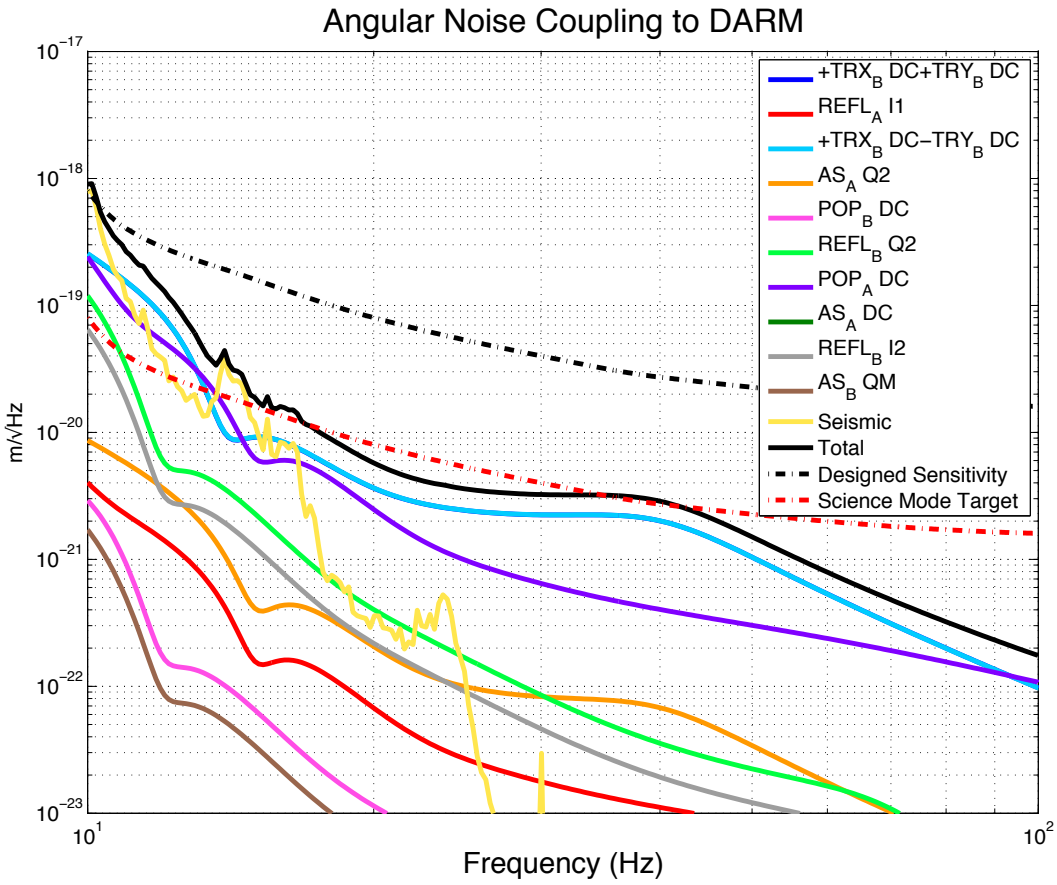

Figure 24: Angular noise coupling to DARM in SCIENCE MODE. The yellow curve represents the sum of the seismic noise contribution from all the mirrors (see figure 25). for details.

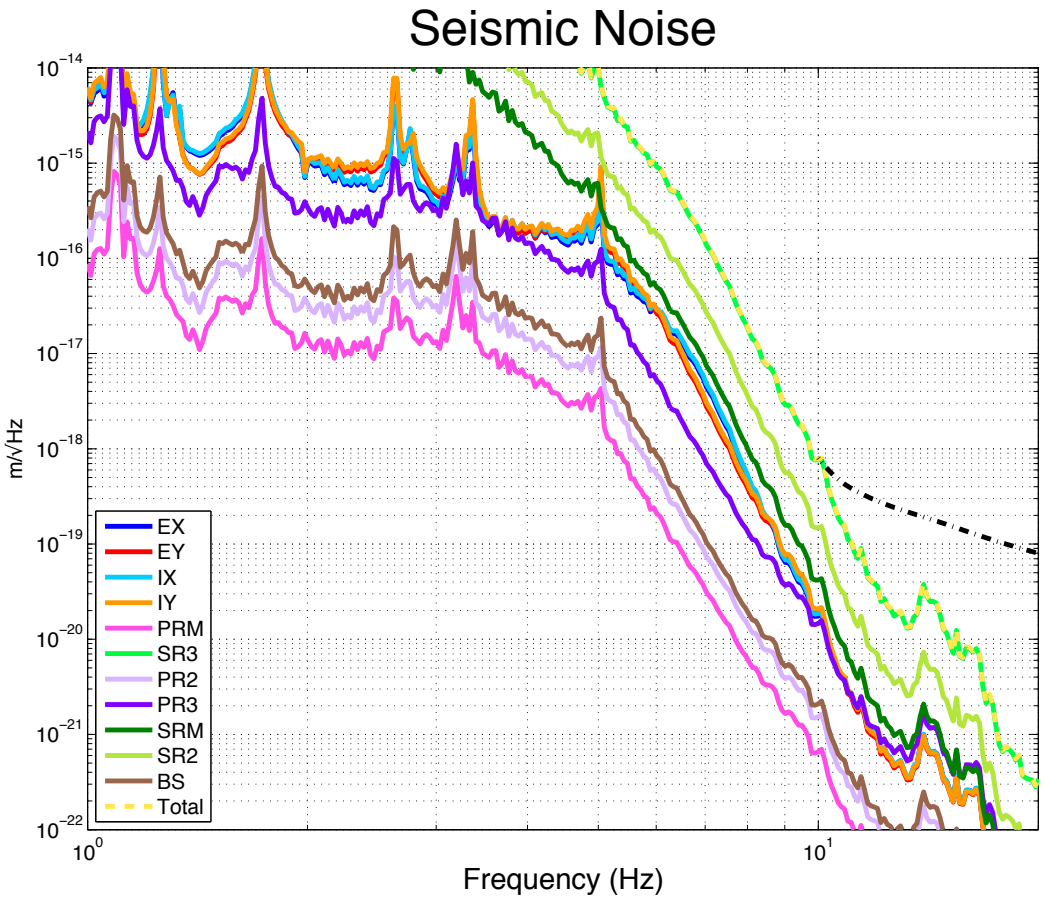

Figure 25: Contribution of the different optics to the seismic noise in SCIENCE MODE.

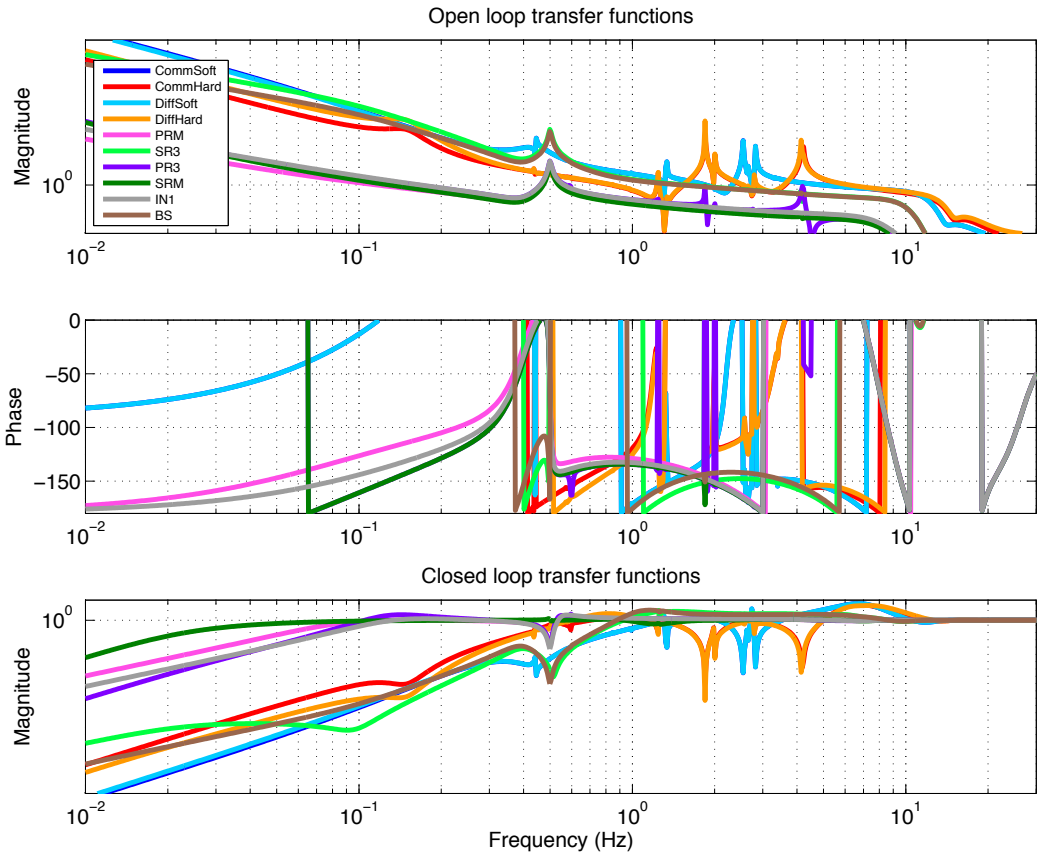

Figure 26: Open loop transfer functions of the angular control loops in SCIENCE MODE, with high bandwidth control for the BS and drift control for the SRM.

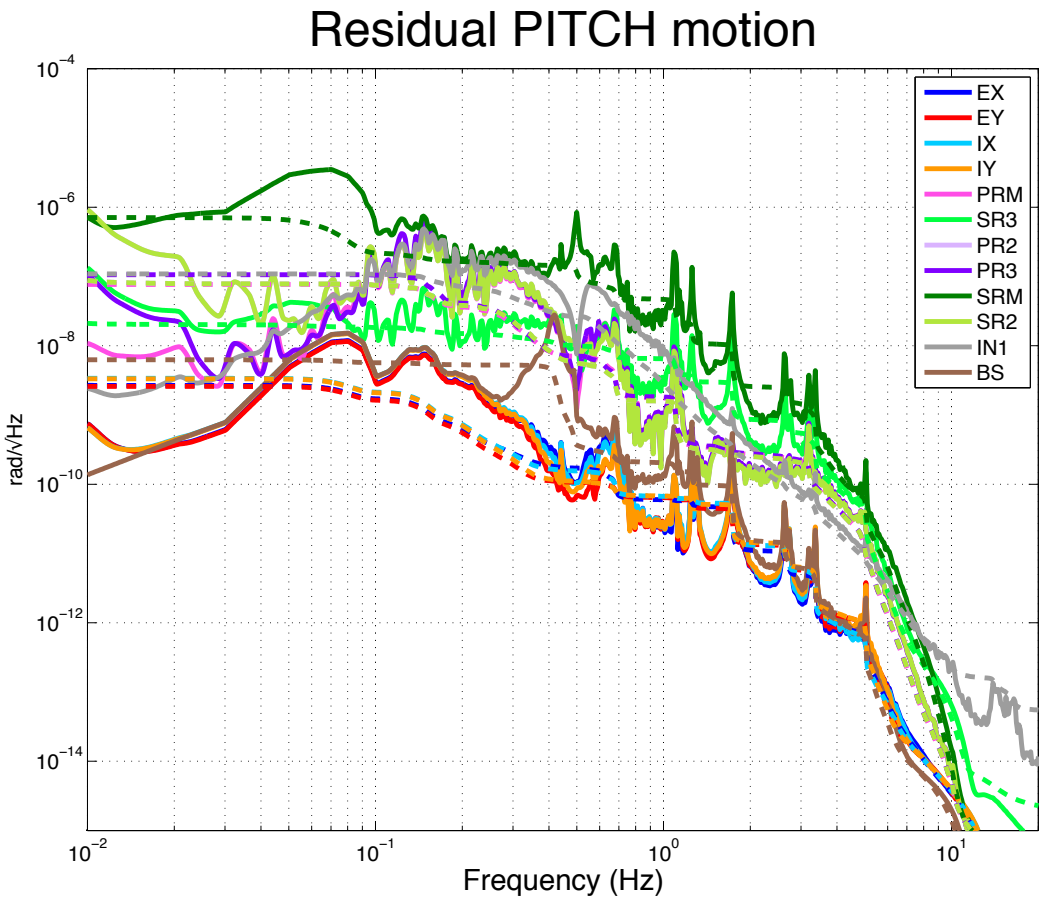

Figure 27: Residual angular motion in SCIENCE MODE with high bandwidth control for the BS and drift control for the SRM.

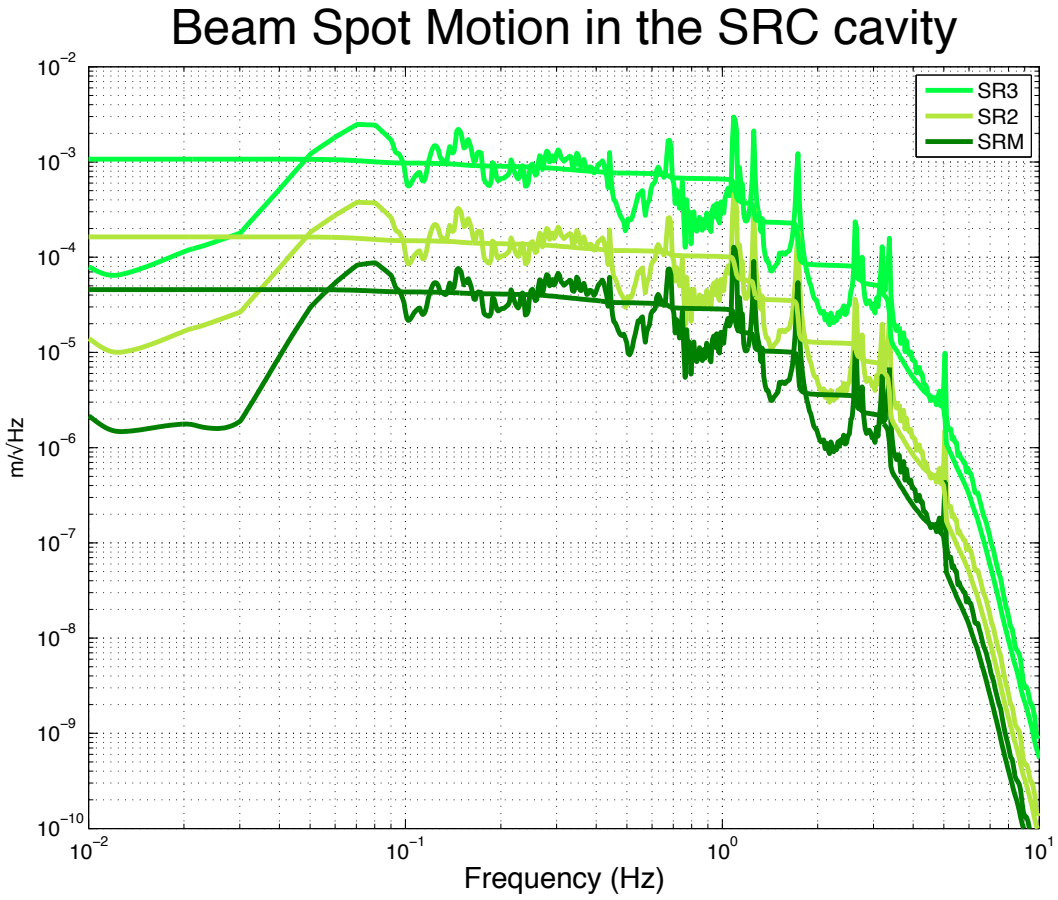

Figure 28: Beam spot motion on the SRC optics in SCIENCE MODE with high bandwidth control for the BS and drift control for the SRM (compare this plot with figure **??**).

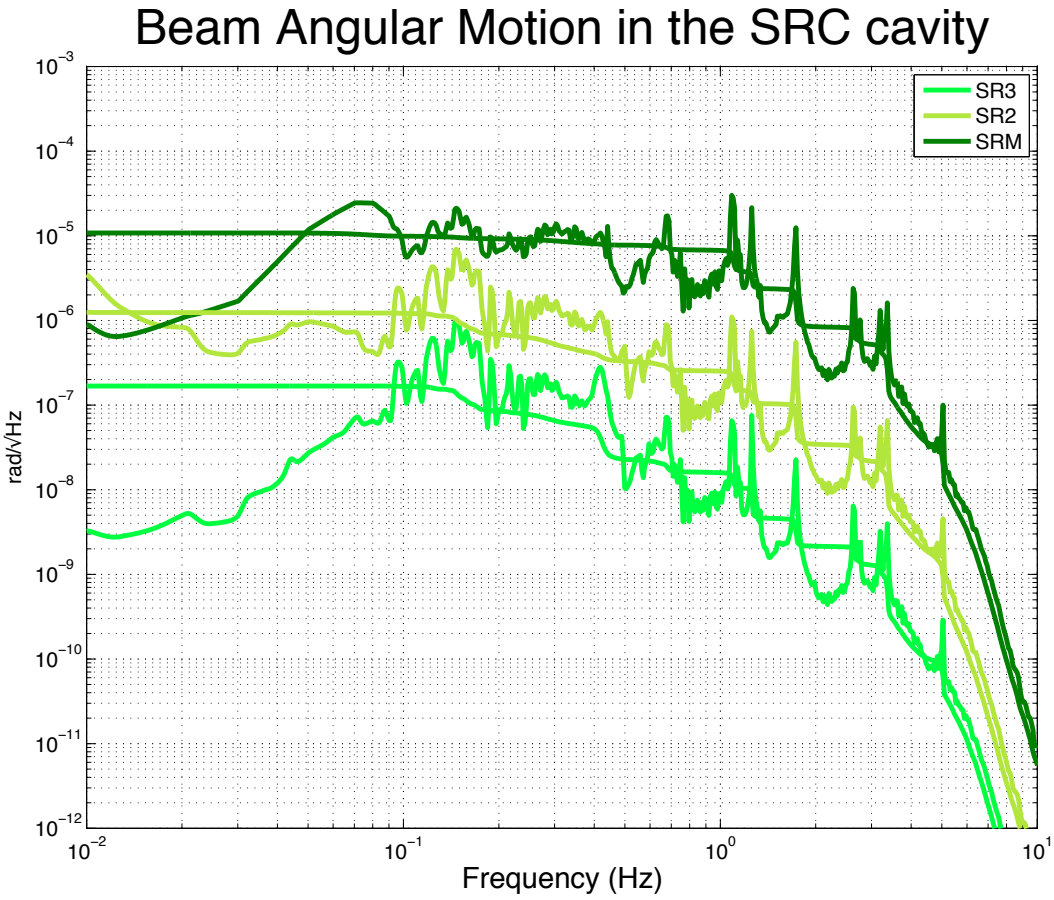

Figure 29: Beam angular motion on the SRC optics in SCIENCE MODE with high bandwidth control for the BS and drift control for the SRM (compare this plot with figure 23).

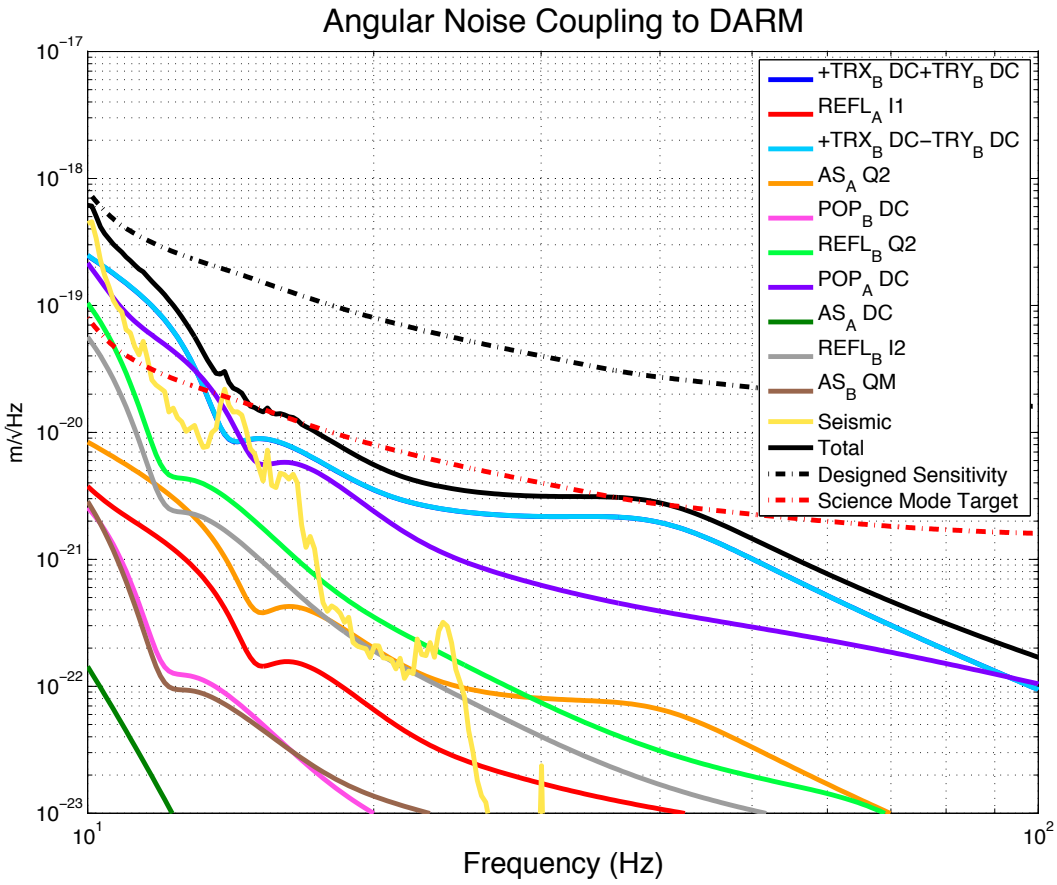

Figure 30: Angular noise coupling to DARM in SCIENCE MODE with high bandwidth control for the BS and drift control for the SRM. The yellow curve represents the sum of the seismic noise contribution from all the mirrors.

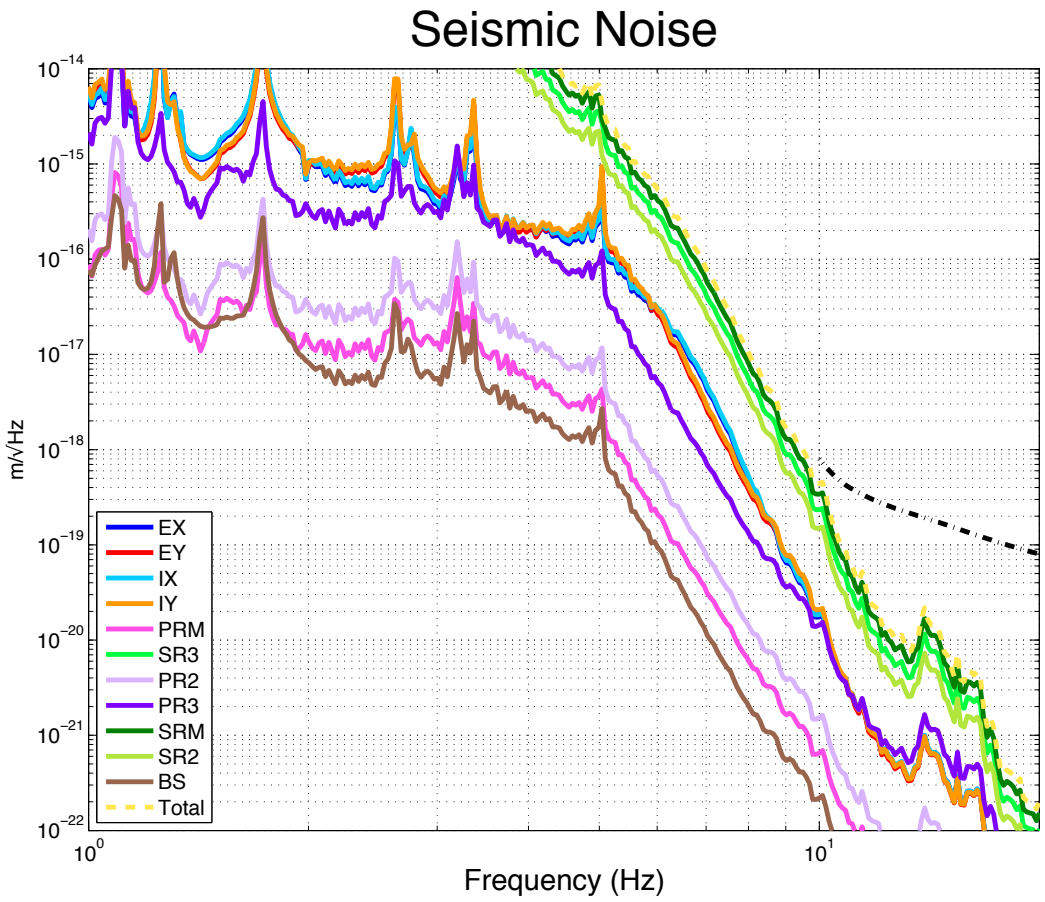

Figure 31: Seismic noise contribution to DARM in SCIENCE MODE with high bandwidth control for the BS and drift control for the SRM.

8 aLIGO with 25 W input power

Before running at full power, aLIGO will operate in a "low power mode", with 25 Watt of input power. With respect to the full power science mode configuration, there are two main differences:

- the opto-mechanical transfer functions are different (see also section 3);
- the power at the AS port is 5 times lower.

Because of the complexity of the transfer functions of the aLIGO quadruple pendulum, the control filters need to be slightly adjusted to keep the loops stable but they are pretty similar to the one shown in the previous section.

Since the signals at the AS port used in the ASC scheme have very low coupling to DARM, the noise performance is very similar to what shown in figure 24.

The usual list of FOMs is the following:

- the residual motion 32;
- the beam spot motion 33 35;
- the angular noise coupling to DARM 37
- the contribution of each optics to the angular seismic noise 38;
- the beam angular motion on the SRC mirrors 34;

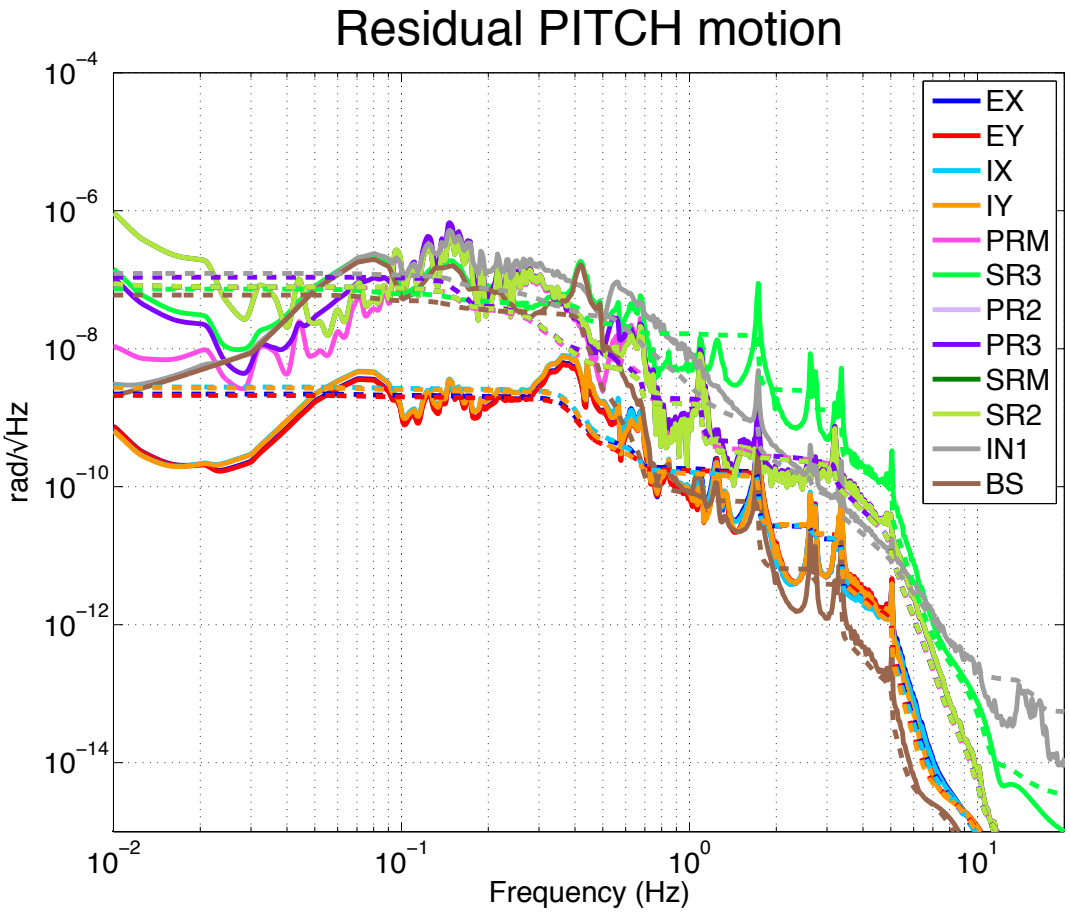

Figure 32: Residual pitch motion in aLIGO with 25 W.

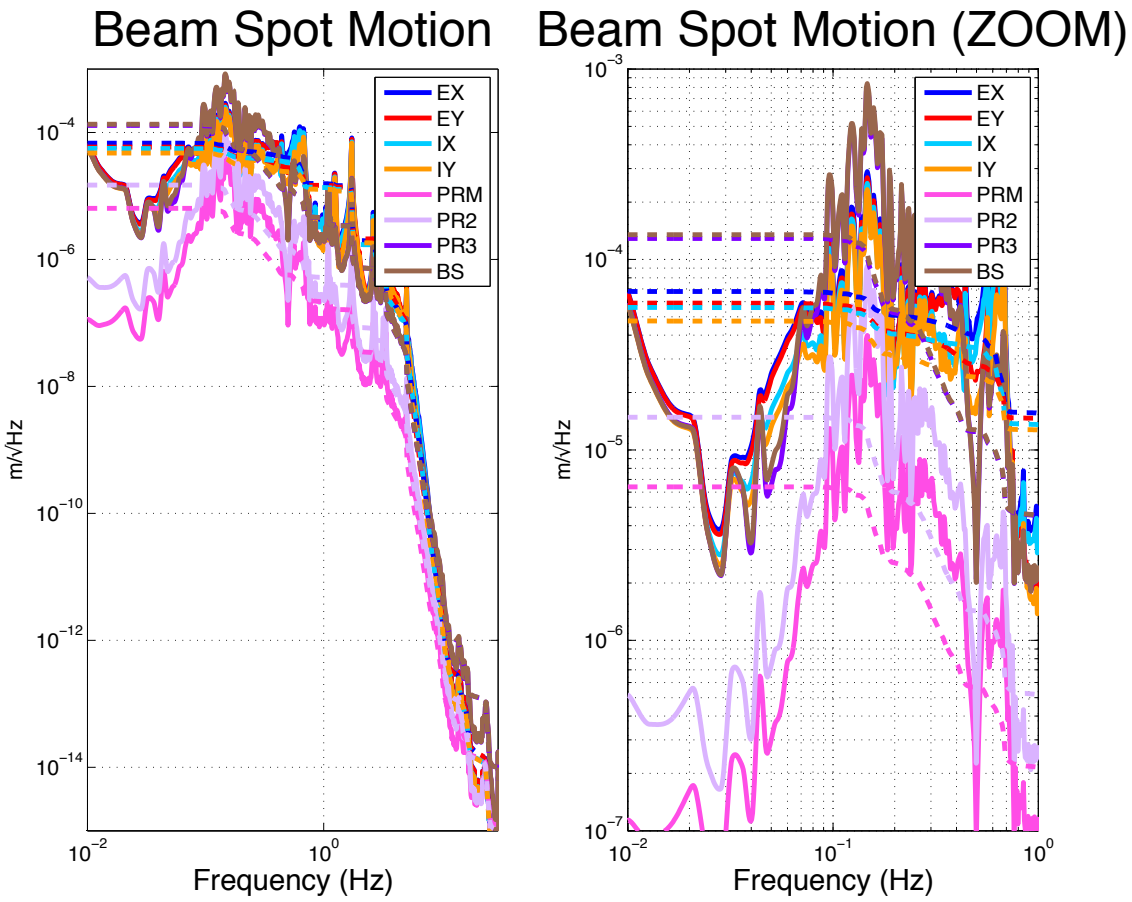

Figure 33: Beam Spot Motion (BSM) on each optic in aLIGO with 25 W.

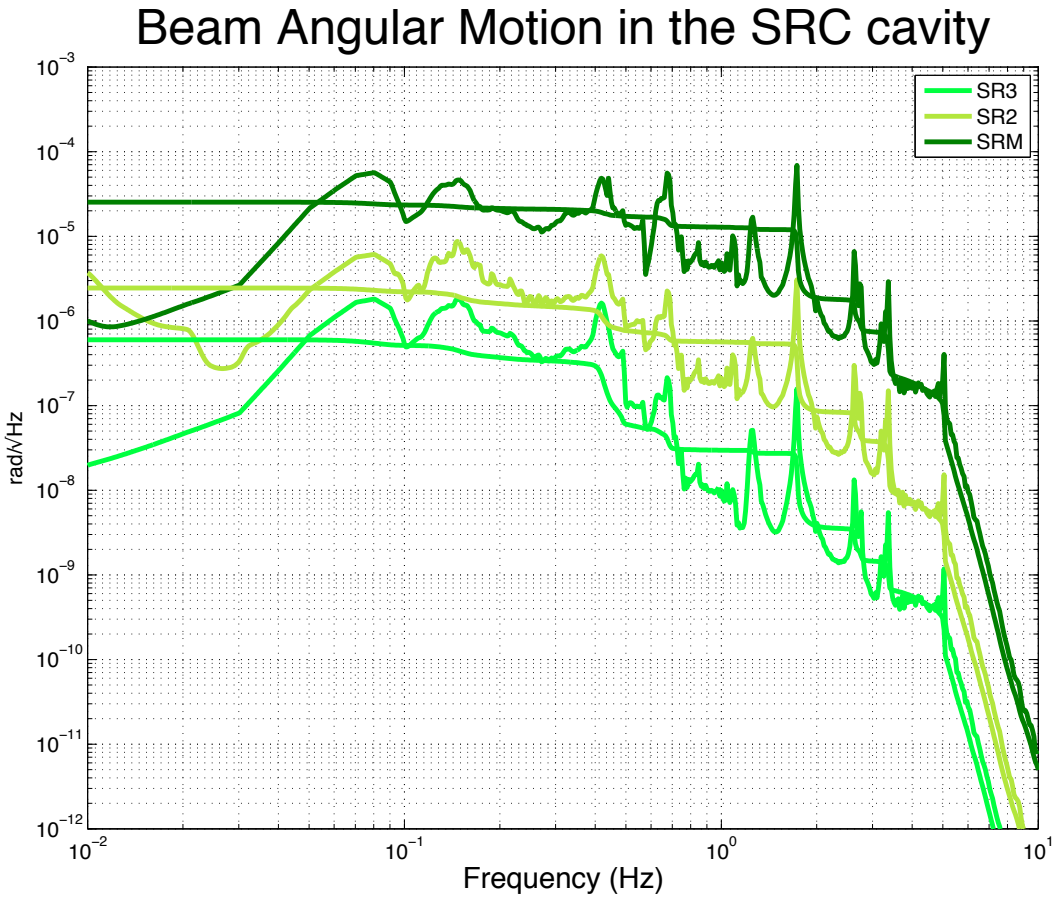

Figure 34: Beam Angular Motion (BAM) on the SRC mirrors in aLIGO with 25 W.

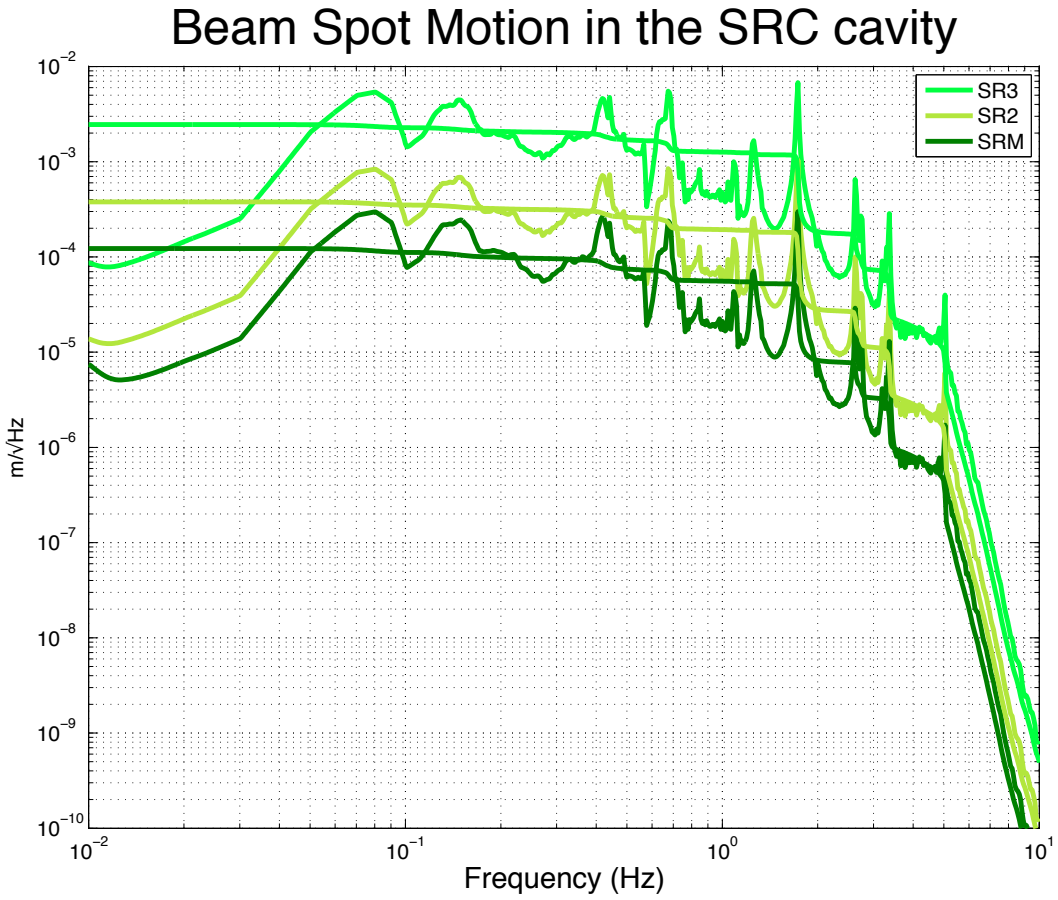

Figure 35: Beam Spot Motion (BSM) on the SRC mirrors in aLIGO with 25 W. This is the effective beam spot motion on the optics. The BSM used for computing the coupling to DARM is actually computed as described in section 5.4, with $\mathcal{C} = A_{00BS}/A_{00SRM} \sim 0.01$.

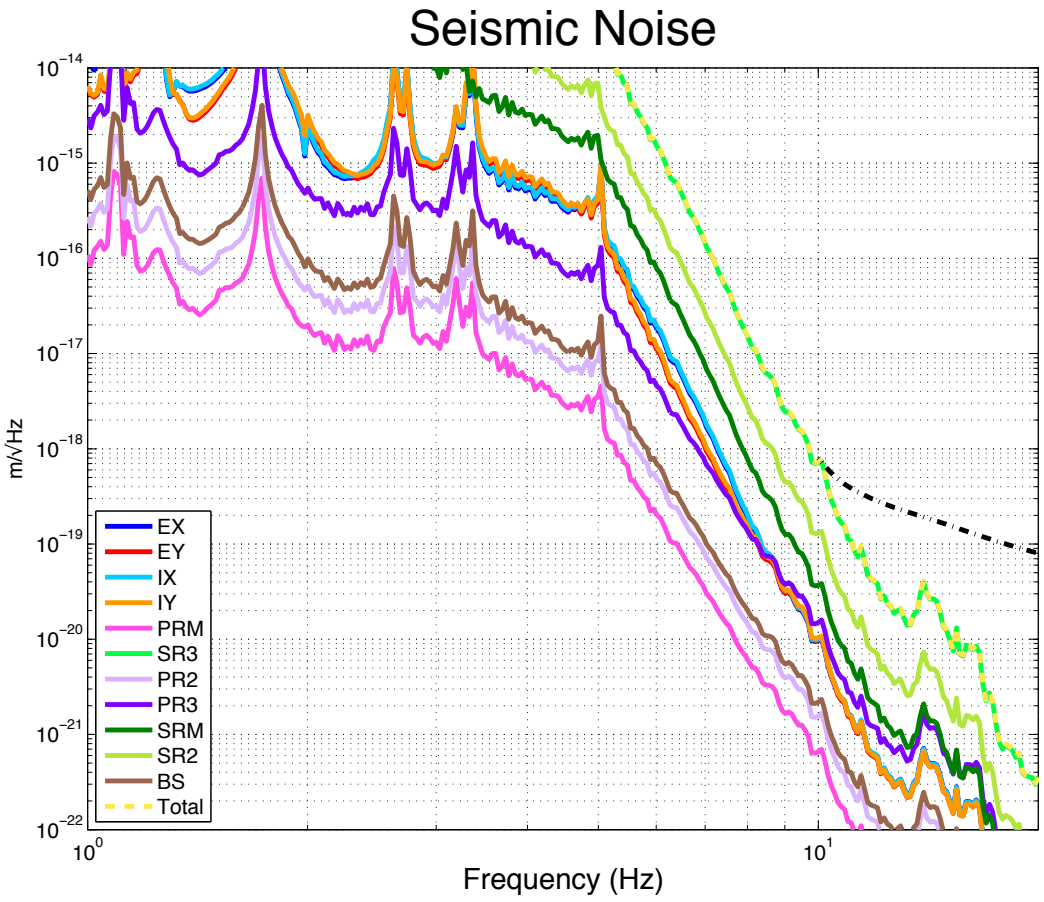

Figure 36: Contribution of the different optics to the seismic noise in aLIGO with 25 W.

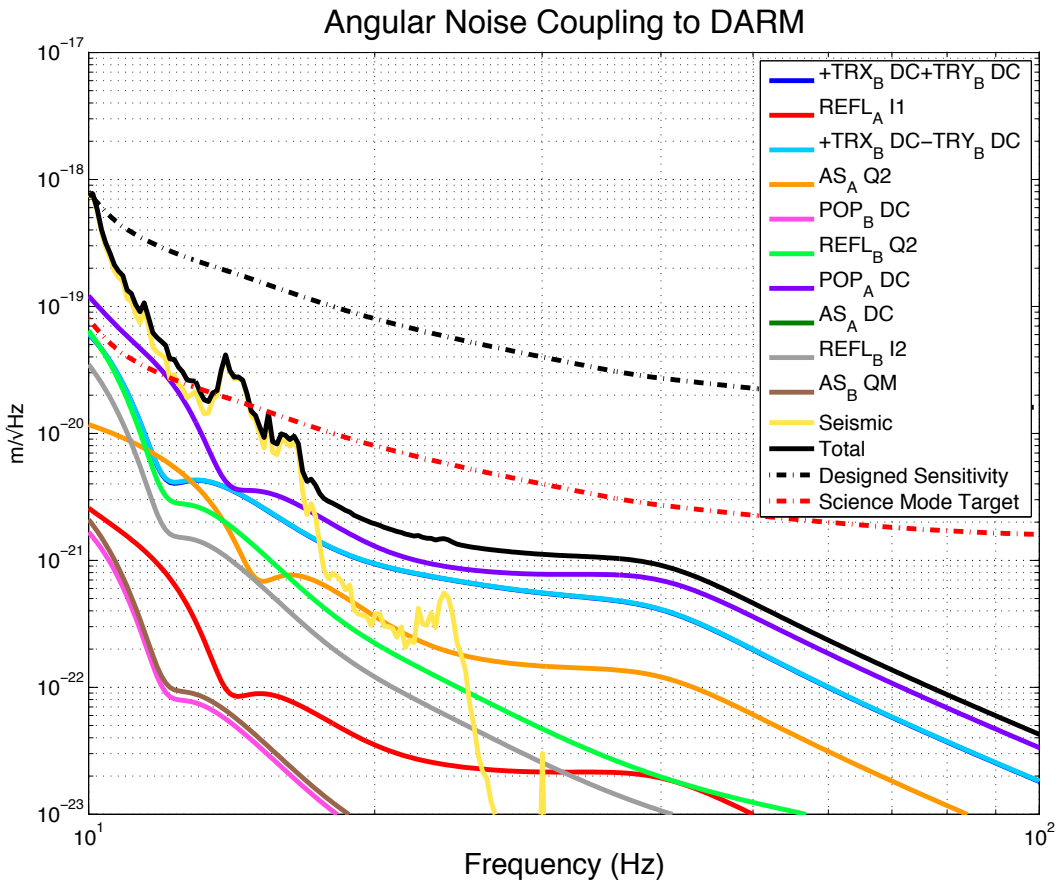

Figure 37: Angular noise coupling to DARM with aLIGO with 25 W. The yellow curve represents the sum of the seismic noise contribution from all the mirrors (see figure 38 for details).

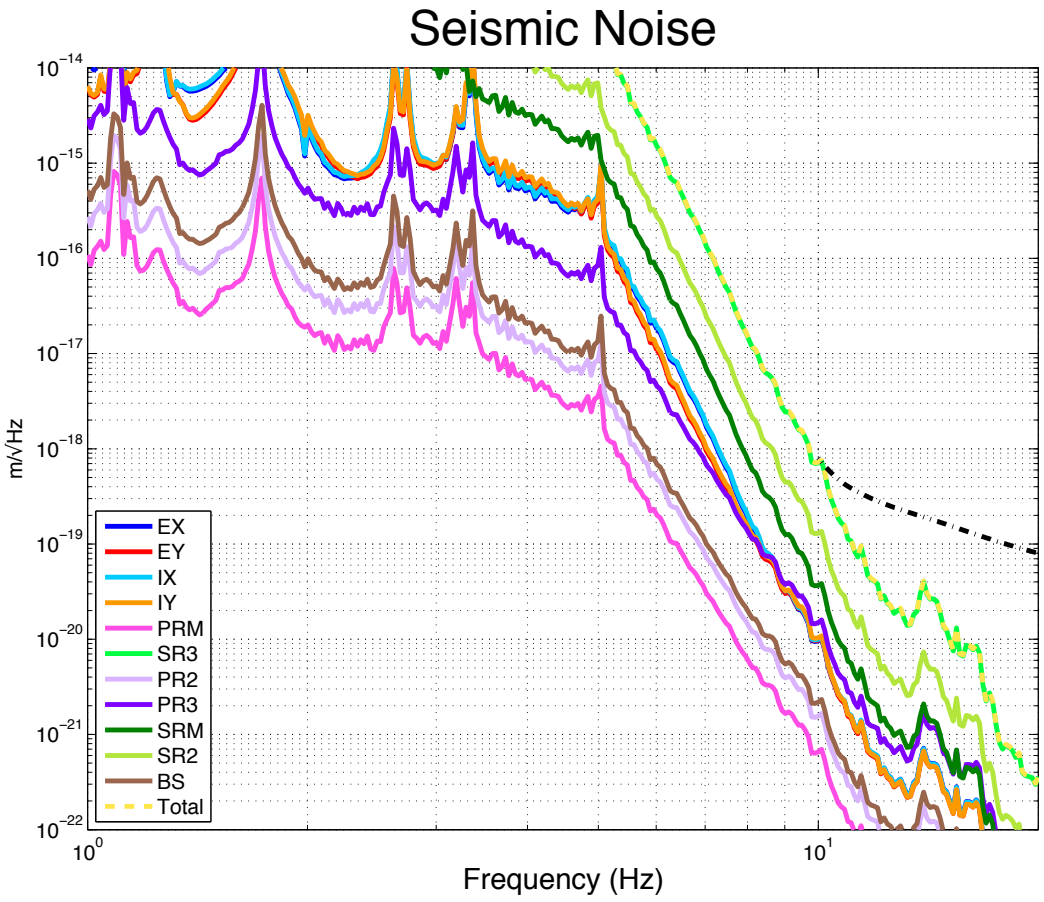

Figure 38: Contribution of the different optics to the seismic noise in aLIGO with 25 W.

9 iLIGO-like configuration (no SRM), with 25 W input power

In the first part of the commissioning, aLIGO is likely to be operated with a high transmission of the signal recycling mirror. A possible alignment scheme for this configuration is described in this section. An input power of 25 W is considered and a transmission of $T = 1$ is set for the SRM. The additional mirrors of the signal recycling cavity, SR2 and SR3, are also present.

9.1 Sensing and Control Scheme

The sensing scheme for this configuration is described in the following table (units are **W/mRad**). The SR3 mirror is controlled by a DC signal, AS_B DC, with a low bandwidth loop. The sensing scheme for the other DOFs is similar to the one described above. As before, the following matrix relies on gain hierarchy.

Signal/DOF	*CS*	*CH*	*DS*	*DH*	*PRM*	*PR3*	*SR3*	*IN1*	*BS*
TR_DC Comm	**-36.0**	0	0	0	0	0	0	0	0
REFL_A I1	36.7	**210.1**	0	0	0	−43.7	0	0	0
TR_DC Diff	0	0	**-36.0**	0	0	0	0	0	0
AS_A Q2	0	0	0	**-332.7**	0	0	0	0	0
POP_B DC	0	0	0	0	−0.7	0.8	0	0	0
POP_A DC	0	0	0	0	0.3	**-1.7**	0	0	**-0.7**
AS_A DC	0	0	0	0	0	0	**-5.0**	0	**3.4**
REFL_B Q2	0	0	0	0	**-1.0**	**4.8**	0	**1.1**	**1.7**
AS_B DC	0	0	0	0	0.0	0	**-4.7**	0	**3.6**

Gouy phases have been set as shown in the next table. There are only 20 degrees of difference in the Gouy phases of the sensors at the AS port, which is far from optimal.

Port	*Sensor*	*GouyPhase(dg)*	*Tuning*	*A∠B(dg)*
TRX, TRY	*A*	14	*Max DH*	90
	B	−76	*Min DH*	
AS	*A*	−78	*Max SRM*	20
	B	−58	*Max BS*	
REFL	*A*	−33	*Max CH*	90
	B	+57	*Min CH*	
POP	*A*	−39	*Max PRM*	118
	B	78.7	*Max PR3*	

(9.1)

The open loop and closed loop transfer functions are shon in figures 39.

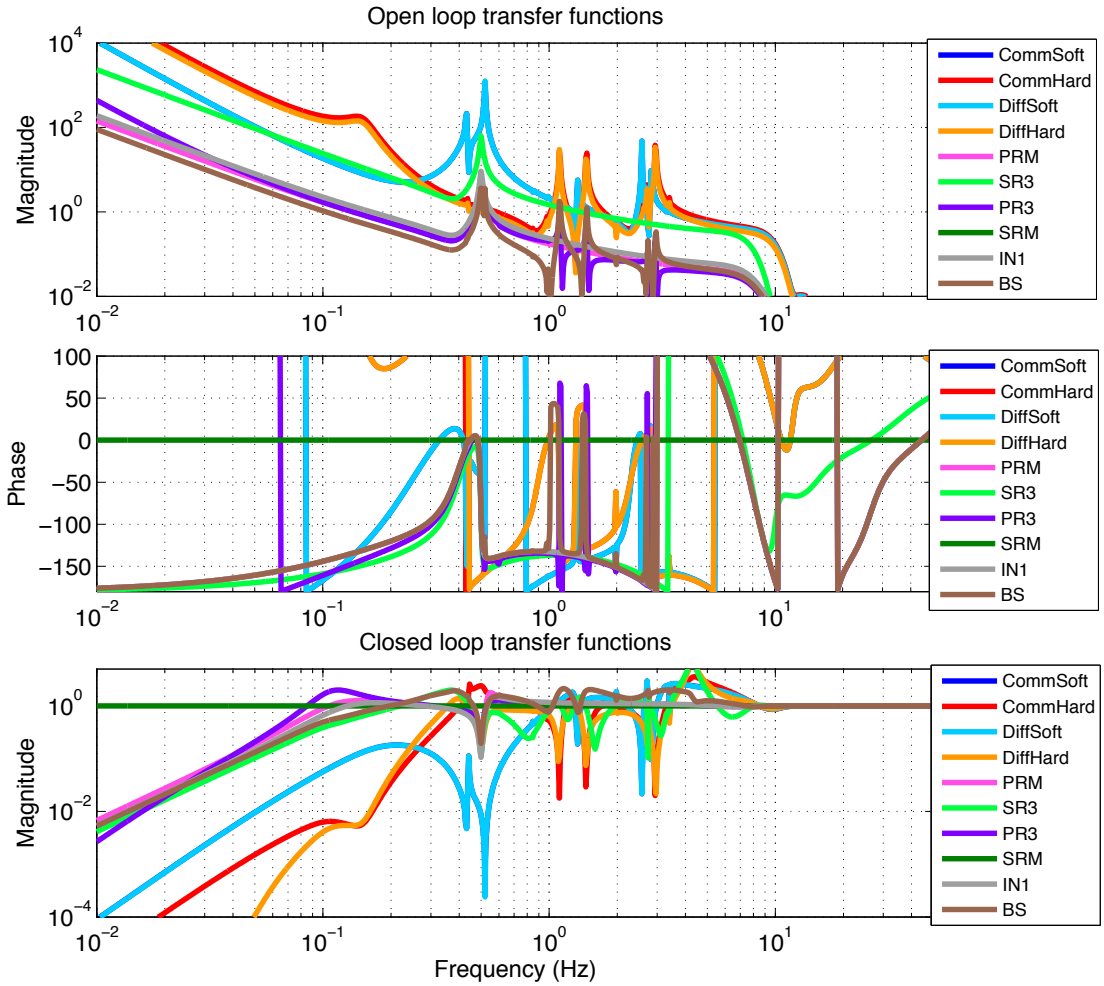

Figure 39: Open loop and closed loop transfer functions of the angular DOF loops in 'iLIGO MODE' The loop on the signal recycling mirror (SRM) is not present.

9.2 ASC FOMs: iLIGO-like configuration with 25 W

Also for this configuration, the usual FOMs are reported:

- the residual motion 40;
- the beam spot motion 41;
- the angular noise coupling to DARM 42

- the contribution of each optics to the angular seismic noise 43.

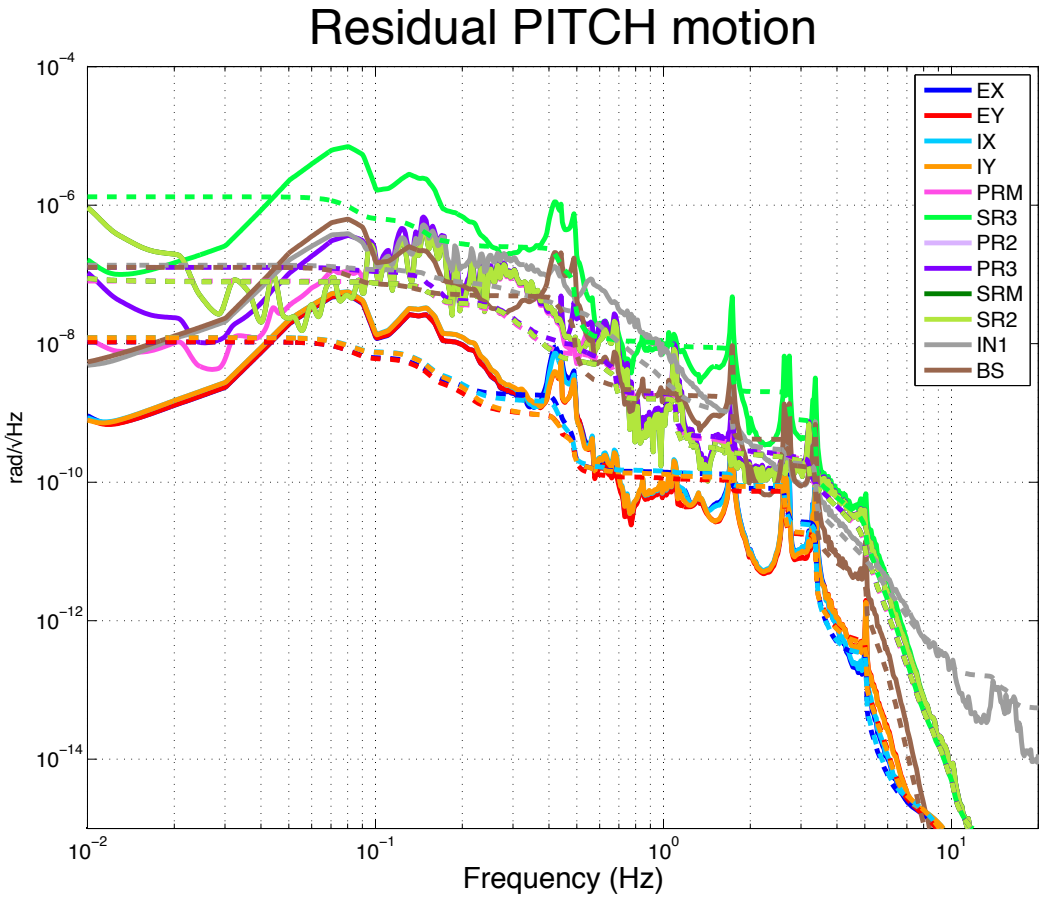

Figure 40: Residual angular motion of each optic in 'iLIGO MODE'.

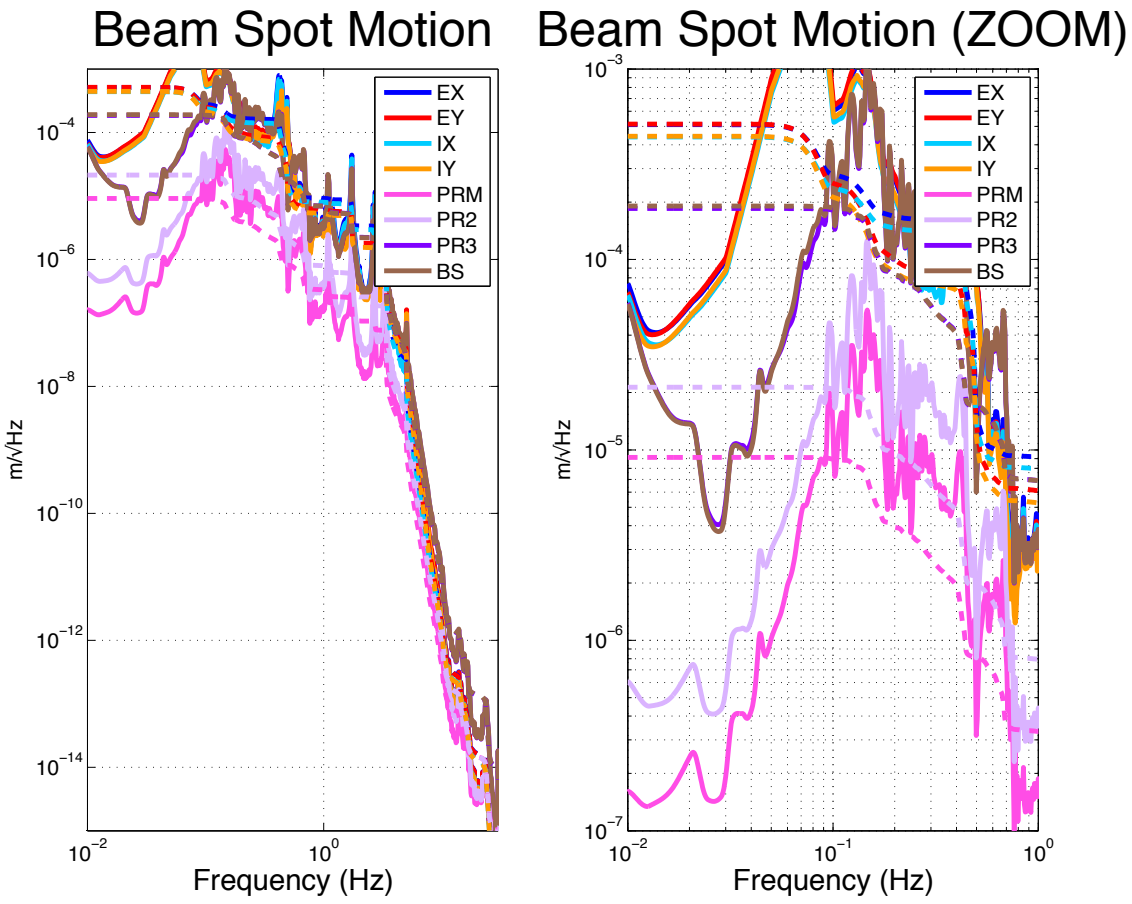

Figure 41: Beam Spot Motion (BSM) on each optic in 'iLIGO MODE'.

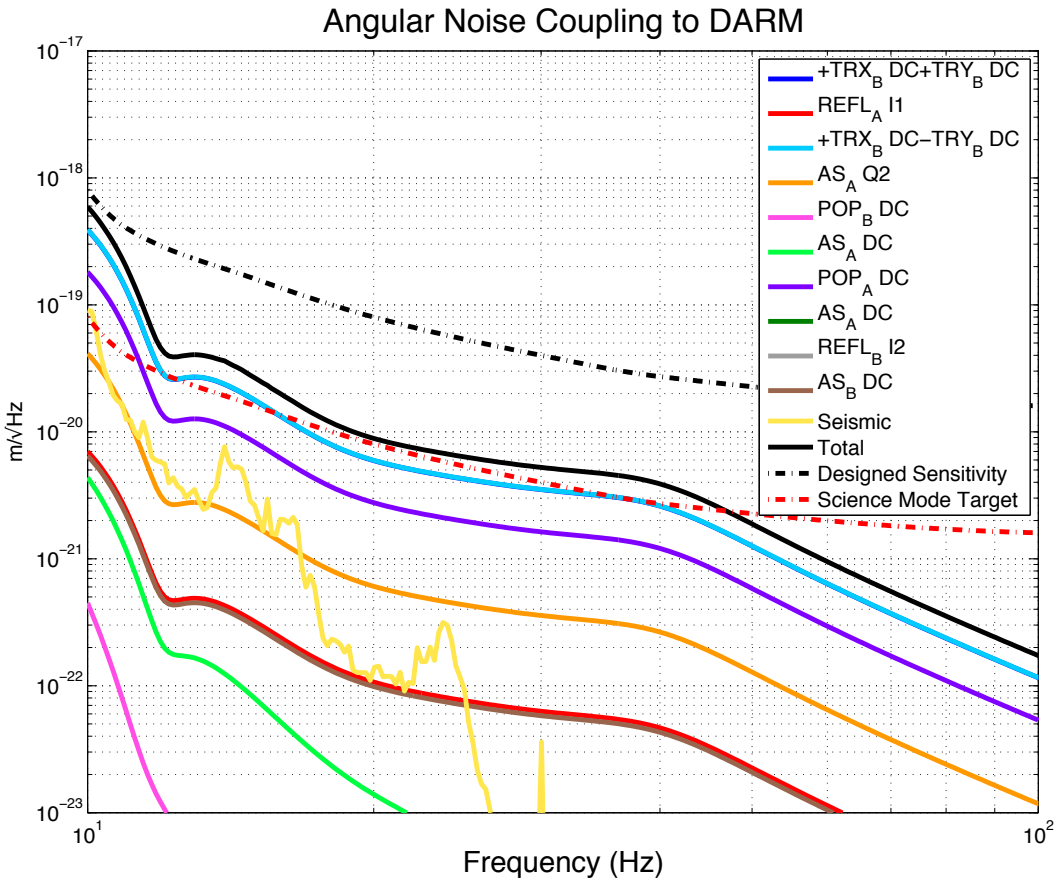

Figure 42: Angular noise coupling to DARM in 'iLIGO MODE'.

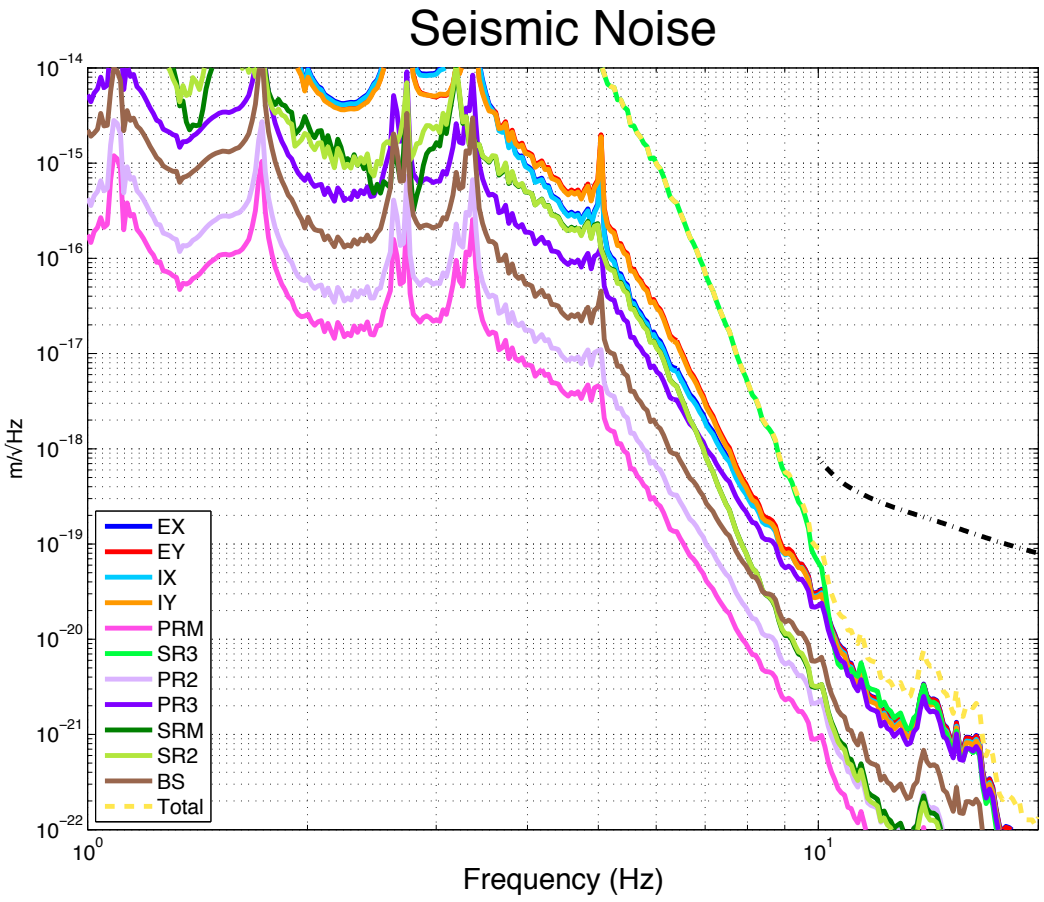

Figure 43: Contribution of the different optics to the seismic noise in 'iLIGO MODE'.

10 Conclusions

The work presented in this note has the final goal of proposing an alignment scheme which meets the stringent noise requirements of aLIGO, and investigate the main complications of the new optical scheme with respect to first generation detectors: higher input power, more mirrors to be controlled, more complex suspension system. There are at least a few outcomes of this work which we think are worth stressing :

- radiation pressure effects appear to be less important than expected: part of this is due to the fact that aLIGO has bee designed to mitigate radiation pressure effects, as compared to eLIGO. Moreover, the larger restoring torque of the quadruple pendulum helps to make radiation pressure effects less critical. The result is that the soft modes remain stable for all but the highest input powers, and even at maximum power the instability is easily overcome by the control system;
- the design of control filters in presence of multiple-resonance transfer functions is not trivial, and it requires particular attention in order to be sure that all the unity gain frequency crossing points are stable. Moreover, the stability must be maintained for different power levels. In this model, we picked two different power levels (25 W and 125 W) and we tuned the control filters for the particular opto-mechanical transfer functions. The more general problem of having control filters which can operate at different power levels has not been addressed here, but it should be done at some point;
- the proposed sensing scheme, in particular the use of the QPDs in transmission to the arm cavities, should provide an easy and robust way of controlling the arm cavity DOFs;
- the proposed control scheme, at least in principle, meets the noise requirements, with an angular control noise a factor 10 below the designed sensitivity.

A DC and RF powers

A.1 Characteristics of the Optickle model

- 50 mW on each WFS (except at the AS port before the OMC: there are 5 mW by taking only 1% of the power and splitting it on 2 diodes, resulting in 2.5 mW power on each WFS);
- the shot noise is estimated as $\sqrt{2h_P\nu_{light}P_{DC}}$ for all signals, where P_{DC} is the total DC power on the WFS.

A.2 Contribution to DC power (in mW) on each sensor from each optical field component (MHz)

	−91	−54.6	−45.5	−36.4	−18.2	−9.1	0.0	9.1	18.2	36.4	45.5	54.6	91	*Total*
$REFL_A$	0	0.01	1.63	0.01	0	5.11	36.11	5.11	0	0.01	1.63	0.01	0	49.65
$REFL_B$	0	0.01	1.63	0.01	0	5.11	36.11	5.11	0	0.01	1.63	0.01	0	49.65
POP_A	0	0	0.18	0	0	0.36	48.66	0.36	0	0	0.18	0	0	49.73
POP_B	0	0	0.18	0	0	0.36	48.66	0.36	0	0	0.18	0	0	49.73
AS_A	0	0	1.02	0	0	0	0.41	0	0	0	1.02	0	0	2.44
AS_B	0	0	1.02	0	0	0	0.41	0	0	0	1.02	0	0	2.44
$OMCr_A$	0	0	24.15	0	0	0.03	0	0.03	0	0	24.15	0	0	48.36
$OMCr_B$	0	0	24.15	0	0	0.03	0	0.03	0	0	24.15	0	0	48.36
TRX_A	0	0	0	0	0	0	48.62	0	0	0	0	0	0	48.62
TRX_B	0	0	0	0	0	0	48.62	0	0	0	0	0	0	48.62
TRY_A	0	0	0	0	0	0	49.62	0	0	0	0	0	0	49.62
TRY_B	0	0	0	0	0	0	49.62	0	0	0	0	0	0	49.62

A.3 Optical power (in mW) on each sensor at each RF frequency (MHz)

	0.0	9.1	18.2	27.3	36.4	45.5	54.6	63.7	72.8	81.9	91.0
$REFL_A$	49.65	2.95	9.72	0	5.56	0.56	2.14	0	0.06	0	2.86
$REFL_B$	49.65	2.95	9.72	0	5.56	0.56	2.14	0	0.06	0	2.86
POP_A	49.73	0.08	0.21	0	0.99	0.06	0.35	0	0	0	0.15
POP_B	49.73	0.08	0.21	0	0.99	0.06	0.35	0	0	0	0.15
AS_A	2.44	0.06	0	0	0.13	2.28	0.05	0	0	0	1.20
AS_B	2.44	0.06	0	0	0.13	2.28	0.05	0	0	0	1.20
$OMCr_A$	48.36	0	0.05	0	2.21	0.07	1.83	0	0	0	7.98
$OMCr_B$	48.36	0	0.05	0	2.21	0.07	1.83	0	0	0	7.98
TRX_A	48.62	0	0	0	0	0	0	0	0	0	0
TRX_B	48.62	0	0	0	0	0	0	0	0	0	0
TRY_A	49.62	0	0	0	0	0	0	0	0	0	0
TRY_B	49.62	0	0	0	0	0	0	0	0	0	0

B Gouy phases relative to IFO mirrors

The Gouy phases reported in this document are relevant only in terms of their relative value. Their absolute value depends on the particular geometry of the readout telescope implemented in the model. In this appendix, the Gouy phases of the detectors placed at the output ports of the IFO are expressed with respect to the last IFO mirror.

B.1 aLIGO

REFL(from IN1, placed 2 meters from PRM) : $REFL_A = 88.9939$, $REFL_B = 1.09394$;

POP(from PR2) : $POP_A = 148.961$, $POP_B = 88.5613$;

AS(from SRM) : $AS_A = 173.142$, $AS_B = 91.6418$;

TRX(from EX) : $TRX_A = 14.0457$, $TRX_B = -75.9543$;

TRY(from EY) : $TRY_A = 14.0457$, $TRY_B = -75.9543$.

B.2 iLIGO-like

REFL(from IN1, placed 2 meters from PRM) : $REFL_A = 88.9939$, $REFL_B = 1.09394$;

POP(from PR2) : $POP_A = 148.961$, $POP_B = 88.5613$;

AS(from SRM) : $AS_A = 70.6418$, $AS_B = 91.6418$;

TRX(from EX) : $TRX_A = 14.0457$, $TRX_B = -75.9543$;

TRY(from EY) : $TRY_A = 14.0457$, $TRY_B = -75.9543$.

C Input Seismic Noise

C.1 Seismic Isolation

In aLIGO there will two different internal seismic isolation systems (ISI):

- the BSC ISI, for the BSC chambers (test masses and BS)
- the HAN ISI, for the HAM chambers (central cavity mirrors).

Both the BSC ISI and the HAM ISI have been commissioned in the last year. The BSC ISI has been built at the LASTI facility at MIT, and it is still under commissioning. The HAM ISI has been built and commissioned directly at the LIGO sites (OMC chamber HAM6), and it is currently operating in eLIGO. The performance of both the ISI systems expected for aLIGO has been based on the current measurements at LASTI and at LLO.

C.1.1 BSC ISI

The only complete BSC ISI system currently operating is at LASTI, MIT, in the center of Cambridge, MA. The current control strategy [5] is close to the one foreseen for aLIGO, even if further improvements are under study. The ground noise measured at LASTI is significantly higher than the ground motion measured at the LIGO sites, so that the predicted performance at the LIGO sites has been computed by considering the ratio between the two ground noises. The reference for the LIGO sites is the ground noise measured at LLO during S5 (90% contour, see [11]). Figure 44 shows the expected noise entering the suspension for the X degree of freedom (laser beam direction). Analogue estimates have been made for the other DOFs.

C.1.2 HAM ISI

The HAM ISI performance measured at LLO in each DOF is summarized in [6]. HEPI, another stage of attenuation of the ground noise, is planned to be installed in the HAM chambers. HEPI has been tested at LASTI, and the measured performance have been combined with the HAM ISI data in order to estimate the expected seismic noise entering the triple suspensions in aLIGO (figure 45). Since the effective motion at low frequency is over-estimated by the GS13, the low frequency signals (below 100 mHz) have been attenuated by a high pass filter.

C.2 Pitch input noise of the optics

The angular input noise motion used in the Optickle model has been computed by combining the seismic isolation performance with the transfer functions of the aLIGO suspensions:

- BSC ISI + Quadruple Pendulum(QUAD) : test masses (ETMX ETMY ITMX ITMY);
- HAM ISI + Triple Pendulum (TRIPLE): central cavity mirrors (PRM PR2 PR3 SRM SR2 SR3);
- BS ISI + BS Triple Pendulum (BS TRIPLE): beam-splitter (BS) .

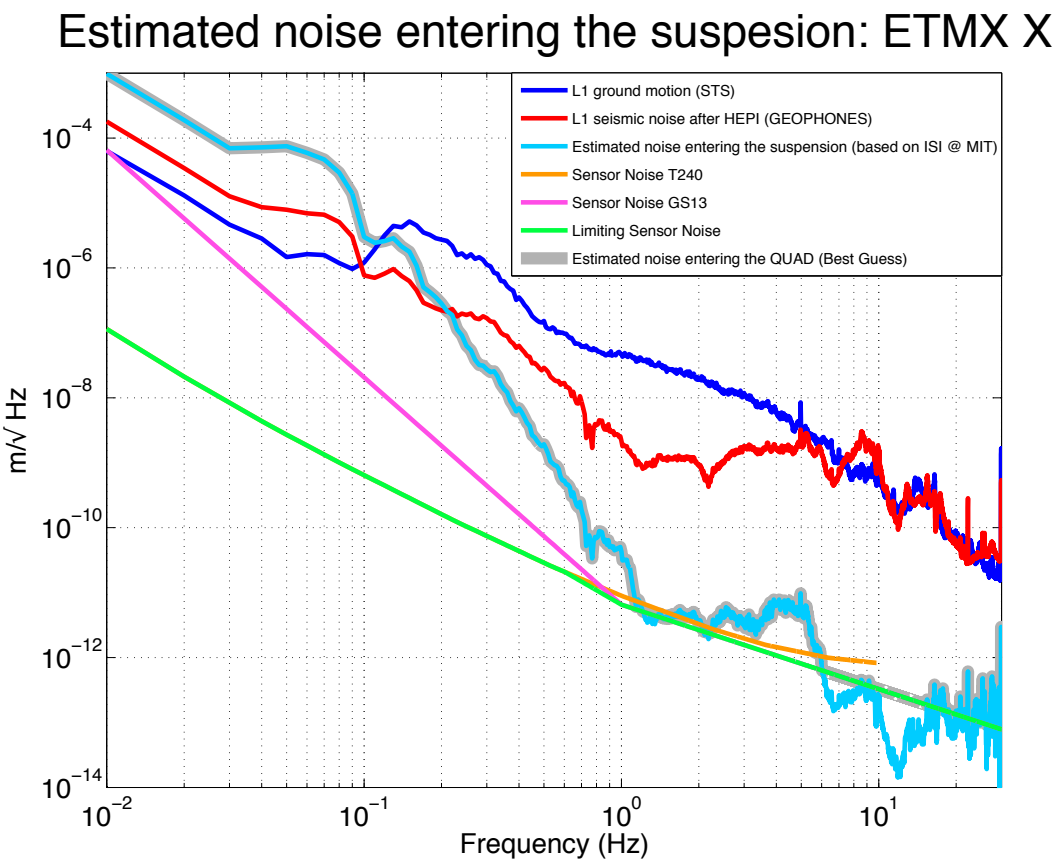

Figure 44: Best guess of the noise entering the BSC suspensions.

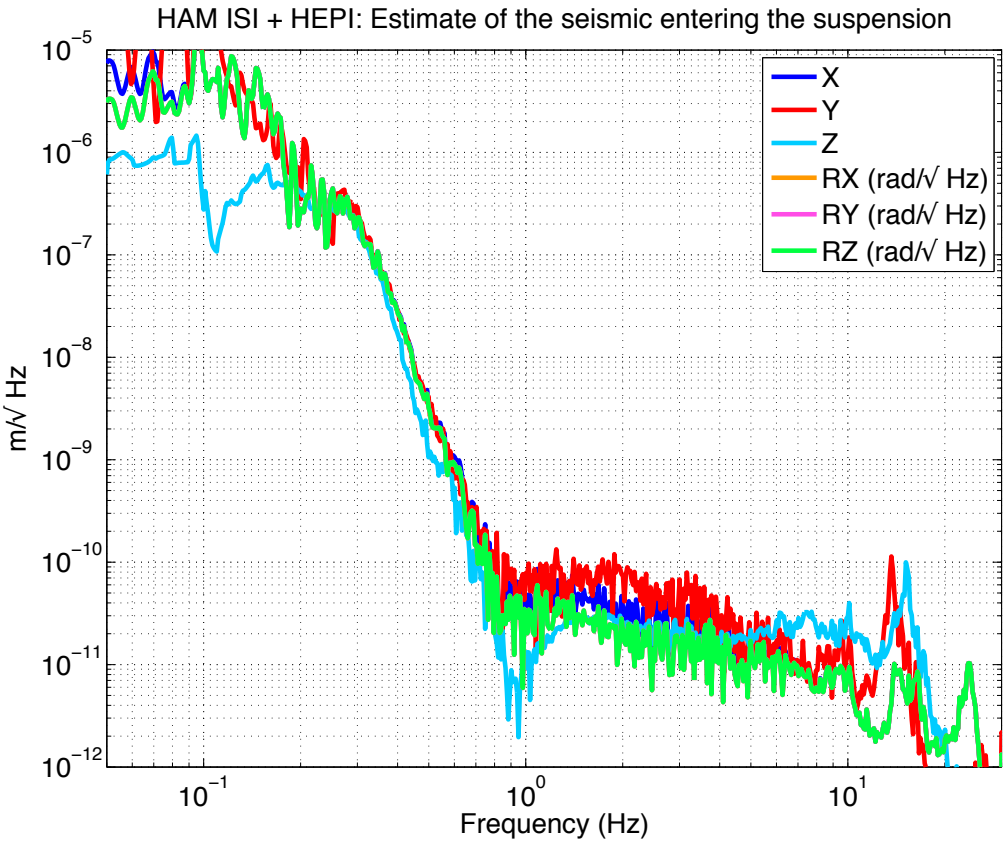

Figure 45: HAM ISI seismic noise in each DOF as measured at LLO (dotted lines), and the HAM ISI noise combined with the HEPI performance measured at LASTI (continuous line).

Local damping will be implemented in the suspensions, both the QUAD and the TRIPLE, in order to reduce the amplitude of the pendulum resonances. Moreover, locking forces will be applied at different stages of the suspensions in order to control the longitudinal degrees of freedom of the IFO. Very preliminary damping loops have been implemented in the model to reproduce the final configuration both on the TRIPLE and on the QUAD. However, a study of the propagation of the sensor noise and the effect of locking forces on the suspension transfer functions has been done only for the QUAD. For the TRIPLE, requirements have been set on the maximum sensor noise tolerable by the alignment scheme.

C.2.1 QUAD: Mirror pitch motion

In order to estimate the pitch motion of the aLIGO test masses, the seismic noise entering the suspension point of the quadruple pendulum has been filtered by the mechanical transfer functions from the suspension point to the pitch DOF of the test mass (TM). Simple longitudinal locking filters (TM to TM and penultimate mass, PM, to TM) have been added in the QUAD control matrix. The increase of the low frequency motion and the consequent increase in the RMS is the main difference observed between the two states (see figure 46).

The increase in the RMS is due to the X (longitudinal) to pitch coupling: when sending the locking force to the PM, the PM is also pitched, and this couples to pitch of the TM. Moreover, there is also the TM X to TM pitch coupling.

Through feed-forward cancelation this coupling can be, in principle, completely removed. Since the mechanical transfer functions of the system are well known, one can in fact exactly predict how much the length to pitch coupling will be, and subtract it. However, in order to do that, the mechanical transfer functions of the system need to be very precisely measured, which is not straightforward because of the many sharp peaks which characterize them. In this model we don't use the exact transfer functions, but we fit them with simple filters, to match the high and the low frequency part (see figure 47.

The length to pitch coupling is not perfectly compensated, but the RMS of the pitch motion is reduced by a factor 50.

Figure 49 shows the noise budget of the test mass pitch motion: seismic noise is dominating below 1 Hz, sensor noise above 1 Hz.

C.2.2 TRIPLE: Mirror pitch motion

Combining the HAM ISI performance with the TRIPLE transfer functions, the pitch motion of the optic results to be the one shown in figure 50. The performance of HEPI measured at LASTI has been included (green curve).

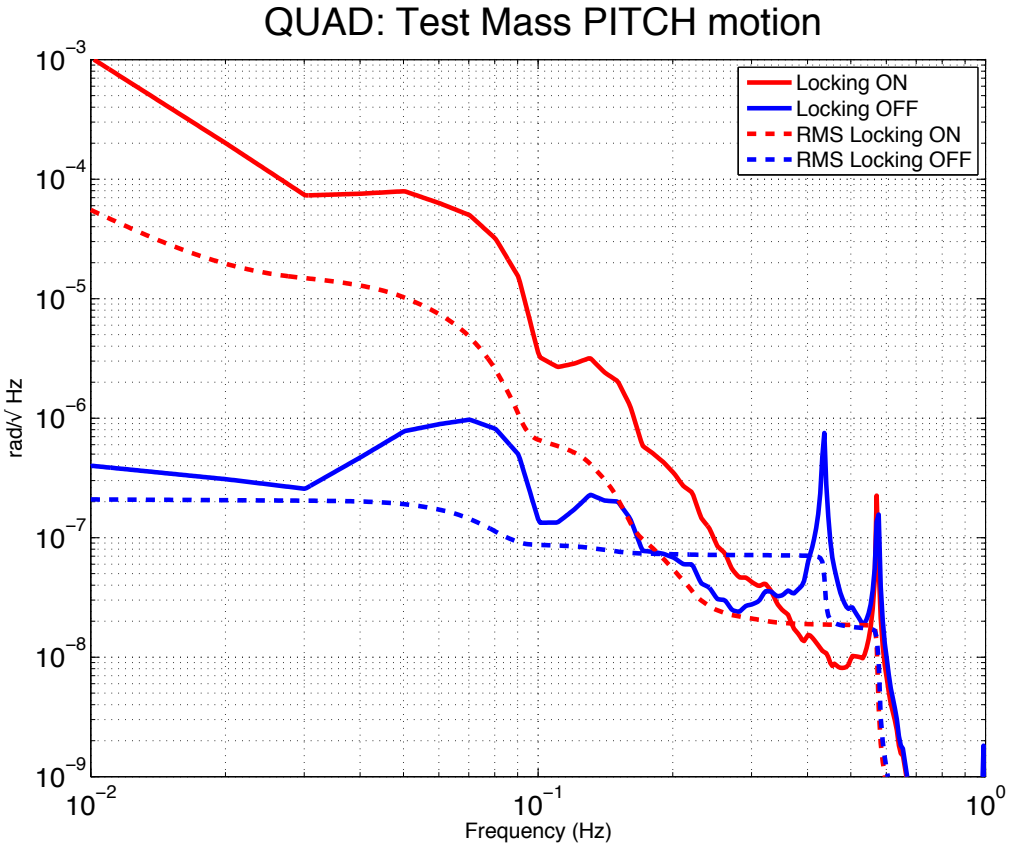

Figure 46: Pitch motion of the aLIGO test masses, hanged from the BSC ISI + Quadruple suspension, with and without locking forces on the PM and the TM. The impact of the locking forces is the increase of the low frequency motion. The RMS increases by more than two orders of magnitude, from 0.2 μrad to 50 μrad.

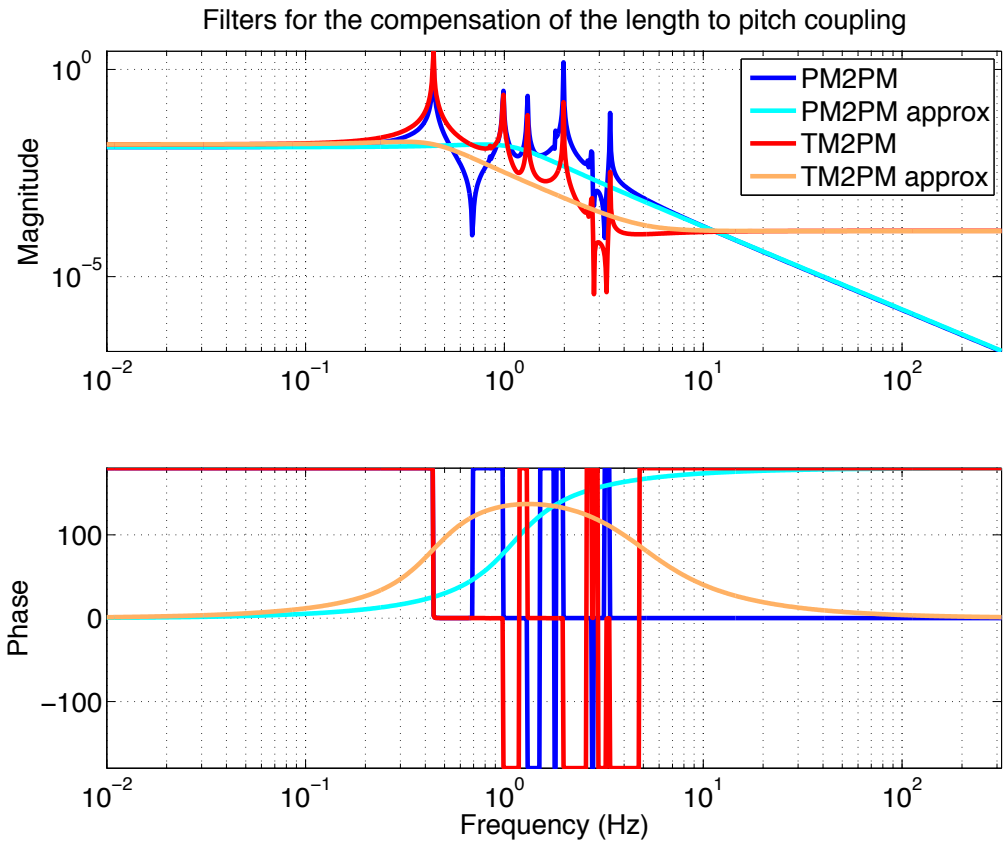

Figure 47: Approximation of the mechanical transfer functions of the system used for reducing the length to pitch coupling.

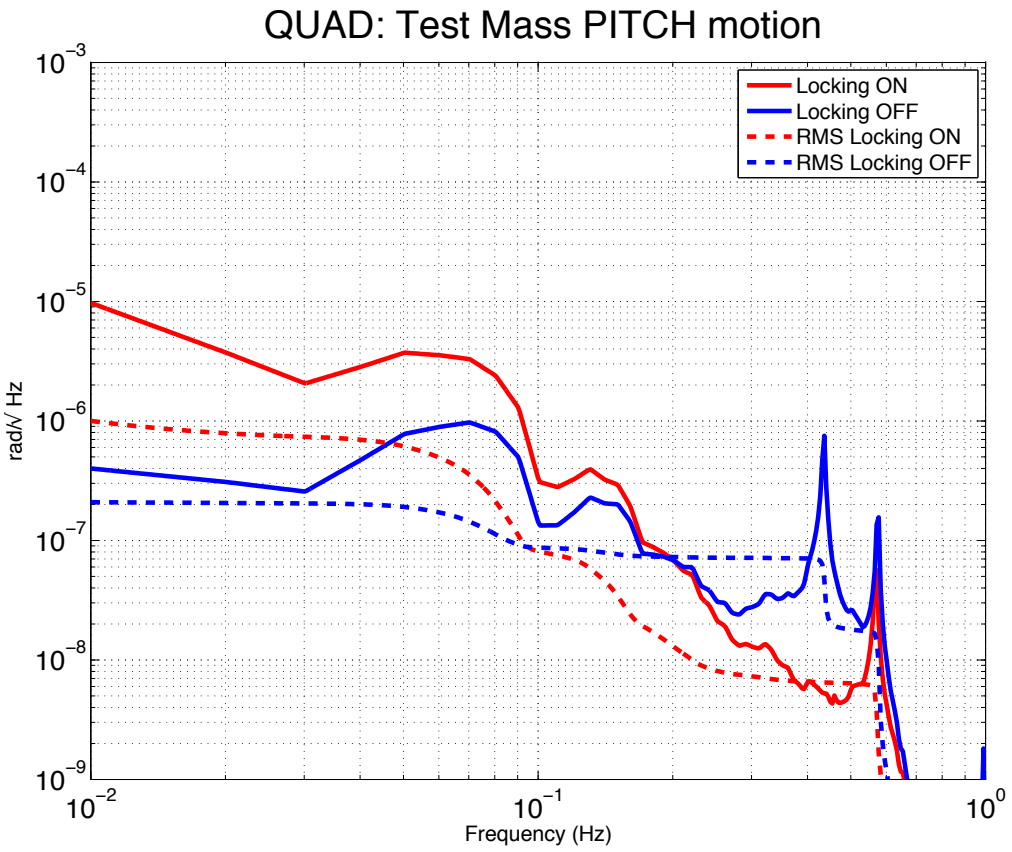

Figure 48: Test mass PITCH motion with the subtraction of the length to pitch coupling.

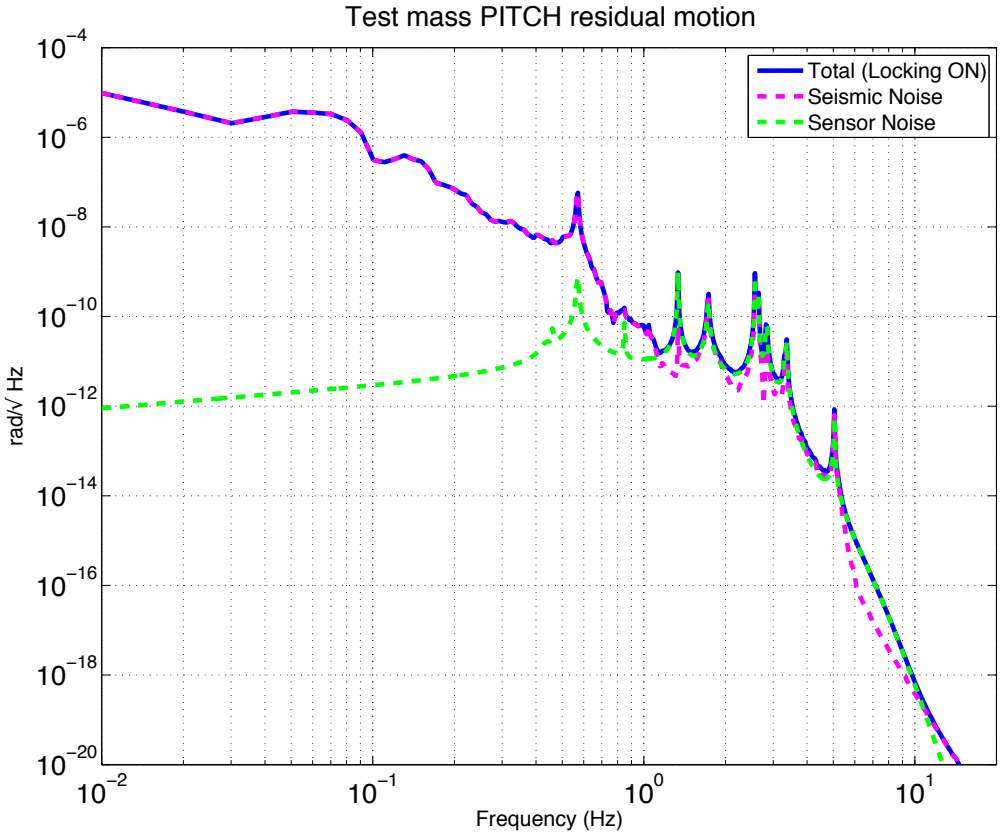

Figure 49: Noise budget of the pitch motion of the aLIGO test masses: below 1 Hz the motion is due to seismic noise, above 1 Hz by sensor noise.

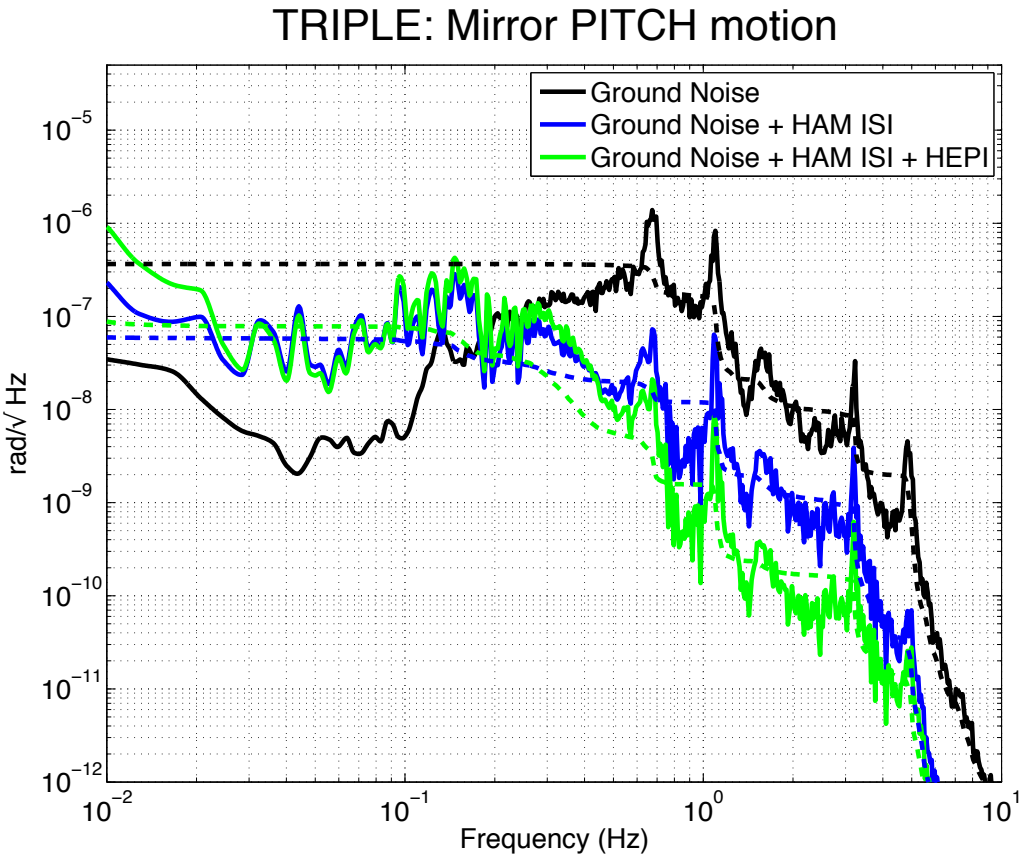

Figure 50: pitch motion of the mirror for the HAM ISI + HEPI + Triple (recycling cavity mirrors), compared with the pitch motion without HEPI (blue) and without any seismic isolation (direct coupling to GROUND noise, in black).

C.2.3 BS TRIPLE

The TRIPLE suspension of the BS differs from the one of the other recycling cavity optics. The difference in the transfer function from X at the suspension point to mirror pitch is shown in figure 51.

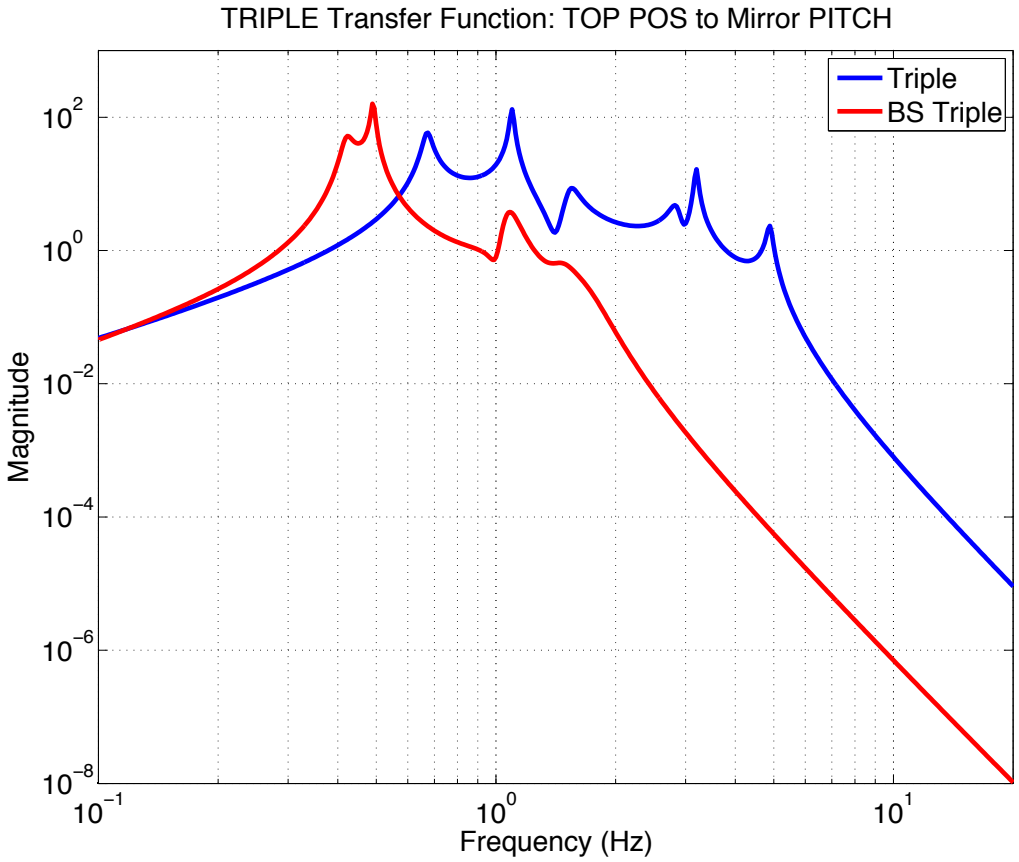

Figure 51: Comparison of the transfer function from X at the suspension point of the TRIPLE to Mirror pitch.)

D Amplitude modulation of the input beam

The input beam is steered into the IFO through 2 steering mirrors, IN1 and IN2 [7]. These mirrors are placed in the HAM2 chamber in aLIGO, and are suspended by simple pendulum suspensions. An estimate of the PITCH motion of these mirrors is given in figure 52.

The RIN of the amplitude modulation of the input beam produced by these mirrors can be computed by adopting the formalisms shown in section 5.4:

[7] The actual names of these two mirrors in the final aLIGO layout are actually SM1 and SM2.

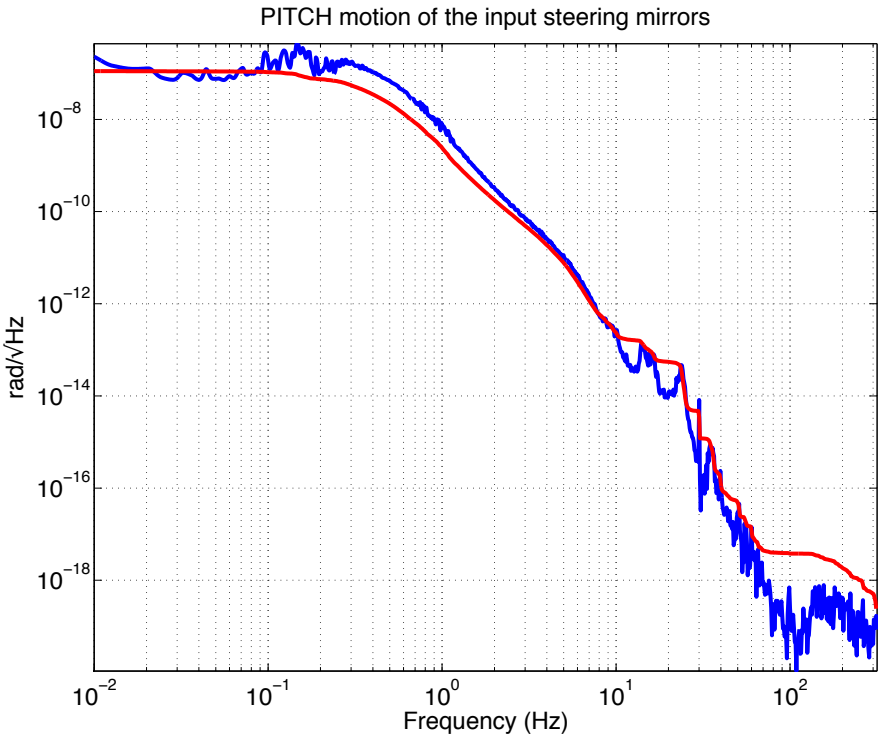

Figure 52: PITCH motion of the input steering mirrors.

$$RIN = \frac{\Delta A_{00}}{A_{00}} \sim 4\alpha^2 \frac{\hat{\Theta}_{mirr} * \hat{\Theta}_{beam}}{\Theta_0^2}$$

where $\hat{\Theta}_{mirr}$ is the motion of the input mirrors and $\hat{\Theta}_{beam}$ is the beam angular motion.

Typically, we want a RIN lower than 10^{-9} above 10 Hz. Figure 53 shows that the RIN is well below that threshold.

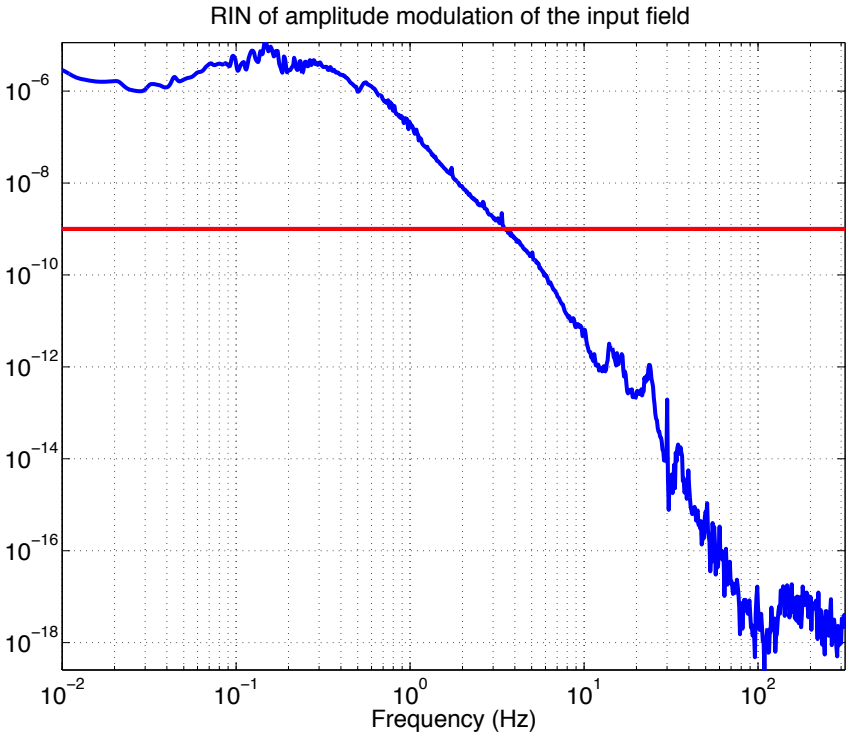

Figure 53: RIN of the amplitude modulation of the input beam produced by the steering mirrors.

E Shift and Tilt

The representation of stable and unstable modes of a cavity can be usefully thought also in terms of shift and tilt of the cavity axis. Naively, one would say that a stable mode is mainly a tilt of the cavity axis, while an unstable mode is mainly a shift of the cavity axis. However, we have a pure shift or tilt only in case of a symmetric cavity. When the cavity is not symmetric, it can be useful to know how big are the off-diagonal terms of the matrix which translates the soft and hard modes in shift and tilt of the cavity axis at the cavity waist.

Let's consider a reference frame in which the X axis is defined by the cavity axis, with the 0 located at the intersection between the cavity axis with the HR surface of the input mirror (ITM), the HR surface of the end mirror (ETM) located at the position +L, where L is the length of the cavity. The reference frame is shown in figure 54, which shows a positive tilt of the two mirrors (the angles are expresses as usual in radians, the lengths in meters).

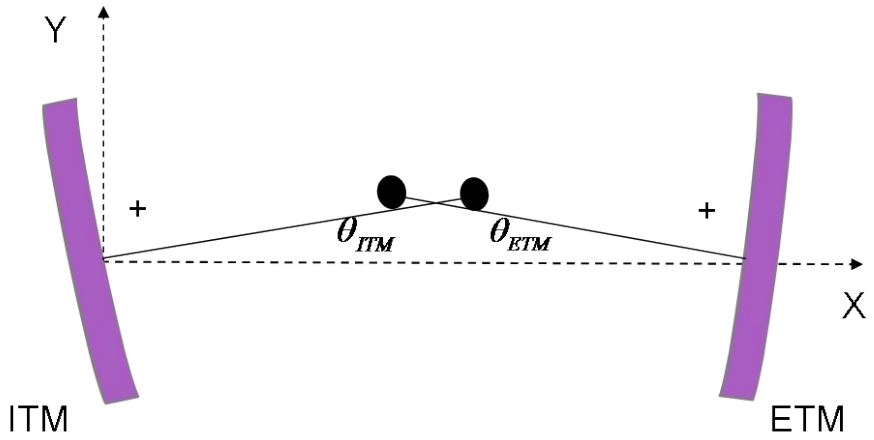

Figure 54: Reference frame of a single cavity.

In this reference frame, the matrix which couples the tilts of the two mirrors into the shift Y and the tilt θ_{tilt} at the cavity waist is:

$$\begin{pmatrix} Y_{Shift} \\ \theta_{Tilt} \end{pmatrix}_{waist} = \begin{pmatrix} R_1(R_2 - X_w) & R2(X_w + R_1 - L) \\ -R_1 & R2 \end{pmatrix} \begin{pmatrix} \theta_{ETM} \\ \theta_{ITM} \end{pmatrix}$$

Where R_1 is the ETM ROC, R_2 is the ITM ROC, and X_w is the position of the waist:

$$X_w = \frac{L(R_1 - L)}{(R_1 + R_2 - 2L)}$$

The matrix which couples the tilt of the mirrors in terms of soft and hard dofs has been described in section 3.2:

$$\begin{pmatrix} \theta_{ETM} \\ \theta_{ITM} \end{pmatrix}_{waist} = \begin{pmatrix} 1 & r \\ r & -1 \end{pmatrix} \begin{pmatrix} \theta_{Soft} \\ \theta_{Hard} \end{pmatrix}$$

The product of these two matrix gives us the matrix which express the shift and the tilt of the cavity axis at the waist in terms of the soft and hard modes:

$$\begin{pmatrix} Y_{Shift} \\ \theta_{Tilt} \end{pmatrix}_{waist} = \begin{pmatrix} R_1(R_2 - X_w) & R2(X_w + R_1 - L) \\ -R_1 & R2 \end{pmatrix} \begin{pmatrix} 1 & r \\ r & -1 \end{pmatrix} \begin{pmatrix} \theta_{Soft} \\ \theta_{Hard} \end{pmatrix}$$

With the aLIGO numbers listed in table 2, we get:

$$\begin{pmatrix} Y_{Shift} \\ \theta_{Tilt} \end{pmatrix}_{waist} = \begin{pmatrix} 2238.3 & 512.19 \\ -0.078687 & -24.516 \end{pmatrix} \begin{pmatrix} \theta_{Soft} \\ \theta_{Hard} \end{pmatrix}$$

References

[1] Optickle is available in the MIT CVS repository at emvogil-3.mit.edu:/export/cvs/iscmodeling. The configuration file with the eLIGO parameters and the Optickle model used in this note can be found in the same place under the name "pickle".

[2] L. Barsotti, M. Evans *Modeling of Alignment Sensing and Control for Enhanced LIGO* LIGO-T080186.

[3] Sidles, Sigg *Optical torques in suspended Fabry-Perot interferometers*, Physics Letters A **354** (2006) 167-172.

[4] Ballmer et al., AdvLIGO Interferometer Sensing and Control Conceptual Design Document LIGO-T070247 (2007)

[5] The measurements at LASTI have been carried out by Fabrice Matichard, and they can be found in the BSC ISI report document.

[6] Kissel et al, L1 HAM6 ISI eLIGO Final Performance Measurements, LIGO internal document T0900285-v1.

[7] Model tuend by Brett Shapiro.

[8] S, Waldman *Transmon sensitivity calculations*, LIGO internal document G0900293-v3.

[9] Measurements taken by Richard Mittelman, cfr SEI logbook.

[10] P. Fritschel et al. *Alignment of an interferometric gravitational wave detector*, Applied Optics, **37**, 28 (1998)

[11] P. Fritschel, S. Waldman *Reference Seismic Data for LLO* LIGO-T0900312-v1

[12] M. Arain and G. Mueller *Optical Layout and Parameters for the Advanced LIGO Cavities*, LIGO internal note, LIGO-T0900043-08 (2009)